Rydberg Molecules and Excitation of Lattice-Mixed Rydberg States in a Deep Ponderomotive Optical Lattice

by

Jamie L. MacLennan

A dissertation submitted in partial fulfillment
of the requirements for the degree of
Doctor of Philosophy
(Applied Physics)
in The University of Michigan
2021

Doctoral Committee:

Professor Georg Raithel, Chair
Professor Steven Cundiff
Professor Cagliyan Kurdak
Professor Vanessa Sih
Professor Duncan Steel

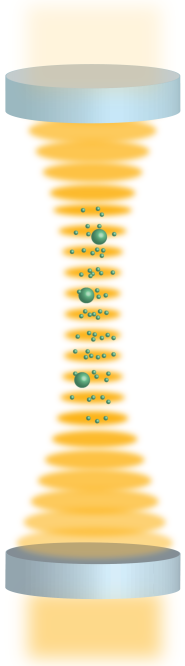

Illustration of Rydberg atoms in
a cavity-generated optical lattice

Jamie L. MacLennan

jmaclenn@umich.edu

ORCID iD: 0000-0002-0511-7203

To my wonderful parents

ACKNOWLEDGEMENTS

I am thankful to all of the people who inspired, guided and supported me through this journey.

Georg, I'm so glad to have had you as my advisor. I am always impressed by the how much you know about all sorts of different things, spanning theoretical to practical, and extending far beyond your own area of research. Your enjoyment of physics for its own sake is inspiring, and I have appreciated your supportiveness of your students, including how you always make time to help, whether explaining concepts, editing writing, or troubleshooting mysterious issues in the lab. Your good-naturedness and curiosity have shaped the lab to be an enjoyable and rewarding environment.

Thank you to the other members of the Raithel lab: David Anderson, Stephanie Miller, Kaitlin Moore, Yun-Jhih Chen, Luis Felipe Goncalves, Nithiwadee "Pound" Thaicharoen, Andira Ramos, Ryan Cardman, Michael Viray, Lu Ma, Xiaoxuan Han, and Alisher Duspayev. Dave, Stephanie, and Kaitlin, thank you for providing me with invaluable guidance as I became first acquainted with the lab and Rydberg-atom research. Thanks, Yun-Jhih, for dedicating many weeks to teaching me the nuances of her well-constructed experimental setup, which you passed on to me in fully working condition. Though words will never do it justice, thank you, Andira, for your never-ending support, in and out of the lab, and being the most faithful of a friend. Thanks also for the music, cookies, encouragement, and perspectives you've provided. Ryan, I've amazed at how quickly you were able to provide significant practical contributions

when you began working in our lab—including, but not limited to, projects with me. It's been a huge help and pleasure working with you. I know that you will go far in physics (if you want to). Between you and Alisher, I'm confident that the experiments that we began are in good hands. Thanks, Xiaoxuan, for support on the research projects, including taking care of the experimental setup while I was in India, collecting initial data and making other significant experimental progress. Thanks to those who provided edits and helpful suggestions for this dissertation: Georg, Andira, Ryan, Alisher, Mike, Jay, and Rob.

I would like to thank my Applied Physics class—Danielle Sofferman, Libby Maret, Brad Smith, Luis Sagastume, Mallory Fuhst, Roy Llewellyn, Xi Chen, Xinlin Song, Brian Worthmann, and Ben Isaacoff—whose camaraderie and collective intellect and teaching abilities were indispensable in helping me making it through the first two years of graduate school. Thanks to Cyndi McNabb, Prof. Çagliyan Kurdak, Prof. Duncan Steel for providing advice and support throughout grad school. Thanks to Prof. Umakant Rapol and the members and other participants in his research group at IISER Pune—Chetan Vishwakarma, Jay Mangaonkar, Pranab Dutta, Korak Biswas, Kushal Patel, Shiv Sagar Maurya, Harinee Natarajan, and Pragya Kushwaha. Thank you for providing me the opportunity to learn about new physics experiments and for welcoming me so warmly to your group during my temporary stay at IISER. Thanks to Prof. Paul Berman, who taught my graduate quantum optics course, for making the course less daunting by injecting humorous perspectives about the lives of atoms, and for permission to quote you throughout this dissertation. Thank you to Dr. Guang-Chong Zhu, Dr. Changgong Zhou, and Dr. Scott Schneider for your encouragement and support in my academic journey and decision to apply to graduate school. Thank you to others in my life who supported me through everything- Dayani Waas, Katie Trapp, Katie Joh, Rachel Martindale, HyeJin Hwang, Gina Lipor, Amy Gray, JT and Chithra Townsend, and other Mosaic friends; my roommate, Susannah

Engdahl; my siblings Kelsey, Daniel, and Brandon; my dad, Scott; and my high-school physics teacher, Wendy, who is also my mom.

Thank you, God, for everything. You're the author of knowledge and wisdom, and the giver as well. You inspire awe and wonder, and I love seeking to peer into the glories reflected into your physical creation. You made the universe with infinite wonderful avenues to explore, and it has delighted me to see how even a single atom has a whole inner world. I marvel that you *spoke*, and it came to be. I also thank you for the gifts and lessons you've provided me through grad school that were sometimes very hard, including for humbling me—deepening my awareness of how much I don't know, and teaching me how to ask for help. Thank you, especially, for your presence.

I would like to acknowledge support from the National Science Foundation (NSF) Graduate Research Fellowship Program (GRFP) under Grant No. DGE 1256260 and the Applied Physics program at the University of Michigan. I would also like to acknowledge the NSF Graduate Research Opportunity Worldwide (GROW) program, the Indo-U.S. Science and Technology Forum (IUSSTF), and the University of Michigan's International Institute (II) and Applied Physics program, for granting me the funds to collaborate with the group of Prof. Umakant Rapol at the Indian Institute of Science Education and Research Pune (IISER Pune), to learn about and support experiments that complemented my work on Rydberg atom spectroscopy and widened my exposure to more topics and techniques within experimental atomic physics.

Lastly, I want to thank Steven Cundiff, Çagliyan Kurdak, Vanessa Sih, and Duncan Steel, for serving on my dissertation committee and providing helpful feedback for improving this document.

TABLE OF CONTENTS

LIST OF FIGURES

Figure

LIST OF TABLES

Table

LIST OF APPENDICES

Appendix

LIST OF ABBREVIATIONS

AOM acousto-optic modulator

APD avalanche photodiode

BEC Bose-Einstein Condensate

DBR distributed Bragg reflector

ECDL external cavity diode laser

EIT electromagnetically induced transparency

EOM electro-optic modulator

FPI Fabry-Pérot interferometer

FSR free spectral range

FWHM full-width half-maximum

HG Hermite-Gaussian

MCP microchannel plate

MOT magneto-optical trap

OPLS offset phase lock servo

PA photoassociation

PD photodiode

PEC potential energy curve

PI photoionization

PLL phase-locked loop

POL ponderomotive optical lattice

RF radio frequency

SHG second-harmonic-generation

TA tapered amplifier

ULE ultralow-expansion

ABSTRACT

In this dissertation, I explore several aspects of Rydberg physics with laser spectroscopy. The experiments center around the use of a very deep, cavity-generated, one-dimensional optical lattice in a cold atom sample. The optical lattice produces elongated clouds of dense, cold atoms via dipole trapping and is able to generate extreme light shifts in the atoms due to its high intensity. I describe experiments which may be divided into two main classes. In the first, I use the dipole trap to prepare a dense sample of atoms for photoassociation of Rb atom pairs into diatomic Rydberg molecules. The Rydberg molecules are formed by low-energy scattering of the Rydberg electron of one atom from the other atom, which is a ground-state atom. This novel binding mechanism also has relevance for chemical physics. I present binding energy measurements for eight different cases of Rydberg molecules. The binding energies reveal information about electron-atom collisions, such as their scattering lengths, and about the spin couplings present within the molecular system. In the second class of experiments, I introduce two proposed measurements in which the optical lattice is ramped to very high intensity during the laser excitation, creating AC Stark shifts in the transition frequencies. In one measurement, low-lying atomic states are probed. Measurements of the light shifts are expected to yield data on the dynamic polarizability and the photoionization cross section of the $5D_{3/2}$-state in rubidium in a 1064-nm light field. I show corresponding preliminary experimental data. The polarizability and photo-ionization cross-section measurements will provide tests of atomic structure theory, which is important both at a fundamental level and for applications such as atomic clocks. In another proposed measurement,

Rydberg atoms in the lattice experience ponderomotive shifts and strong mixing of their angular-momentum states, allowing direct optical excitation of the lattice-mixed high-angular-momentum states. I describe the theoretical basis and experimental preparation for spectroscopically characterizing the lattice-mixed states. The ability to optically excite selected high-angular-momentum states without the use of static or RF fields may be useful for quantum information processing and simulation.

CHAPTER I

Introduction

"If you're an atom, moving along, singing your song..."

– Paul Berman

1.1 A model atom

The work in this thesis is centered on Rydberg atoms. Rydberg atoms are highly-excited atoms, in which one of the electrons occupies a state with a very high principal quantum number. Although Rydberg atoms have likely existed since not long after the universe began [1], they were not discovered until the late 19th century. They were predicted through the work of Johann Balmer and subsequently Johannes Rydberg to explain absorption spectra [2, 3], building on the concepts introduced by Bohr's model of hydrogen.

Rydberg atoms are giant in size; they can be hundreds or thousands of times larger than atoms in non-excited (i.e. ground) states, with observed sizes as large as bacteria. They have many other unusual properties [4] including long decay times and extreme sensitivity to electric fields [5] (and also to magnetic fields, for certain Rydberg states [6]). Because the Rydberg electron is shielded from the nucleus by the core electrons, Rydberg states closely resemble those of hydrogen regardless of the atomic species. Their resemblance to hydrogen, which is the element with the closest

to a fully analytical solution to its quantum mechanical description, makes them far simpler to model and analyze. The long lifetimes of Rydberg atoms allow them to be considered metastable states in many contexts. The simple atomic structure, long lifetime, and exaggerated sensitivities of a Rydberg atom make it a model atom for a wide variety of experiments.

The ultra-high sensitivities of Rydberg atoms to their environment opens up numerous possibilities for technological applications as well as for their utilization as sensitive probes of experimental physics. I elaborate on the former category in the beginning of Chapter III; applications include atomic clocks, quantum sensing and communications, and quantum information processing. The research here relates to the latter category; it includes the examination of two situations in which the loosely-bound Rydberg electron acts as a probe of some underlying physics. In the Rydberg molecule experiment, a Rydberg electron probes a second atom that is in its ground-state by scattering from it. The energies of the bound molecular states contain information about the properties of electron-atom collisions. In the experiment involving Rydberg atoms in an optical lattice, the Rydberg electron probes light intensities that are spatially and periodically modulated over the same scale as the size of the electron orbital.

1.2 Thesis framework

In this dissertation, I present three primary experiments. While the physics probed by each of experiments is somewhat different, their experimental and theoretical "building blocks" overlap significantly; they all involve the study of Rydberg states and/or light shifts, the preparation of cold atom samples, and the measuring of ion counts as one of the excitation lasers is scanned over $\sim$0.5 GHz or more. I begin in Chapter II by briefly describing some of the physics governing the methods I use to optically cool and trap atoms in their ground-state. In Chapter III, I introduce

Rydberg atoms and Rydberg molecules, noting some of their unusual properties and abilities. I describe the central features of the experimental setup in Chapter IV, including a near-concentric cavity generating an optical lattice dipole trap, a variety of laser systems, methods employed for atom detection, and optical phase-locked loop (PLL) setups that are used for highly precise frequency control for two of the excitation lasers.

The subsequent three chapters (V, VI, and VII) correspond to the three primary experiments. The introductory information and motivations that are specific to each experiment are discussed in the beginning of each chapter, such that these chapters are largely self-contained. In Chapter V, I investigate rubidium (Rb) ($24D_J$+$5S_{1/2}$) Rydberg molecules bound by scattering of Rydberg electron and a neutral ground-state atom. I measure and compare binding energies for eight combinations of spins that are coupled within the molecular system, and discuss how the spin couplings affect the binding energies. I explain an adapted theoretical model and use it with the binding energy data to extract the four electron-atom scattering lengths describing the scattering interactions. In Chapter VI, I discuss a measurement of the dynamic polarizability and photoionization cross section of the Rb $5D_{3/2}$ state. Measuring two atomic transitions that are light-shifted by a high-intensity 1064-nm dipole trap reveals a relation of the polarizabilities of the three states involved; when two polarizabilities are known, the third may be solved for without having precise knowledge of the 1064-nm intensity. The spectra linewidths will also allow a photoionization cross-section measurement to be extracted. The experiment in Chapter VII builds upon the polarizability experiment by extending the excitation scheme with a third step, this time reaching Rydberg states. For Rydberg states, the shifts from optical lattices are caused by the ponderomotive energies of the Rydberg electron instead of the electric dipole interaction with the atom. I explain how the ponderomotive interaction in an optical lattice causes mixing of the angular-momentum states at high

optical intensities. The goal of the proposed experiment is to observe the lattice-mixed state. To guide the design of the experiment, I consider calculated results of adiabatic potential energy curves across one lattice period, as well as of line strengths, photoionization rates and corresponding spectra, for a variety of possible excitation schemes and principal quantum numbers. Finally, in Chapter VIII, I summarize the main findings of the presented work and outline future directions.

CHAPTER II

Manipulating Atoms with Light

"You should have learned this in kindergarten."

– Paul Berman, on various parts of atomic physics theory

Laser light offers the most precise tools to excite and control matter at the level of isolated atoms and molecules. In this chapter I provide brief, basic descriptions of several light-matter interactions that are commonly used in atomic physics experiments, including those presented in this thesis. I focus on the applications to rubidium (Rb) because it is the primary element studied in this work. For comparison to an alternate element, I also reference strontium (Sr).

2.1 Electronic structure

Each atomic species has its own signature structure of excited electronic states due to its unique nuclear core and number of electrons. The differences in electronic structure among atomic species are the most dramatic in their low-energy states, where the outermost electron(s) have significant spatial overlap with the regions of the nucleus and lower-lying electrons. Highly-excited states (discussed in the next chapter), on the other hand, tend to have more similarities than differences—especially for alkali atoms—because the outermost electron shell largely occupies free space.

2.1.1 Rb and Sr

Rubidium is an alkali metal, which means it has a single valence electron, and has many similarities to hydrogen. In contrast, strontium is an alkaline-earth metal, with two valence electrons and a level structure that is akin to helium. The two valence electrons may be in either antiparallel or parallel alignment, which give singlet $S = 0$ or triplet $S = 1$ states.

Of the 32 Rb isotopes that can exist, only 2 are naturally occurring and relatively stable. The composition of naturally occurring Rb is about three-quarters ^{85}Rb and one-quarter ^{87}Rb, with respective nuclear spins of $I = 5/2$ and $I = 3/2$. While ^{85}Rb is inherently stable, ^{87}Rb is very slightly radioactive, decaying into ^{87}Sr with a half-life of about 50 billion years. Strontium has four stable, naturally occurring isotopes. Three (^{84}Sr, ^{86}Sr, ^{88}Sr) are bosonic, which together with their having two valence electrons, implies that their nuclear spins are zero. The fermionic isotope, ^{87}Sr, has a nuclear spin of $I = 9/2$. A summary of the isotopes of Rb and Sr is shown in Table 2.1.

Isotope	Natural abundance	Fermionic/Bosonic	Nuclear spin
^{85}Rb	72.2%	bosonic	5/2
^{87}Rb	27.8%	bosonic	3/2
^{84}Sr	0.56%	bosonic	0
^{86}Sr	9.86%	bosonic	0
^{87}Sr	7.00%	fermionic	9/2
^{88}Sr	82.58%	bosonic	0

Table 2.1: Isotopes of Rb and Sr.

2.2 Atoms in static or oscillating electric fields

This section draws equations and insights from Refs. [7–11], and I recommend them for more in-depth analyses of the topics presented here.

"You can all do this in your head... or your neighbor's head."

– Paul Berman

2.2.1 Static electric field

An external electric field interacts with and shifts atomic energy levels, a phenomenon called the Stark effect. We first consider an atom in initial state i in a weak static electric field $\vec{\mathcal{E}}$ (i.e. the field is weak enough such that the energy shift caused by the field is small relative to the level spacing of the atom). Non-degenerate perturbation theory gives a first order correction to the energy of:

$$\Delta E_i^{(1)} = \left\langle \psi_i \left| \vec{d} \cdot \vec{\mathcal{E}} \right| \psi_i \right\rangle$$

where $\vec{d} = e\vec{r}$ is the electric dipole moment of the atom. Because only $\Delta l = \pm 1$ transitions are allowed, this term is zero for low-l, non-hydrogenic states because these do not have degenerate states with different parities. Thus, for these states the lowest-order nonvanishing energy correction is the second order term, known as the quadratic Stark effect:

$$\Delta E_i^{(2)} = \sum_{f \neq i} \frac{\left| \left\langle \psi_f \left| e\vec{r} \cdot \vec{\mathcal{E}} \right| \psi_i \right\rangle \right|^2}{E_i^{(0)} - E_f^{(0)}} = -\frac{1}{2}\alpha_0 \mathcal{E}^2 \tag{2.1}$$

where α_0 is the static polarizability of the atomic state i ($\alpha \coloneqq d_z/\mathcal{E}_z$), and the subscript f refers to the identity of a perturbing atomic state.

2.2.2 Oscillating electric field

In an oscillating electric field $\vec{\mathcal{E}}(t) = \vec{\mathcal{E}}_0 \cos(\omega t)$, an atomic state experiences a second-order energy shift when the field frequency is far from resonance with every other atomic state f, i.e. when $|\delta_f| \gg \Omega_R$ for all f states, where the Rabi frequency

is $\Omega_R = \langle\psi_f|e\vec{r}\cdot\vec{\mathcal{E}}_0|\psi_i\rangle/\hbar$, the detuning is $\delta_f = \omega - \omega_f$, and the resonance frequency is $\omega_{fi} = (E_f - E_i)/\hbar$.

In the dressed-atom picture, the unperturbed eigenstates are

$$\phi_{n,k} = \psi_n e^{-ik\omega t}, \tag{2.2}$$

where k is the number of photons exchanged between the atom and the field.

The energy shift is similar to equation (2.1), except the matrix element now contains a time-dependent field. A time-average over one oscillation period selects only transitions where $k = \pm 1$ and yields a factor of 1/2 compared to a static field, that is,

$$\langle\langle\phi_{f,k}|\phi_{i,0}\rangle\rangle = \frac{\omega}{2\pi}\int_0^{2\pi/\omega}\left\langle\psi_f\left|e\vec{r}\cdot\vec{\mathcal{E}}_0\cos(\omega t)\right|\psi_i e^{ik\omega t}\right\rangle dt \tag{2.3}$$

$$= \begin{cases}\frac{1}{2}\left\langle\psi_f\left|e\vec{r}\cdot\vec{\mathcal{E}}_0\right|\psi_i\right\rangle, & \text{if } k=\pm1\\ 0, & \text{otherwise.}\end{cases} \tag{2.4}$$

Now the energy shift is

$$\begin{aligned}\Delta E_i^{(2)} &= \sum_{f\neq i}\frac{\frac{1}{4}\left|\left\langle\psi_f\left|e\vec{r}\cdot\vec{\mathcal{E}}\right|\psi_i\right\rangle\right|^2}{E_i^{(0)}-E_f^{(0)}-\hbar\omega} + \frac{\frac{1}{4}\left|\left\langle\psi_f\left|e\vec{r}\cdot\vec{\mathcal{E}}\right|\psi_i\right\rangle\right|^2}{E_i^{(0)}-E_f^{(0)}+\hbar\omega}\\ &= \sum_{f\neq i}\frac{\hbar|\Omega_R|^2}{4}\left(\frac{1}{\omega_{fi}-\omega}+\frac{1}{\omega_{fi}+\omega}\right)\\ &= \sum_{f\neq i}\frac{\hbar|\Omega_R|^2}{4}\left(\frac{2\omega_{fi}}{\omega_{fi}^2-\omega^2}\right).\end{aligned} \tag{2.5}$$

When the laser is much closer to one resonance than any others, the atom may be approximated as a two-level system (with state i and a single state f). The detuning, i.e. the driving field angular frequency relative to the transition angular frequency, is now defined as simply δ. Note that the assumption $|\delta| \gg \Omega_R$ has already been

made previously. If the detuning is small compared to the transition frequency (i.e. $|\omega - \omega_{fi}| \ll \omega + \omega_{fi}$), the rotating-wave approximation may be made, and Eq. 2.5 becomes [7, 9]

$$\Delta E \approx \pm \frac{\hbar \left|\Omega_R\right|^2}{4\delta} = \pm \frac{\hbar \Gamma^2}{8\delta} \frac{I}{I_{sat}}, \tag{2.6}$$

where the upper sign (+) is for the ground state (i) and the lower sign (-) is for the excited state (f), and I and I_{sat} are the actual intensity and saturation intensity, respectively. The saturation intensity of an atomic transition is a useful intensity scale; when the laser intensity is equal to it and the system is in steady state, the excited population is 1/4 and an atom has an equal chance of decay by stimulated emission as by spontaneous emission. The saturation intensity depends on the atomic transition properties; for circularly-polarized light, $I_{sat} = 2\pi^2 \hbar c \Gamma / (3\lambda^3)$.

2.2.3 Dynamic polarizability

The polarizability due to an oscillating electric field is known as the dynamic polarizability (sometimes also referred to as AC polarizability). Eq. 2.5 may be written alternatively in terms of dynamic polarizability as

$$\Delta E_i^{(2)} = -\frac{1}{4} \alpha(\omega) \mathcal{E}_0^2, \tag{2.7}$$

where

$$\alpha(\omega) = -\sum_{f \neq i} \left| \left\langle \psi_f \left| \vec{d} \right| \psi_i \right\rangle \right|^2 \left(\frac{1}{E_i^{(0)} - E_f^{(0)} - \hbar\omega} + \frac{1}{E_i^{(0)} - E_f^{(0)} + \hbar\omega} \right). \tag{2.8}$$

The polarizability $\alpha(\omega)$ depends on the m quantum numbers of the i and f states. It is convenient to find an isotropic (rotationally invariant) polarizability, which is [8,

11]

$$\alpha_I(\omega) = \frac{2}{3\hbar} \sum_{f \neq i} \frac{|\langle f||e\vec{r}||i\rangle|^2 \omega_{fi}}{\omega_{if}^2 - \omega^2}, \tag{2.9}$$

where $|\langle f||e\vec{r}||i\rangle|$ is the reduced matrix element.

For resonances to higher energy states, the sign of the polarizability is positive for red-detuned frequencies (i.e. $\omega < \omega_{fi}$ for all f) and negative for blue-detuned frequencies. For states with multiple transitions, the sign depends on the total contributions from all of them. For positive polarizabilities, the AC Stark effect allows one to optically trap atoms with a simple Gaussian beam, as discussed in the following section.

2.3 Cooling and trapping

Because the main trapping tools in this work are an optical dipole trap and a magneto-optical trap (MOT), I briefly summarize their underlying physics here.

2.3.1 Far-off resonance optical dipole trap (FORT)

The energy shift due to the AC Stark effect is the basis of the trapping forces in an optical dipole trap. In a two-level system and in the limit of large detuning, the energy potential for the initial state is, from Eq. 2.6,

$$U \approx \frac{\hbar\Gamma^2}{8\delta} \frac{I}{I_{sat}} \tag{2.10}$$

The dipole force is simply the gradient of the potential [7],

$$\mathbf{F} = -\nabla U \approx -\frac{\hbar\Gamma^2}{8\delta} \frac{\nabla I}{I_{sat}} \tag{2.11}$$

In this way, a gradient of intensity of far-off-resonant light I corresponds to a force. A simple Gaussian beam has an intensity distribution that is maximum at the center,

which means that, depending on the sign of the detuning, the atom experiences either repulsion or attraction to the radial center of the beam. A single uncollimated beam with negative detuning provides trapping only along the radial direction. A three-dimensional trap may be formed by using a tightly focused beam (as in optical tweezers), a pair of crossed beams, or a retroreflected beam forming a one-dimensional lattice.

In the experiments in this thesis, a 1064-nm one-dimensional lattice is used to trap ground-state Rb atoms. For the Rb atoms in the ground-state ($5S_{1/2}$), the light is attractive because it is red-detuned from the primary transitions available (780nm and 795nm). For the higher-lying levels used in the work here ($5P$, $5D$, and low-n Rydberg states), transitions of both positive and negative detunings must be considered, but ultimately, all of these states are repulsed by the 1064-nm light.

2.3.2 Magneto-optical trap (MOT)

A MOT is formed by three pairs of counterpropagating beams that are circularly-polarized opposite to each other and slightly-red-detuned from an atomic transition, along with a quadrupole magnetic field.

The counterpropagating beams produce a friction force on the atoms via Doppler cooling and a restoring force via the magnetic gradient. For a MOT operating on a $J = 0$ to $J = 1$ transition, the total force of the MOT on an atom along the z-direction is (see Ref. [7])

$$F_{MOT}(z) = \left[4\hbar k \frac{I}{I_{sat}} \frac{2\delta/\Gamma}{[1 + (2\delta/\Gamma)^2]^2}\right] \left(kv + \frac{g\mu_B}{\hbar}\frac{dB}{dz}z\right), \tag{2.12}$$

where $k = 2\pi/\lambda$ is the magnitude of the wavevector of the cooling light, I is the intensity, I_{sat} is the saturation intensity of the transition, δ is the laser detuning from the transition, Γ is the transition rate, $g\mu_B$ is the magnetic sensitivity of the sublevel

of the excited state, and dB/dz is the gradient of the magnetic field.

> *"If [Doppler cooling] were the only force, [the atom] would keep getting colder and colder, till it needed a muffler."*
>
> – Paul Berman

The maximum velocity an atom may have to be captured in the MOT is about $v_c = \Gamma/k$, which corresponds to a temperature on the order of $T_c = \Gamma^2 m/(k^2 k_B)$. Two temperature cooling limits may be relevant. The Doppler cooling limit is the minimum temperature achievable by Doppler cooling alone, $T_D = \hbar\Gamma/(2k_B)$. If other types of cooling are performed (e.g. polarization gradient cooling), an even lower temperature may be reached. The minimum temperature achievable by laser cooling with continuous interaction of the atoms with the light is the one half of the recoil limit T_r, which is given by $T_r = \hbar^2 k^2/(k_B m)$. The three temperatures T_c, T_D, and T_r are given for several cooling transitions of Sr [12] and Rb in Table 2.2.

Transition	$\Gamma/2\pi$ (MHz)	λ (nm)	I_{sat} (mW/cm^2)	T_c (K)	v_c (m/s)	T_D (K)	T_r (K)
(a)	6.07	780	3.6	0.230	4.7	1.5×10^{-4}	3.6×10^{-7}
(b)	30.5	461	40.7	2.1	14.1	7.2×10^{-4}	1.0×10^{-6}
(c)	0.0074	689	0.0030	2.7×10^{-7}	0.0051	1.8×10^{-7}	4.6×10^{-7}

Table 2.2: Some relevant parameters for MOT cooling transitions in Rb and Sr: (a) Rb, $^2S_{1/2} -^2 P_{3/2}$; (b) Sr, $^1S_0 -^1 P_1$; (c) Sr, $^1S_0 -^3 P_1$.

In $^{85(87)}$Rb, the main cooling transition is $5S_{1/2}[F = 3(2)] \rightarrow 5P_{3/2}[F = 4(3)]$. The transition is not closed, i.e. a few atoms are excited from the same initial state to $5P_{3/2}[F = 3(2)]$, and then may escape the cooling cycle by decaying to the lower hyperfine ground state, $5S_{1/2}[F = 2(1)]$. Therefore, a repumper beam on the transition $5S_{1/2}[F = 2(1)] \rightarrow 5P_{3/2}[F = 3(2)]$ is also needed. Creating a MOT for Sr is significantly more complicated because of the electronic structure of the species. For the best cooling and retaining of atoms in the trap, two cooling transitions and one

or more repumping transitions must be used.

CHAPTER III

Rydberg Atoms and Molecules

"Here you are, happy little atom, sitting in the medium. All of a sudden, a pulse comes by and briefly excites you..."

– Paul Berman

3.1 Rydberg atoms

A Rydberg atom is an atom with a valence electron in a highly-excited state. The expanded volume of empty space between the valence electron's shell and the nuclear core has earned them the nickname "fluffy atoms," and their creation has been likened to microwaving popcorn. Because of the small overlap between the far-out Rydberg electron and the inner atomic core, Rydberg atoms are hydrogen-like systems and their energies and wavefunctions can be derived analytically by making small corrections to the corresponding solutions of the hydrogen atom.

Rydberg atoms have a number of interesting and useful properties arising from the large separation between the nucleus and Rydberg electron. They are extremely sensitive to external fields and to each other, making them a prime candidate for DC [5, 13] and radio frequency (RF) electric-field sensors [14, 15] and for imaging tools [16]. The wide selection of Rydberg states available, their relatively close energy spacing, and the fact that external fields can fine-tune their properties, makes Rydberg

atoms impressively versatile and leads to their sensitivity over an extremely wide range of frequencies including the entire RF band [17]. Such high and tunable responsivity to RF fields has generated rapidly-growing interest in exploiting Rydberg atoms for quantum technologies [18] such as quantum communications [19–21], which for a given application may offer various advantages over corresponding classical-based technologies such as superior security, better sensitivity, and smaller physical sizes of the systems. Rydberg atoms are also noteworthy candidates for qubits for quantum information processing (QIP) [22, 23]. It remains to be seen in the coming years and decades how the unique set of advantages and disadvantages of Rydberg atoms for QIP will fare in the race to develop fully-functioning quantum computers.

Besides having direct applications, Rydberg atoms also offer an excellent quantum playground for testing various theories of fundamental physics and exploring novel physics. For the most part, the experiments in this thesis fall in this category. Improving physics knowledge not only spurs the development and new growth of theories, but also indirectly benefits existing technologies (e.g. knowledge of polarizabilities can improve atomic clock performance) and opens doors to imagine entirely new ones.

In a Rydberg atom, the outer electron is much farther away from the nucleus than the other electrons are, which allows the nucleus and electrons to be treated collectively as a singly-charged core. The Rydberg electron energies are then given approximately by a modified Bohr formula where the principal quantum number is replaced by an effective principal quantum number n^*:

$$E_R(n, \ell) = -hc\frac{R}{n^{*2}}$$

where R is the mass-corrected Rydberg constant, $R = R_\infty [M/(m_e + M)]$, where m_e and M are the respective masses of the electron and the inner ionic core, and

the Rydberg constant R_∞ is defined as $hcR_\infty = (e^2/4\pi\epsilon_0)^2 m_e/2\hbar^2$. For Rb, $R = 109736.605\text{cm}^{-1}$ [4]. The effective principal quantum number $n^* = n - \delta_{n\ell j}$ accounts for the distortion of Rydberg electron wavefunction by the core. The quantum defect $\delta_{n\ell j}$ depends primarily on the atomic species and ℓ, but also slightly on n and j. The higher the ℓ, the less the Rydberg electron penetrates the core, and the closer the energies (and wavefunctions) are to those of hydrogen. The Rydberg-Ritz formula gives an expansion for $\delta_{n\ell j}$:

$$\delta_{n\ell j} = \delta_0 + \frac{\delta_2}{(n-\delta_0)^2} + \frac{\delta_4}{(n-\delta_0)^4} + \frac{\delta_6}{(n-\delta_0)^6} + \frac{\delta_8}{(n-\delta_0)^8} + \ldots$$

For example, the quantum defects of ^{85}Rb are listed in Table 3.1.

$n\ell j$	$ns_{1/2}$	$np_{1/2}$	$np_{3/2}$	$nd_{3/2}$	$nd_{5/2}$	nf_j
δ_0	3.1311804	2.6548849	2.6416737	1.3480917	1.3464657	0.016312
δ_2	0.1784	0.2900	0.2950	-0.6029	-0.5960	-0.064007
δ_4	-1.8	-7.904	-0.97495	-1.50517	-1.50517	-0.36005
δ_6	–	116.4373	14.6001	-2.4206	-2.4206	3.239
δ_8	–	-405.907	-44.7265	19.736	19.736	–

Table 3.1: ^{85}Rb quantum defects [24, 25]

The exaggerated properties of Rydberg atoms are reflected in how they scale with n^*. Table 3.2 lists some of the most important scaling laws.

Orbital radius	n^{*2}
Radiative lifetime (low-ℓ)	n^{*3}
Radiative lifetime (high-ℓ)	n^{*5}
Fine structure splitting (low-ℓ)	n^{*-3}
Fine structure splitting (high-ℓ)	n^{*-5}
Kepler frequency	n^{*-3}
Ionization electric field (low-ℓ)	n^{*-4}
DC polarizability	n^{*7}
Transition dipole moment	n^{*2}
Van der Waals interactions	n^{*11}
Electric dipole interactions	n^{*4}

Table 3.2: Scaling Rydberg atom properties with effective principal quantum number.

3.2 Rydberg state excitation and detection

Rydberg atoms may be created by charge exchange, electron impact, and photoexcitation [4]. In this work, the latter method is used. Optical excitation with lasers allows a specific target Rydberg state to be reached by controlling the energy of the incident photon. The cross section $\sigma(n)$ for optical Rydberg excitation is [4]:

$$\sigma(n) = \frac{\sigma_{PI}}{\Delta W n^3}$$

where ΔW is the energy resolution of the excitation. For Rb, $\sigma_{PI} = 0.10 \times 10^{-18}\text{cm}^2$.

In most of the experiments presented here, I detect Rydberg atoms using field ionization, i.e. stripping away the loosely-bound Rydberg electron and collecting the resulting positive ion on a microchannel plate (MCP). Most cold atom experiments similarly field ionize the Rydberg atoms in order to detect them. Some alternative and non-destructive methods are optical and based on electromagnetically induced transparency (EIT), which can allow detection of the Rydberg level structure [26] or of the Rydberg state population [27].

3.2.1 Rydberg atoms in optical lattices

Rydberg atoms behave differently in optical lattices than ground-state atoms because their sizes are comparable with optical wavelengths. In this regime, the light shift comes from the ponderomotive potential V_P of the quasi-free electron that is driven by the far-off-resonant light to rapidly oscillate. The ponderomotive potential is

$$V_P = \frac{e^2|\mathbf{E}|^2}{4m_e\omega^2}. \tag{3.1}$$

The potentials experienced by Rydberg atom are a spatial average of the position-dependent ponderomotive energy over the spatial extent of the Rydberg electron. When V_P is large compared to the energy separation between states of different ℓ

and the Rydberg atom diameter is on the same scale as the lattice periodicity (such that the potential varies significantly over the span of the Rydberg electronic wavefunction), the lattice mixes the ℓ states. For high-angular-momentum states, whose electronic wavefunctions are of different shapes, the lattice breaks the state degeneracy and creates a rich structure.

3.3 Rydberg molecules

Rydberg molecules [28] are molecules in which one or more of the atoms is in a Rydberg state. They have binding mechanisms that are unique compared to any other type of molecule, and have exotic properties including extremely long bond lengths and large dipole moments. Several classes of Rydberg molecules exist, including those bound by the scattering interaction of a Rydberg atom's electron with a ground-state atom, multiple Rydberg atoms bound by a long-range multipolar interaction, and molecules consisting of Rydberg atoms and ions. The first class are the earliest-discovered [28, 29] and have received the most attention. A nice review is given in Ref. [30]. They are the type I summarize here and experimentally investigate in Chapter V.

The Rydberg molecule system formed by a Rydberg atom and a ground-state atom consists of three bodies: an ionic core with a Rydberg electron that mediates the interatomic bond by its local interaction with the ground-state atom. The ground-state atom perturbs the Rydberg electron wavefunction, which leads the molecular potential energy curves to be oscillatory and correspond to the wavefunction density of the Rydberg electron. The strength of the interaction depends on the relative kinetic energy of the electron and atom, as well as their relative spin orientation. This class of Rydberg molecules can further be divided into three subclasses: 1) trilobite molecules [31], in which the Rydberg electron occupies a superposition of hydrogenic states, 2) butterfly molecules [32], whose potentials arise from the p-wave shape res-

onance present in alkali-metal atoms, and 3) low-ℓ Rydberg molecules [29]. Trilobite and butterfly Rydberg molecules possess electric dipole moments on the order of 1 kilodebye, while for low-ℓ Rydberg molecules they are on the order of 1 debye.

CHAPTER IV

Experimental Setup

"Now you have all the tools you need in Life!"

– Paul Berman

The following chapter details the experimental setup and techniques. A key feature of the experimental apparatus is its in-vacuum optical cavity, which sustains a 1064-nm one-dimensional optical lattice. At the center of the lattice region, a magneto-optical trap (MOT) is produced and provides the initial cooling and collection of the atoms before they are loaded into the lattice. The lattice trap forms an elongated, dense atomic cloud [full-width half-maximum (FWHM) of the density distribution about 18 μm, length up to 1.6 mm].

The optical lattice serves multiple purposes for the experiments described in this work. In the Rydberg molecule experiment, though the lattice is off during the excitation, the lattice increases the atomic density in the excitation region, which is necessary for the photo-association rate to be large enough such that molecular states become observable. Additionally, unlike some setups for studies of Rydberg molecules, this setup facilitates either Rb isotope to be cooled and trapped, and allows high repetition rate for the experimental cycle (100 Hz). In the lattice-mixed-Rydberg-state experiment and polarizability experiment, the lattice light is on during excitation

and induces massive (∼GHz) light shifts. In the former experiment, the light shifts mix Rydberg F character into the hydrogenic manifold, so that the hydrogenic states may be reached with a three-photon transition and no additional fields. For the polarizability experiment, the relative difference in light shifts in the $5P$ and $5D$ levels allows an extraction of the $5D$ polarizabilities.

Much of the setup has been described in a previous thesis [33] and is only briefly reviewed here, while the more recent additions and improvements are described in more detail. The primary changes consist of 1) a frequency-tracking mechanism with improved accuracy for spectroscopic measurements, 2) an avalanche photodiode for sensitive measurements of light absorption, and 3) the addition of five new laser systems and corresponding setups for their frequency control.

4.1 Magneto-optical trap

In each of the three experiments, a Rb atom reservoir is heated to produce an atomic vapor which then fills the connected vacuum chamber. The atoms are prepared in MOT and loaded into a spatially overlapping 1-D optical lattice.

The MOT light source is an amplified distributed Bragg reflector (DBR) laser system (linewidth ~ 1 MHz), operating close to the $5S_{1/2} \rightarrow 5P_{3/2}$ transition. The MOT repumper is a homemade external cavity diode laser (ECDL). A second, identical amplified DBR laser system is used for absorption imaging of the atoms and also for coupling the $5S_{1/2}$ and $5P_{3/2}$ levels when performing two-photon Rydberg excitation.

Each of the three aforementioned 780-nm lasers may be locked at a frequency close to the respective atomic resonance using saturation absorption spectroscopy on a reference Rb vapor cell.

4.2 Intracavity, near-concentric optical lattice

The central component of the setup is an in-vacuum, 1064-nm, 1-D optical lattice in a near-concentric cavity. The cavity was designed and built by Yun-Jhih Chen and is well-described in her thesis [33].

4.2.1 1064-nm laser

The light used in the cavity is produced by a cw narrow-band laser (IPG Photonics YLR-10-1064-LP-SF) at wavelength $\lambda = 1064$ nm. I repaired the laser unit once, when one of its internal power modules failed and caused the laser to completely stop functioning.

Though the laser has a short-term linewidth of 100 kHz, it has large fluctuations on the timescale of seconds and of minutes. Instead of stabilizing the 1064-nm frequency, the cavity length is actively controlled to match the fluctuating frequency, as will be described in more detail.

4.2.2 Design of the cavity

The cavity is a near-concentric design, meaning that the locations where each of the two mirrors focus are both nearly at the midpoint between the mirrors, i.e. the distance between the mirrors L is about equal to twice the radius of curvature of the mirrors r. The mirror locations are intentionally offset slightly closer together in order to make the cavity stable (i.e. robust against small angular misalignment) so that $L = 2(r - \delta)$. The concentric type of cavity was chosen because it has the highest intensity contrast between the intensity at the center, where the atoms are located (and thus the benefit of intensity is maximal), and the intensity at the mirror surfaces, where there is a risk of damage.

A pair of coupling lenses focuses the 1064-nm beam at the center of the cavity. The focal length of the lenses (40 mm) was selected to best match the waist of the

incoming beam.

An estimate of the displacement δ and of other cavity parameters was made by measuring the splitting between a Hermite-Gaussian (HG) mode and the HG mode closest in frequency ($\Delta\nu_A - \Delta\nu_T$) compared to the splitting between two of the same HG modes at sequential orders ($\Delta\nu_A$). Their ratio ($\Delta\nu_A - \Delta\nu_T/\Delta\nu_A$) approximately equals $\frac{2}{\pi}\sqrt{\frac{\delta}{r}}$. Since the mirror radius r is assumed to be as specified by the manufacturer, a value of δ (or equivalently, L) may be extracted. The measured ratio of 0.030 ± 0.014 translates to $\delta \approx 0.056$mm and $L \approx 49.9$mm. When r and δ are known, the free spectral range (FSR) and beam waists at various locations may also be derived. The relations are shown in Table 4.1 (see also Ref. [33]).

	Notation	Relation(s)	Value
Mirror radius	r	–	25 mm
Axial-transverse ratio	$\frac{\Delta\nu_A - \Delta\nu_T}{\Delta\nu_A}$	–	0.030(14)
Displacement of each mirror relative to position for perfect concentric-cavity	δ	$\frac{r}{2} + \frac{r}{2}\cos\left[\pi\left(1 - \frac{\Delta\nu_A - \Delta\nu_T}{\Delta\nu_A}\right)\right]$	0.06(5) mm
Free spectral range; Axial mode spacing	FSR; $\Delta\nu_A$	$c/2nL \approx c/4r$	3.0 GHz
Axial mode spacing minus transverse mode spacing	$\Delta\nu_A - \Delta\nu_T$	$\frac{c}{2nL}\left[1 - \frac{1}{\pi}\cos^{-1}\left(1 - \frac{L}{r}\right)\right] \approx \frac{c}{2r\pi}\sqrt{\frac{\delta}{r}}$	90(42) MHz
Beam waist at cavity center	w_0	$\sqrt{\frac{L\lambda}{n\pi}\sqrt{\frac{r}{2L} - \frac{1}{4}}} \approx \sqrt{\frac{r\lambda}{\pi}\sqrt{\frac{\delta}{r}}}$	20(5) μm
Beam waist at cavity mirrors	w_1	$\sqrt{\frac{L\lambda}{n\pi}\sqrt{\frac{r^2}{2Lr - L^2}}} \approx \sqrt{\frac{r\lambda}{\pi}\sqrt{\frac{r}{\delta}}}$	420 μm (+160/-70)μm
Optimal beam waist at input (outside of focusing lenses)	w_1'	$2.411 w_1$	1020μm (+380/-180)μm

Table 4.1: Cavity geometric parameters

The performance of cavity depends on the optical properties of the mirrors. The absorption and transmission of the mirrors were measured to predict the finesse and coupling efficiency, as well as the optical circulating power, which is useful for estimating optical intensity. These parameters are compiled in Table 4.2 (see also Ref. [33]).

	Notation	Definition	Value
Reflection, specified	R		$> 99.5\%$
Absorption, measured	A_{meas}		0.28%
Transmission, measured	T_{meas}		0.14%
Finesse,	$\mathcal{F}$		
theoretical		$\pi\sqrt{R}/(1-R)$	> 630
actual			600
Coupling Efficiency,			
for perfect beam mode		$T_{meas}^2/(A_{meas}+T_{meas})^2$	11%
typical measured			$< 11\%$
Circulating-power-to-transmitted-power ratio	$\frac{P_0}{P_{trans}}$		
for lossless mirrors & optics		$\mathcal{F}/\pi$	200
accounting for losses		$\sim (0.9 \cdot T_{meas})^{-1}$	790

Table 4.2: Cavity optical parameters

The optical intensity is a very important metric, as it determines the light shifts of the trapped atoms; however, it cannot be measured directly. A good estimate of the intensity at a given time can be made by using the approximate beam waist at the trap center (w_0) along with the ratio of the circulating power to the transmitted power (P_0/P_{trans}), and measuring the transmitted power. The ratio of powers, although it has some uncertainty, is particularly helpful because it is a fixed relation and enables the transmitted power to be used as an intensity reference. In contrast, the coupling efficiency is not fixed because it is sensitive to the alignment of the beam into the cavity.

The maximum optical intensity at the location of the trapped atoms is twice the average intensity which is in turn twice the circulating intensity, since the sinusoidal

electric field (standing wave) of the light doubles at its antinodes, such that:

$$I_{max} = 2I_{avg} = 4I_{cir} = 4 \times \frac{2P_0}{\pi w_0^2}$$

The ratio of I_{max} to the power that is transmitted through the cavity is then:

$$\frac{I_{max}}{P_{trans}} = \frac{8}{\pi w_0^2} \times \frac{P_0}{P_{trans}}$$

Using the values in Tables 4.1 and 4.2, I_{max} is estimated to be about $5.0(+4.4/-1.6) \times 10^9$ W/m^2 per mW of transmitted power.

An alternative method to estimate the optical intensity at the atoms is to use the atoms themselves. The trapped atoms experience a light shift proportional to their state polarizability and the light intensity at the location of the atoms. The ratio of the ground-state light shift to the transmitted power is estimated to be 18 MHz/mW. Using the theoretical value of the ground-state polarizability at 1064nm ($687.3(5) \times 4\pi\epsilon_0 a_0^3$ [34]), this translates to 9.9×10^8 W/m^2 per mW of transmitted power. The biggest uncertainty contribution is that of axial mode spacing. There is also uncertainty in the transmission of the cavity mirror and the subsequent optics (lenses and vacuum chamber windows) that the beam passes through before being measured, and uncertainty in the power measurement itself.

The maximum achievable intensity in the cavity is primarily limited by the reflectivity of the cavity mirrors. Absorptive and scattering losses limit circulating power for an input beam of fixed power and geometry, and absorptive loss also effectively restricts the power the cavity is likely to sustain without damage. The intensity could be improved by replacing the mirrors with ones that have extremely low absorptive loss. For example, the recently-developed technology of single crystal dielectric coatings are quoted to have absorptive and scattering losses less than a few ppm [35], which is nearly three orders of magnitude better than the mirrors in the existing

setup. The coupling efficiency of the input light could also be improved by using a spatial light modulator to correct the phase front of the beam.

4.2.3 Control of the cavity

The cavity mirrors are mounted on piezos for fine control of the cavity alignment. The top mirror of the vertical cavity is mounted on a ring piezo, and the bottom mirror is mounted on a set of three piezos, in a tripod configuration, with different surfaces (one with a flat surface, one with a V-shaped groove, and one with three sapphire balls). The ring piezo is used for active stabilization of the cavity length so that a Gaussian cavity mode frequency matches the laser frequency while the laser frequency passively drifts. One of the tripod piezos is used to manually adjust the cavity mode to be near the appropriate laser frequency before the ring-piezo lock is turned on.

4.2.4 Atomic density in the lattice

The atomic density in an optical dipole trap loaded from a MOT depends on many factors including the dipole trap waist and depth, the MOT background density, the intensities and detunings of the MOT primary and repumper light, and the loading time [36]. The lattice loading becomes very inefficient when the depth exceeds about 50 MHz. The atomic density in the lattice trap here is estimated via absorption imaging. The observed area density and diameter of the atomic cloud are used to calculate the volume density assuming cylindrical symmetry. An optimized density using a trap at a shallow, constant depth (∼30 MHz) was found with this method to be $\approx 2 \times 10^{11}\mathrm{cm}^{-3}$ [33] in the center of the trap. The actual maximum density is expected to be about 4 times higher due to the longitudinal compression in the lattice sites, which is not resolvable with the absorption imaging. When the light intensity of the dipole trap is dynamically ramped for tens of microseconds before the atoms

are probed, even higher densities may be acquired [33].

4.3 Lasers for Rydberg excitation

4.3.1 Laser wavelengths and basic designs

Two different schemes for Rydberg excitation are used for the experiments described in this thesis (shown in Fig. 4.1). The first is a two-photon excitation through the intermediate state $5P_{3/2}$, by which nS or nD Rydberg states are accessible with a 480nm laser. The second is three-photon excitation through the intermediate states $5P_{1/2}$ and $5D_{3/2}$ and reaches nP or nF states via light around 1260-1290nm. The first scheme is logistically simpler since it requires one laser fewer, and had already been set up for previous experiments. The second scheme was implemented particularly with the lattice-mixed-Rydberg-state experiment in view, since in Rb, the nF states lie closer to the nearest hydrogenic manifold than the nS or nD states do and are mixed more strongly with them (as explained in more detail in Chapter VII). Furthermore, whereas the $5P_{3/2}$ state has already been measured [37], the second scheme will allow a polarizability measurement and photoionization cross-section measurement of a new state, i.e. $5D_{3/2}$; this is discussed in Chapter VI.

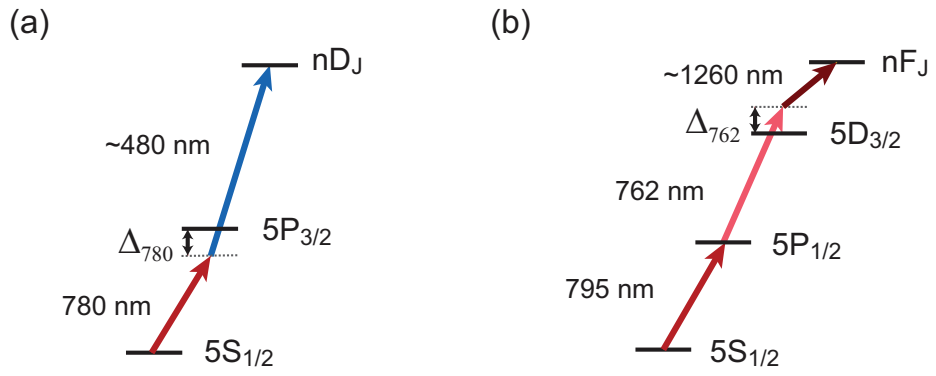

Figure 4.1: Level diagrams of two schemes used for Rydberg excitation in Rb. (a) Two-photon excitation used for the Rydberg molecule experiment. (b) Three-photon excitation used for the lattice-mixed-Rydberg-state experiment.

For the two-photon Rydberg excitation, the 780-nm light is provided by a DBR laser that has the same design as the 780-nm MOT laser. The 480-nm light comes from a tunable 960-nm laser that is amplified with a tapered amplifier (TA) and subsequently frequency-doubled in a second-harmonic-generation (SHG) cavity. The 780-nm light is typically detuned from the intermediate state by 500-1000 MHz in order to diminish scattering-induced heating.

For the three-photon scheme, the two red lasers (795nm and 762nm) used for excitation are compact ECDLs. Two additional 795nm and 762nm ECDLs are used as frequency references. The four lasers are also used in the polarizability measurement experiment, in which there are no Rydberg excitations. The 1260-nm laser provides excitation light for the final step to the Rydberg states in the lattice-mixed-Rydberg-state experiment. It is a widely tunable (1230-1290nm) ECDL with a cateye design.

In the lattice-mixed-Rydberg-state experiment, the 795nm is at or near resonance with the first intermediate state ($5P_{1/2}$), which is AC-Stark shifted by the high intensity 1064-nm light. The 762-nm light is kept off-resonance from the second intermediate state ($5D_{3/2}$) to prevent population in it. Avoiding population of the $5D_{3/2}$ state is desired since the atoms would ionize easily via both Penning ionization and photoionization from the 1064-nm light.

4.3.2 Locking and scanning the laser frequencies

The primary experiments described in this thesis are spectroscopy experiments, in which one of the excitation laser frequencies is scanned, and a signal—in the present case, typically ion counts—is recorded. To adequately explore the physics in view, the frequency scans must be at least several hundreds of MHz, and in some cases multiple GHz. Adjusting a laser frequency over this range with high precision (both of the scanning steps and of the absolute frequency), can prove to be a significant experimental challenge.

On a similar note, even the frequency locking of the excitation lasers that are not scanned requires extra consideration. In a typical setup for laser excitation, the lasers are stabilized at or near the resonances of the atomic transitions, which usually makes it straightforward to use the atomic transitions as absolute frequency references (for example, performing saturation absorption spectroscopy in separate vapor cells). Acousto-optic modulators (AOMs) may provide an offset of at most a few hundred MHz from the transition and a scanning range of tens of MHz. However, for the polarizability and lattice-mixed-Rydberg-state experiments, the transitions of the atoms in the experiment chamber are shifted on the order of GHz from the field-free transitions, which means that the lasers must be stabilized at a greater offset than usual from the field-free transitions.

4.3.2.1 Locking and scanning with Fabry-Pérot interferometers (FPIs)

Several FPIs are used in the experiments.

Fixed-FSR FPI for 780nm In the long-range Rydberg molecule experiment, the atoms are not AC Stark shifted, but a large detuning from the intermediate state is still desired. To accommodate this, the red lower excitation ($5S_{1/2} \rightarrow 5P_{3/2}$) laser is locked to a reference signal from an FPI cavity. The FPI has no mechanism for tuning its FSR (except on long timescales by changing the temperature of the system). To estimate the absolute frequency offset, the FPI resonances are compared to the atomic transitions. The same FPI has been used for the 795-nm and 762-nm lasers previously, but their frequency control has since been replaced with a more versatile method (see subsection 4.3.2.2).

Pressure-tuned FPI for 960nm The 960-nm laser for the blue upper-transition ($5P_{3/2} \rightarrow 24D_J$) is locked to a separate FPI, which is constructed such that its resonances may be tuned by controlling the internal air pressure using a motorized linear

stage. The FPI's tunability and calibration are of critical importance to the Rydberg molecular binding energy measurements that were made, and they are explained in detail in Appendix B.

FPI with fiber electro-optic modulator (EOM) for 1260nm The 1260nm uses a third FPI. A portion of the beam is split off and sent through a fiber EOM, which adds frequency sidebands via an RF signal generator. The EOM is capable of modulating the 1260nm beam up to 20 GHz (in first order; higher orders are also produced). One of the sidebands of the modulated beam is locked to the FPI. When the RF is scanned, the frequency of the sideband stays constant while the unmodulated beam frequency follows the scan. As an alternative to the FPI, an electromagnetically induced transparency (EIT) lock with a Rb vapor cell (similar to the scheme in Ref. [38] may be used.

Limitations Using FPI resonances for locking the lasers has a few potential drawbacks in general. The absolute frequency offset information takes a few minutes to obtain. FPIs are subject to small temperature fluctuations (having already been diminished by active temperature stabilization), which can cause the resonances to fluctuate within $\sim$1 MHz. Perhaps the most significant limitation is that the two FPIs that are usable for the red and 1260-nm lasers are not tunable. Fortunately, all of these factors are negligible for the Rydberg molecule experiment and manageable for the others.

4.3.2.2 Locking and scanning with optical phase-locked loops (PLLs) for 795nm and 762nm

Optical phase-locked loops (PLLs) offer the ability to lock and scan a laser to a second laser with GHz offset frequencies and extremely high precision. A tradeoff is that each PLL requires an extra laser and as well as extra electronics and significant

time to set up. I use two PLLs, one for 795nm and one for 762nm.

A diagram of setup of the phase-locked loops is shown in Fig. 4.2. In each master-slave system, a beam is split off from each of the two lasers. The two split-off beams are aligned to spatially interfere on a photodiode (PD). The AC component of the PD signal is amplified and sent to an offset phase lock servo (OPLS) and compared to a RF signal that is at a controlled frequency. The output of the OPLS is attenuated and fed to the current control of the slave laser. The master lasers are also each locked to atomic vapor cell references. The 795-nm master laser uses a typical saturati on absorption spectroscopy scheme, while the 762-nm laser is referenced to an EIT signal where the stabilized 795-nm laser is used as a fixed-frequency EIT probe on the $5S_{1/2} \rightarrow 5P_{1/2}$ transition. The EIT coupler (762-nm laser) is locked on the EIT resonance. To allow for peak locking, each of the atomic references are modulated through an oscillating magnetic field that is produced by modulating the current through wires coiled around the vapor cells.

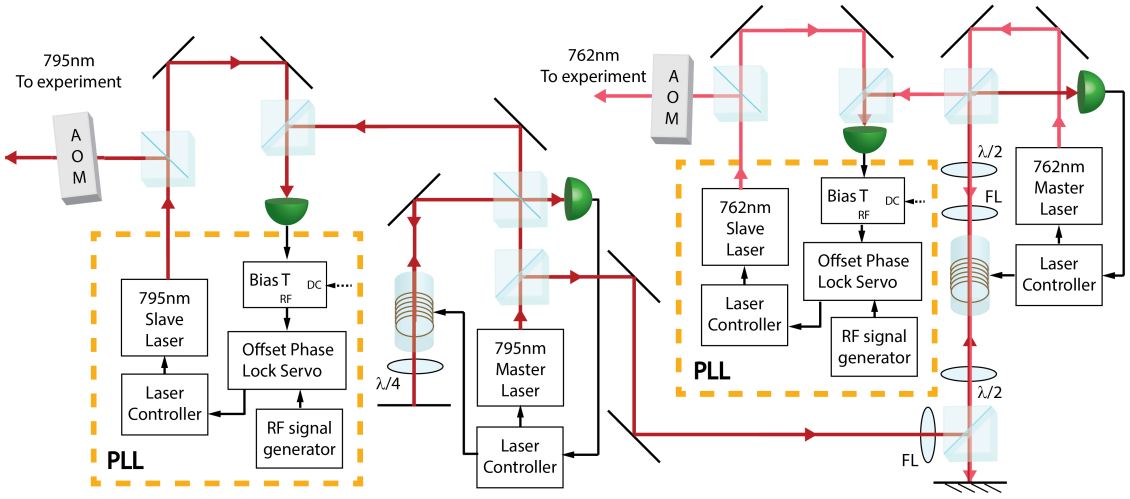

Figure 4.2: Setup of phase-locked loops (PLLs) and atomic frequency locks. Green semi-spheres denote photodiodes. AOM, Acousto-optic modulator; FL, focusing lens; $\lambda/2$, half-wave plate; $\lambda/4$, quarter-wave plate.

The level diagram of the two isotopes and the transitions accessed by the four lasers are shown in Fig. 4.3. The available scan ranges of the offset phase lock servos

(D2-135, Vescent Photonics) have minimum offsets of hundreds of MHz. In order for the slave lasers to be able to access the field-free resonances as well as the whole range of light-shifted resonances, the master lasers are locked to transitions of the other Rb isotope (^{87}Rb). The 795-nm master laser is locked to a transition lower in frequency than the primary ones to be accessed by the slave laser, and the 762-nm to a higher-frequency one. In this way, each laser may respectively access its entire relevant range without ever requiring its PLL offset frequency to be too small.

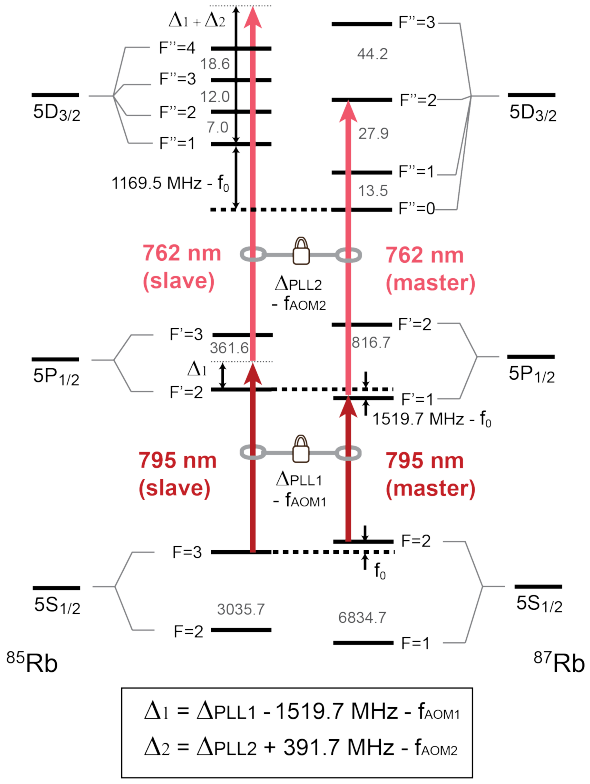

Figure 4.3: Level diagram and laser locking scheme of excitation master and slave lasers. The master lasers are locked to atomic vapor cells on ^{87}Rb lines. The slave lasers are PLL-locked to the master lasers, and passed to the atoms in the lattice via AOMs, as shown in Fig. 4.2. The slave lasers drive transitions in ^{85}Rb and are scanned via scanning the RF sources in the PLLs. Numbers in gray are hyperfine splitting frequencies in MHz. Each relative frequency between a master laser and a slave laser is the PLL offset frequency plus an offset from an AOM. The relations between the PLL frequency offsets and the detunings of the slave lasers from the field-free resonances, accounting for the isotope differences and the AOM offsets, are shown in the box. The relative frequencies are mainly derived from Ref. [39] as well as Ref. [40–43].

The laser detunings Δ_1 and Δ_2 should be chosen to be able to access the transitions up to the expected maximum light shifts ($\sim +1.5$ GHz for 795nm and ~ -0.5 GHz for 762nm), and for transitions through both intermediate hyperfine states ($5P_{1/2}$ $F' = 2$ and $F' = 3$), which are 360 MHz apart. Then the target PLL offset frequencies may be found using the relation in Fig. 4.3. Accordingly, we find:

$$\Delta_1 = 0 \text{ to } +1.86 \text{ GHz} \longrightarrow \Delta_{PLL1} - \mathrm{f}_{AOM1} = +1.52 \text{ to } +3.38 \text{ GHz}$$

$$\Delta_2 = 0 \text{ to } -0.86 \text{ GHz} \longrightarrow \Delta_{PLL2} - \mathrm{f}_{AOM2} = -0.39 \text{ to } -1.25 \text{ GHz}$$

The 16x multiplier setting on the OPLSs permits a range of $480 - 3840$ MHz, which fully covers both of the PLL offset frequency ranges. At this setting, the RF generators should be set at 1/16th of the target frequencies, i.e. 85-201 MHz for 795 nm and 54-108 MHz for 762 nm.

4.3.3 Summary

Table 4.3 shows a summary of the ten lasers used in the primary experiments.

4.4 Electric field control

Six independent electrode rods around the perimeter of the 1064-nm cavity allow control of electric fields in the two dimensions transverse to the lattice. The electrodes serve several purposes. First, they compensate for small stray electric fields (to which Rydberg atoms are very sensitive). Ref. [33] explains how the compensation voltages are found in this setup using Stark spectroscopy. Secondly, the electrodes can apply fields up to about 130 V/cm. The fields can be applied during laser excitation (e.g. for studying dipole moments of Rydberg molecules), and/or the fields can ionize some Rydberg states post-excitation (for example, fields at the specified strengths can ionize low-angular-momentum states with principal quantum numbers ranging

λ (nm)	Type	Purpose	Lock signal	Feedback applied to	Scanning mechanism (while locked)	Exp Mol. Hyd. Pol.
780	DBR	MOT cooling	SS	current	–	✓✓✓
780	ECDL	MOT repumper	SS	grating	–	✓✓✓
1064	Fiber	Lattice trap and level shifts	reflection from cavity (PDH error)	slow: cavity ring piezo fast: AOM FM	–	✓✓✓
780	DBR	Excitation ($5S_{1/2} - 5P_{3/2}$)	SS or red FPI	current	–	✓
∼480 (after doubling)	ECDL	Excitation ($5P_{3/2} - nD$)	FPI for 960nm	grating	FPI pressure-tuned by linear stage	✓
795	ECDL	Frequency reference	SS	grating & current	–	✓✓
795	ECDL	Excitation ($5S_{1/2} - 5P_{1/2}$)	beat note w/ other 795	current	RF generator (using PLL)	✓✓
762	ECDL	Frequency reference	EIT on ^{87}Rb line	grating & current	–	✓✓
762	ECDL	Excitation ($5P_{1/2} - 5D_{3/2}$)	beat note w/ other 762	current	RF generator (using PLL)	✓✓
∼1260	ECDL (Cateye)	Excitation ($5D_{3/2} - nP/nF$)	FPI for 1260nm	grating	Fiber EOM	✓

Table 4.3: Lasers in primary experiments with their relevant locking and scanning mechanisms (SS = saturation absorption spectroscopy; FPI = Fabry-Pérot interferometer).

from the 40s and above). Thirdly, the electrodes help to steer the ions toward the MCP detector.

4.5 Detection Methods

For the experiments in this thesis, the primary ways of making quantitative assessments of the atoms and molecules are by counting the ions originating from excited states and sometimes by measuring the absorption of on-resonance light. It is also useful to monitor the atoms by imaging their fluorescence in the MOT, but this signal is generally more complicated to interpret quantitatively.

4.5.1 Ion detection and time of flight imaging

The primary data signal is an ion count rate, which destructively measures some atomic and molecular states. It usually corresponds to the number of Rydberg products (atoms or molecules) that had been present previously, because the Rydberg electrons have energies close to the ionization threshold and in most cases ionize very easily compared to lower-energy states. The $5D_{3/2}$ states, whose valence electrons already have about 75% of the energy needed for ionization, also ionize fairly easily and are detected via ion counts in the polarizability experiment (Chapter VI). Depending on the details of the scenario, the ions from Rydberg or $5D_{3/2}$ states may be formed through a variety of physical processes. Ionization may be induced by applying external fields, i.e. electric-field ionization (for Rydberg states) or 1064-nm photoionization. It can also happen spontaneously through black-body photoionization or through collisions of excited atoms (via processes such as Penning ionization, Hornbeck-Molnar ionization, or ion pair formation [44–46]).

An MCP detector [47] pulls in the positive ions by the very large negative voltage on its front plate. The collision of an ion on the plate releases a large number of electrons, which create an electric field pulse. The high-frequency component of the

pulse is detected and counted by a photon counter as a single event. If desired, further information about the Rydberg state that generated the ion and/or about the ionization process can be gained from the spatial location of the ion collision on the MCP front plate [48] and/or from the timing of its collision. The timing of the ions' arrivals is used to distinguish Rb^+ from $Rb_2{}^+$, for example, in the Rydberg molecule experiment (see Fig. 5.2). The timing information also has the potential to be used in combination with a ramped field-ionization pulse to discriminate among Rydberg states of different quantum numbers [49].

4.5.2 Absorption detection

To perform absorption imaging, light on resonance with $5S_{1/2} \rightarrow 5P_{3/2}$ (780nm) or $5S_{1/2} \rightarrow 5P_{1/2}$ (795nm) is sent through the atom cloud and the exiting intensity I is monitored. The initial probe intensity I_0 is set to be low compared to saturation intensity of the transition, I_{sat}.

The area density n_A may be found from the relation [33]

$$n_A = \frac{2I_{sat}}{\Gamma h\nu} \ln \frac{I_0}{I}, \tag{4.1}$$

where Γ is the decay rate of the transition and $h\nu$ is the transition energy. The volume density may be estimated by estimating the depth (in length units) of the atom cloud (for example, by making use of its observed geometry in the plane of the camera).

4.5.2.1 Absorption imaging with cameras

One camera views the side of the experimental region (i.e. transverse to the dipole trap), and another views the lattice longitudinally from above. Images from the side camera such as those in Fig. 4.4 are used to qualitatively monitor the atomic densities in real-time or to quantitatively estimate them. The top camera shows the

position of the dipole trap within the MOT. It may be used for absorption imaging, or more interestingly, to probe radiation guiding effects of the elongated cloud [33]. An absorption image from the top camera is also shown in Fig. 4.4.

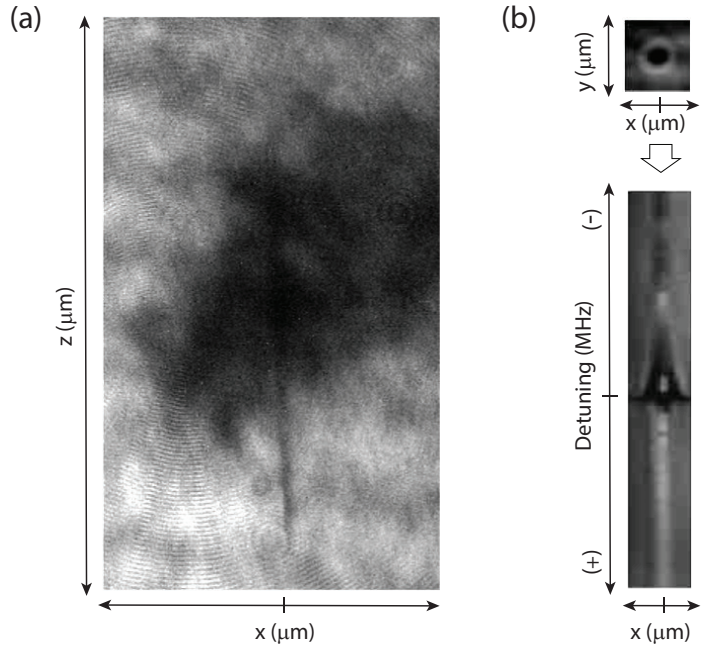

Figure 4.4: Absorption imaging of 780nm with cameras. (a) A typical absorption image of the dipole trap (and MOT) from the side view [(x, z) plane] of the dipole trap. The large dark region shows atoms in the MOT, while the even darker, narrow vertical strip shows atoms in the optical lattice dipole trap. (b) A series of absorption images of the dipole trap from the top view [(x, y) plane] such as the image at the top are recorded at various detunings spanning -520 MHz to $+480$ MHz. To illustrate how the images vary with detuning, the horizontal strip of pixels at $y = 0$ for each detuning are joined together to form new picture (lower right). Each horizontal strip corresponds to an image with a pattern of concentric rings of various brightness and darkness.

4.5.2.2 Absorption spectroscopy with avalanche photodiode (APD)

An avalanche photodiode (APD) is placed along the path in which the red excitation beams exit the chamber. The APD can detect light at very low powers with excellent sensitivity. It is convenient for optimizing the overlap between the excitation beams and the dipole-trapped atoms, because the high density of atoms in the dipole trap cause higher absorption of the light. It is also useful as a way to probe

the AC Stark shifts caused by the dipole trapping light without requiring excitation to higher energy levels or the use of the MCP. Example spectra recorded by the APD are shown in Fig. 4.5.

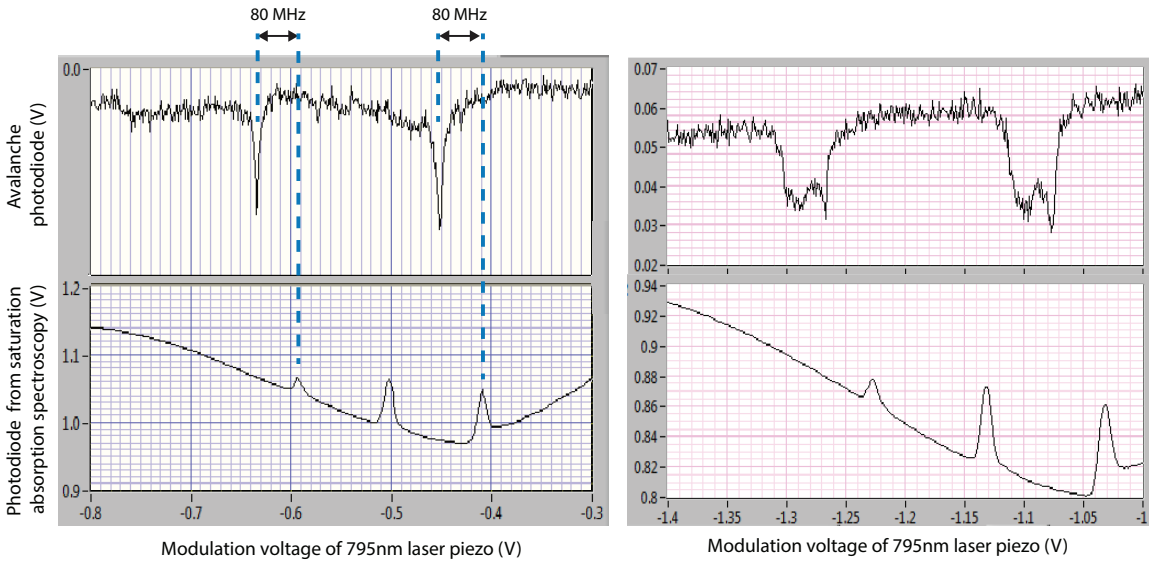

Figure 4.5: Absorption spectra of the atoms in the chamber using a 795nm beam shifted by 80 MHz from an AOM, and the APD (top row). Signals from saturation absorption spectroscopy are shown in the bottom row. During the excitation, the 1064-nm lattice is off (left column) or on at low power (right column). The extra peaks in the top right spectrum originate from atoms trapped in the lattice, which experience AC Stark shifts. In all cases, the frequency is changed by scanning the voltage of the laser piezo (positive change in voltage corresponds to negative change in frequency) but has been similarly done using the 795nm PLL.

CHAPTER V

Long-Range Rydberg Molecules

"You're a happy little atom. A pulse comes by, it's the highlight of your day."

– Paul Berman

5.1 Overview and motivation

In this chapter, I describe an experiment in which I examined Rydberg molecules for eight different spin couplings. The experiment forms a core part of this thesis. Much of the material in this chapter has been published in Ref. [50]. Here, I provide more details. In particular, I expound further upon the methods we used to extract scattering length functions from the molecular resonance measurements, and upon the relevance of atom cloud temperature in photoassociation in this experiment.

The Rydberg molecules studied here are bound by the scattering of a Rydberg electron and a neutral ground-state atom. The ground-state atom is embedded in the electron orbital of a Rydberg atom, and the scattering interaction "happens" as the Rydberg electron repeatedly collides with it. This is a unique mechanism of forming a molecular bond [28]; it is fundamentally different from the covalent, ionic, or van der Waals bonds which form all other molecules. The molecular states are most accurately termed "resonances" instead of "vibrational states" because the molecules undergo tunneling-induced decay where the ground-state atom crosses through the

potential barrier to the Rydberg-atom nucleus. Thus, the states have an energy width and Breit-Wigner resonance.

The molecular binding energies depend on very-low-energy electron-atom scattering properties (in the sub-50-meV range). Measurements of the binding energies can validate calculations of the scattering phase shifts and the structure of negative-ion resonances [51–54]. Studying low-energy-electron scattering using electron and molecular beams is difficult due to inherent energy spreads and space-charge electric fields. Rydberg molecules present an attractive, experimentally accessible alternative [29, 55–63], in which electric fields can be eliminated using Rydberg Stark spectroscopy [4]. Thus these molecules emerge as a testbed for low-energy electron-atom scattering [64–69]. Low-energy electron scattering is also of broad interest. For instance, it can cause DNA strand breaks through the formation of negative-ion resonances [70–74].

I probed $(24D_J{+}5S_{1/2})$ molecular resonances for ^{85}Rb and ^{87}Rb and measured binding energies up to 440 MHz with fractional uncertainties as low as 0.2% for the most deeply-bound states. Compared to standard molecules, these binding energies are extremely small (by a factor of about a million), but compared to other Rydberg-ground molecules they are large due to the low principal quantum number selected for the Rydberg state ($n = 24$). The 0.2% uncertainty compares favorably with other experiments in the field, and small uncertainties map into the ability to better estimate the underlying electron-atom scattering phase shifts.

In Rydberg-ground molecules, there are four coupled spins: the spin and the angular momentum of the Rydberg electron, the electron spin of the ground-state atom, and the nuclear spin of the ground state atom. Because there are two isotopes of Rb that are experimentally accessible (in contrast to cesium, for example), twice the number of spin coupling conditions are available. I observe isotopic effects in the binding energies arising from the different nuclear spins as well as from the slightly

different nuclear masses.

Because diatomic Rb Rydberg molecules are two-electron systems (one valence electron from each of the two atoms), there are both singlet and triplet scattering channels, which are very different because of the exchange interaction. In the present case as well as the typical one, only the $l = 0$ and $l = 1$ partial waves of the scattering matter for Rydberg molecules. Thus, there are a total of four relevant scattering phase shifts functions because higher-order partial waves ($l \geq 2$) may usually be safely neglected. Two interesting exceptions are i) when the perturber has a d-wave or f-wave shape resonance [75] and ii) a predicted class of Rydberg molecules where the internuclear distances are significantly smaller than the size of the Rydberg electronic wavefunction [76]).

In this work, a semi-empirical model is developed relating the scattering phase shift functions to the binding energies. By tuning the scattering phase shift parameters, the observed binding energies are fit to 3.8 MHz rms deviation. Because the vibrational molecular resonances involve different spin configurations and cover a wide range of internuclear separations, the resonances have different dependencies on the s-wave and p-wave scattering phase shifts for singlet and triplet scattering. Consequently, fitting the spectroscopic data enables comprehensive determination of all four scattering phase shift functions over the relevant energy range as well as the zero-energy scattering lengths (directly related to the scattering phase shifts) of the two s-wave channels.

Compared to other Rydberg molecule experiments, in this setup the atom temperature is unusually high (180 μK) and the density is unusually low (1×10^{11} cm^{-3}). The production of Rydberg molecules in these conditions suggest that the molecule excitation occurs through photo-assisted collisions (discussed in section 5.5).

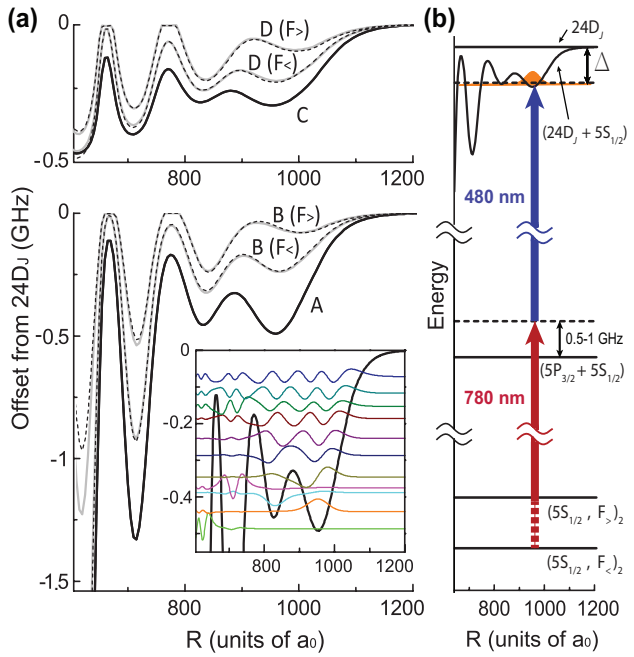

Figure 5.1: (a) Potential energy curves for Rb ($24D_J + 5S_{1/2}$) molecules for J=5/2 (top) and J=3/2 (bottom). The "deep" potentials (solid black) are virtually the same for both hyperfine ground-states ($F_>$ and $F_<$) and isotopes (^{87}Rb and ^{85}Rb). The "shallow" potentials (solid gray for ^{87}Rb, and dashed black for ^{85}Rb) depend significantly on hyperfine ground-state and slightly on isotope. Inset shows wavefunctions of vibrational resonances in potential A (vertical offset shows resonance energy). (b) Excitation level diagram. The figure is from my paper [50].

5.2 Theory

A theoretical framework is presented here in order to give a qualitative understanding of the origin and nature of the molecular resonances that are measured. The concepts will be revisited again in section 5.4, where they are used together with the experimental data to extract electron-atom scattering length functions.

5.2.1 Fermi pseudopotential model

The Rydberg-ground molecular interaction may be described by a Fermi pseudopotential [77, 78] in which the ground-state atom is modeled as a point perturber. The perturbation strength is determined by energy-dependent scattering lengths $a_l(k)$, which are related to the scattering phase shifts $\eta_l(k)$ by $a_l(k)^{2l+1} =$

$-\tan\eta_l(k)/k^{2l+1}$, where k is the electron momentum and l is the scattering partial-wave order (s, p, ...). We note that with this definition of the scattering, $a_l(k)$ always has the units of length regardless of l, which is why we sometimes refer to $a_p(k)$ as a scattering length. The p-wave scattering volume is just $a_p(k)^3$. In the reference frame of the Rydberg ionic core, the scattering interaction is [78]:

$$\begin{aligned}\hat{V}(\mathbf{r};R) = {} & 2\pi a_s(k)\delta^3(\mathbf{r}-R\hat{\mathbf{z}}) \\ & + 6\pi[a_p(k)]^3\delta^3(\mathbf{r}-R\hat{\mathbf{z}})\overleftarrow{\nabla}\cdot\overrightarrow{\nabla}\end{aligned} \tag{5.1}$$

where $\mathbf{r}$ and $R\hat{\mathbf{z}}$ are the positions of the Rydberg electron and perturber atom.

The full Hamiltonian for the system is [79]:

$$\hat{H}(\mathbf{r},R) = \quad \hat{H}_0 + \sum_{i=S,T}\hat{V}_i(\mathbf{r},R)\hat{\mathcal{P}}_i + A_{\mathrm{HFS}}\,\hat{\mathbf{S}}_2\cdot\hat{\mathbf{I}}_2 \tag{5.2}$$

where $\hat{H}_0$ is the Hamiltonian of the unperturbed Rydberg electron (including its fine structure). The second term sums over both spin-dependent singlet (i=S) and triplet (i=T) scattering channels, using the projection operators $\hat{\mathcal{P}}_T = \hat{\mathbf{S}}_1\cdot\hat{\mathbf{S}}_2 + 3/4$, $\hat{\mathcal{P}}_S = 1-\hat{\mathcal{P}}_T$ ($\hat{\mathbf{S}}_1$ and $\hat{\mathbf{S}}_2$ are the electronic spins of the Rydberg and ground-state atom, respectively). The last term represents the hyperfine coupling of $\hat{\mathbf{S}}_2$ to the ground-state-atom nuclear spin $\hat{\mathbf{I}}_2$, with hyperfine parameter A_{HFS}. In Rb, A_{HFS} is comparable to the scattering interactions (on the order of GHz), and $\hat{\mathbf{I}}_2$ becomes coupled in second order to $\hat{\mathbf{S}}_1$ through $\hat{\mathcal{P}}_T$ and $\hat{\mathcal{P}}_S$. The singlet potentials disappear and are replaced with mixed singlet-triplet potentials [58, 79]. These, in addition to the (nearly-pure) triplet potentials, sustain molecular bound states, as has been observed in Cs [56], Rb [59, 63], and Sr [80].

5.2.2 Adiabatic potential energy curves

We obtain the potential energy curves (PECs) by solving the Hamiltonian on a grid of intermolecular distances R, [28, 29], as shown in Fig. 5.1(a). Following the Born-Oppenheimer approximation, the PECs describe the vibrational motion. The hyperfine-mixed singlet-triplet potentials ("shallow" potentials) have shallower wells and vary significantly depending on whether the ground-state-atom is in its upper or lower hyperfine state, $F_2 = F_>$ or $F_<$. The shallow potentials for $F_<$ are deeper than those for $F_>$. The triplet potentials ("deep" potentials) are virtually unaffected by hyperfine mixing, and therefore independent of I_2 and F_2.

5.2.3 Molecular resonances

The narrow molecular resonances in each PEC are found by solving the Schrödinger equation for the vibrational motion [79], as explained further in subsection 5.4.2. The result is a spectrum of quasibound vibrational states, the majority of which are mostly contained in the outermost potential wells [inset of Fig. 5.1(a)].

5.3 Experiment

5.3.1 Procedure

The Rydberg molecules are photoassociated from cold Rb atoms. The atoms are first prepared in the one-dimensional lattice loaded from the MOT in the setup described previously. While the setup is an atypical one to create Rydberg molecules, it has several advantages. It facilitates either isotope to be cooled and trapped in either hyperfine ground state, which makes possible a direct comparison of each case. The setup also allows a high repetition rate (100 Hz), which is conducive to obtaining good signal-to-noise in spectroscopic experiments.

Pairs of atoms are excited through a two-photon transition to a $(24D_J+5S_{1/2})$ pair

state as shown in Fig. 5.1(b). The lower-transition laser (780 nm) frequency is 0.5-1 GHz blue-detuned from the $5P_{3/2}$ intermediate state to mitigate scattering-induced heating, while the upper transition laser (480 nm) frequency is scanned from the Rydberg atomic line to several hundred MHz below. Rydberg molecules are produced when the detuning from the Rydberg atomic line matches a molecular binding energy.

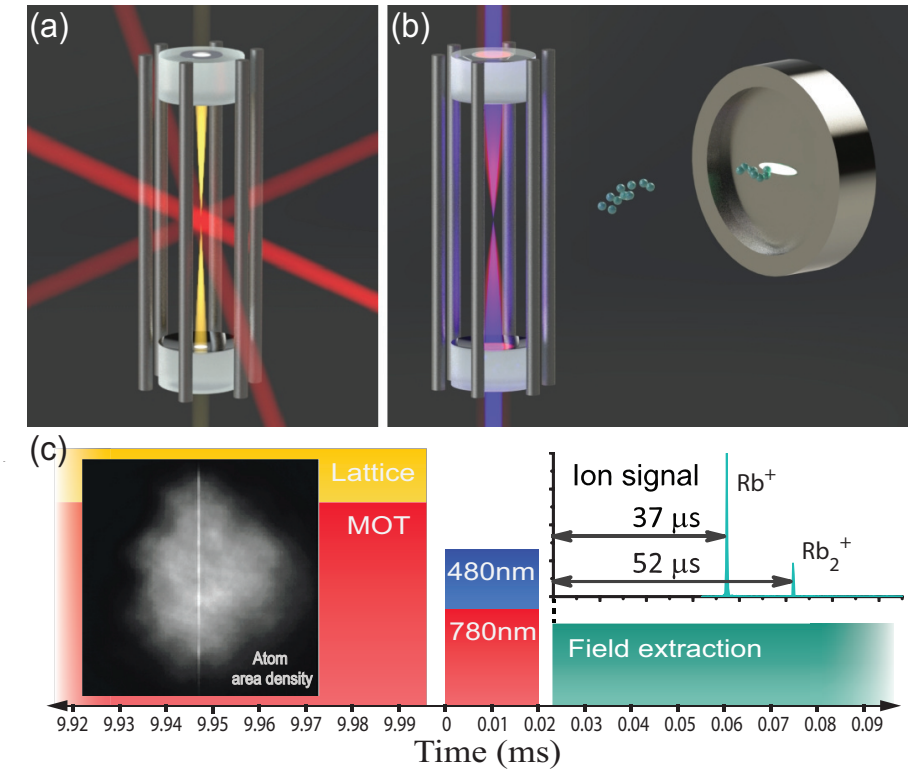

Figure 5.2: Experimental sequence: (a) Atoms are first trapped in a MOT (red beams) and loaded into the vertical 1-D lattice trap (yellow). (b) The traps are switched off, and overlapping 780-nm and 480-nm beams excite a Rydberg atomic or molecular state. After excitation, voltages applied to six metal rods steer spontaneously generated Rb^+ and Rb_2^+ ions to the MCP detector, where they arrive in time-resolved clusters. (c) Timing sequence. Data rate is 100 Hz. The insets show a qualitatively-representative atom area density of the lattice-trapped atoms and surrounding MOT (left) and an ion time-of-flight signal (upper right). The figure is from my paper [50].

Figure 5.2 shows the experimental geometry and timing. The lattice trap loads $\sim 2\times10^4$ atoms from an overlapping MOT (Fig. 5.2(a)) with a trap depth of $\sim$40 MHz for Rb $5S_{1/2}$. It generates an atom cloud of about 18 μm diameter, 700 μm length, transverse temperature $\sim$180 μK, and central volume density $\sim 1.6\times10^{11}$ cm^{-3}. While the longitudinal temperature could not be directly measured, we believe that it should

be approximately the same. The measured temperature is considerably higher than the temperature in other photoassociation experiments of Rydberg molecules, which are usually done from Bose-Einstein Condensate (BEC) or near-BEC clouds. I explain in section 5.5 how this scenario differs conceptually from the "frozen gas" picture commonly applied to related experiments, and how photoassociated molecules are still produced despite the relatively high atom temperatures. Before photoassociation, the MOT and the lattice trap are turned off to avoid light shifts. Several μs afterward, a 20-μs pulse of 780-nm and 480-nm light excites atoms to Rydberg atomic and molecular states. The 780-nm and 480-nm beams have respective waists of 20 μm and $\lesssim$ 100 μm and overlap with the 1064-nm trap, creating an oblong excitation volume in the densest region of the cloud.

The molecules are probed for eight cases of spin combinations: ground-state atom nuclear spin, I_2; the hyperfine state of the ground-state atom, F_2; and the fine state of the Rydberg atom J. To observe the isotope (I_2) dependence, we adjust our MOT lasers to trap either isotope. To observe the hyperfine (F_2) dependence, the ground-state atoms are prepared in either the upper ($F_>$) or lower ($F_<$) hyperfine state by turning off the repumper laser either at the same time as the cooling laser or 150 μs earlier. The 780-nm laser frequency is adjusted according to the choice of I_2 and F_2. Finally, to observe $24D$ $J = 3/2$ or $5/2$ Rydberg-ground molecules, the 480-nm laser frequency is changed by the Rydberg fine-structure splitting (913 MHz).

The Rydberg-ground molecules yield either Rb_2^+ via Hornbeck-Molnar autoionization or ion-pair formation, or Rb^+ via black-body photoionization or ion-pair formation [44, 81–83]. The ions detected by the microchannel plate [MCP; see Fig. 5.2(b)] constititute the signal. Rydberg-Rydberg molecules are also produced [84–86], but only a small fraction ionize spontaneously. Since the ion extraction electric field here is too weak to field-ionize either type of Rydberg molecule, Rydberg-ground molecules are preferentially detected.

5.3.2 Spectroscopic data of molecular binding energies

The ion counts produced from scanning the upper-transition laser, shown in Fig. 5.3, reveal the molecular state resonances. In Appendix A, I show a different dataset recorded for the same spectra, whose better signal-to-noise ratio more clearly exhibits the weaker resonances. I do not record or fit the resonance energies from the data, however, because the calibration of the x-axis values has lower accuracy than what is presented in this figure. The data is used later for the linewidth analysis in subsection 5.5.6.

The resonances in Fig. 5.3 are different for each (I_2, F_2, J) combination. The upward trend of the background signal at small detunings is attributed to Rydberg-Rydberg molecules [84]. I assign the most prominent peaks to the deep or shallow potentials of Rydberg-ground molecules, A/C or B/D in Fig. 5.1, respectively, by comparison with the resonances predicted by the model, described in the following section. The binding energies, determined by Gaussian fits to the peaks, are marked with vertical lines and listed in Table 5.1.

The identified peaks, with the exception of peaks D_x, arise from the first or second vibrational resonances in the outer region of the PECs ($R \approx 800$–$1000a_0$, see Fig. 5.1). We observed no other prominent resonances up to 150 MHz below the deepest peaks in Fig. 5.3. The D_x peaks correspond to resonances in the inner well at $R \approx 710a_0$; they have weaker signals due to the reduced likelihood of finding atoms at smaller internuclear separations. Most unidentified peaks in Fig. 5.3 are higher resonances in the deep potentials. They can be identified more clearly in the data in Appendix A, which has cleaner spectra but with lower accuracy in the detuning frequencies. The peaks' low signal strength may be attributed to the rapid oscillations in their vibrational wavefunctions [see the inset of Fig. 5.1(a)], leading to small Franck-Condon factors, and their short tunneling-induced lifetimes. The spin-mixing also plays a role in signal strength; a method for computing line strengths of vibrational spectra

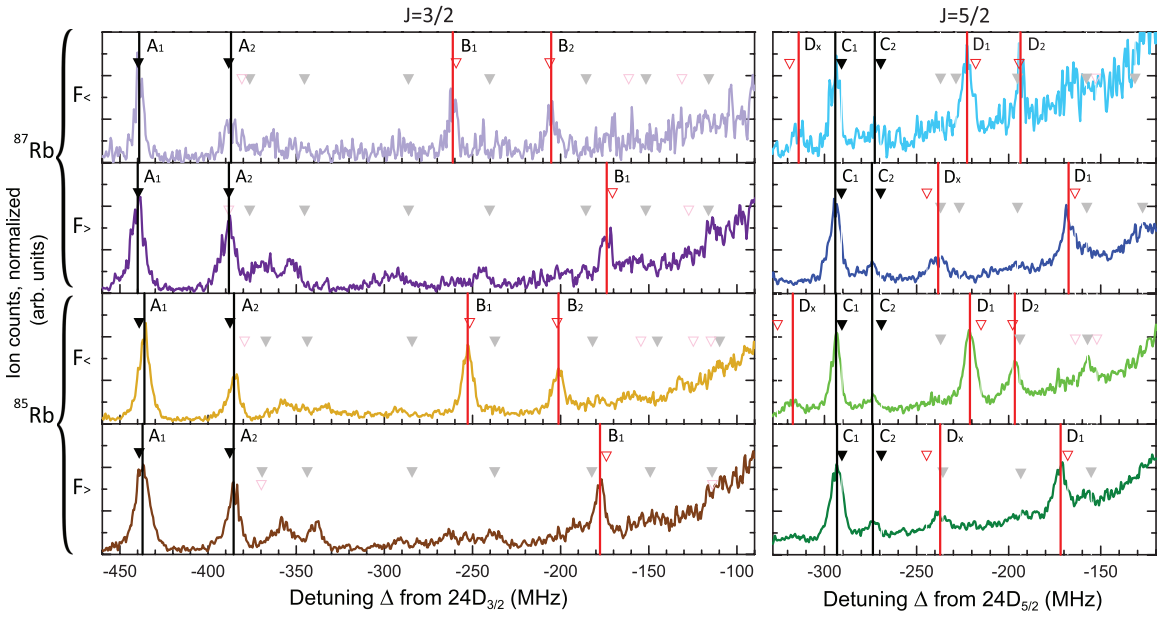

Figure 5.3: Detected ions vs. detuning relative to the $24D_J$ atomic state, for the eight (I_2, F_2, J)-combinations. The spectra are normalized by the height of the A_1 or C_1 resonance. A selection of resonances is marked with vertical lines and labeled according to their corresponding potential in Fig. 5.1(a). Filled (open) triangles denote resonances in the deep (shallow) potentials predicted with our model. Faded triangles are additional predicted resonances not used in the fitting procedure. The figure is from my paper [50]. A different dataset recorded for the same spectra is shown in Appendix A.

Pair potentials	A_1	A_2	B_1	B_2	
^{87}Rb $(24D_{3/2} + 5S_{1/2}$ F$_<)$	-439.1(10)	-387.0(10)	-261.2(8)	-205.4(8)	
^{87}Rb $(24D_{3/2} + 5S_{1/2}$ F$_>)$	-439.9(10)	-388.2(10)	-173.9(7)		
^{85}Rb $(24D_{3/2} + 5S_{1/2}$ F$_<)$	-436.1(9)	-385.3(9)	-252.7(8)	-201.2(7)	
^{85}Rb $(24D_{3/2} + 5S_{1/2}$ F$_>)$	-437.2(9)	-385.5(9)	-177.7(7)		
Pair potentials	C_1	C_2	D_x	D_1	D_2
^{87}Rb $(24D_{5/2} + 5S_{1/2}$ F$_<)$	-294.1(8)	-272.7(8)	-314.0(8)	-222.6(7)	-193.6(7)
^{87}Rb $(24D_{5/2} + 5S_{1/2}$ F$_>)$	-294.1(8)	-274.2(7)	-238.3(7)	-167.5(7)	
^{85}Rb $(24D_{5/2} + 5S_{1/2}$ F$_<)$	-293.7(8)	-274.1(8)	-317.2(8)	-221.0(7)	-196.7(7)
^{85}Rb $(24D_{5/2} + 5S_{1/2}$ F$_>)$	-293.2(8)	-273.7(8)	-237.2(7)	-171.8(7)	

Table 5.1: Molecular binding energies in MHz, relative to the atomic lines, corresponding to the labeled peaks in Fig. 5.3.

of Rydberg molecules including the hyperfine- and spin-dependence is presented in Ref. [87].

The starkest difference among the spectra in Fig. 5.3 is between J=5/2 (right) and J=3/2 (left); the deepest resonances differ by up to 150 MHz. The depths of the molecular potential wells and the fine structure scale as n^{-6} [60] and n^{-3}, respectively. At low n, the molecular binding interaction strength exceeds the fine-structure splitting. When this happens, the molecules are classified as Hund's case (a) [88, 89]. In this limit, the molecular potentials that asymptotically connect to J=5/2 approach and repel from the adiabatic potentials that connect to the J=3/2 atomic level. As a result, in the Hund's case (a) regime, the J=3/2 adiabatic potentials become deeper than the fine-structure coupling, with their depths scaling as n^{-6}, whereas the J=5/2 potentials are limited in depth by the fine structure splitting; hence their depths scales as n^{-3}. Molecules in Rb $24D_J$ are far into the Hund's case (a) regime. The relevance of Hund's cases to Rydberg-ground molecules has been discussed in detail in Ref. [79].

The largest difference among the rows in Fig. 5.3 and Table 5.1 is between the states in the shallow potentials (i.e., the B and D peaks) for $F_<$ and $F_>$, which differ by up to 70 MHz. The strong dependence on F_2 is expected from the PECs in Fig. 5.1. The B and D peaks also exhibit isotopic differences up to ∼10 MHz, which originate from the different hyperfine-coupling strengths A_{HFS}, nuclear spins I_2, and masses.

The A peaks are similar for $F_>$ and $F_<$ but vary slightly between the two isotopes (see Fig. 5.3 and Table 5.1). As the A-PECs are virtually identical, the variation is likely due to the isotopic mass difference. The heavier isotope has deeper binding energies because of its smaller vibrational frequencies within the same potential. The two unlabeled resonances immediately to the right of A_2 (at -370 to -330 MHz) show a pronounced difference between isotopes, suggesting that they correspond to states of the inner PEC wells at $R \approx 710a_0$ in Fig. 5.1, where a mass difference has a greater

quantitative effect because of the larger spacings between vibrational states.

5.3.3 Uncertainty analysis

The largest uncertainty arises from the 480-nm laser frequency calibration (typically 0.6-0.9 MHz), followed by statistical uncertainties caused by fluctuations in signal strength and the peak-fitting. The resultant relative uncertainties of the listed binding energies range between 0.2%, for the lowest states found, and 0.4%. To our knowledge, these values are lower than previously reported ones.

5.3.4 Preliminary data on very deeply bound Rydberg-ground molecules

In this subsection, I report some additional experimental spectra that were not used for the extraction of scattering lengths but may offer additional physical insight or support future studies.

I observed several peaks in the ion signal about 1500 MHz below the $24D_{3/2}$ atomic line, shown in Fig. 5.4. They did not consistently appear in the spectra. This characteristic was also seen with the molecular signals previously found, because they are sensitive to fluctuations in the quality of the MOT and dipole trap. The peaks' inconsistent appearance suggests that they are less likely to be caused by systematic effects associated with the AOMs and the laser spectrum transmitted to the atoms. The previously observed molecules with binding energies around 440 MHz and smaller are noticeably absent, which may be due to poor trap qualities that were present initially or that developed in the middle of the laser scan.

The features in the rightmost region of the spectrum have causes that are well-understood but mundane. An alternate order of AOM-deflected excitation light leaks into the primary beam and results in a copy of the atomic line with diminished amplitude at 80±0.2 MHz below the true atomic line. (The copy is marked by an arrow in Fig. 5.4.) At some point during the laser scanning between the atomic line

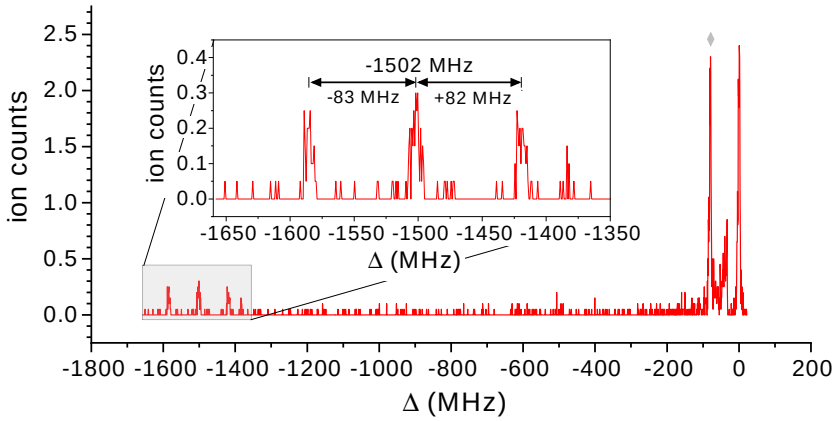

Figure 5.4: Ion counts as a function of laser detuning from the $24D_{3/2}$ atomic line (see text for more details).

copy and the true atomic line, I dramatically reduce the excitation light (in order to keep the ion counts low to protect the MCP detector), which manifests as a sharp drop-off in the spectrum and greatly diminishes the amplitude of the atomic line signal.

The three (or possibly four) peaks around 1500 MHz, assuming they are genuine signatures of the molecular resonances in the very deep inner potential wells, have several possible explanations. They may reflect the J-splitting of the p-wave scattering that is due to relativistic effects, as recently observed in Ref. [90]. Alternatively, they may originate from multiple inner potential wells that exist at different internuclear separations and/or that are from a combination of triplet and mixed singlet/triplet potentials. It is less likely that all of them are different vibrational resonances from the same inner potential well, because their frequency spacing is much closer than theoretical models predict.

Future work will be required to confirm the reproducibility of the peaks. In addition, studying the dependence of their resonance energies on principal quantum number may provide valuable insight into the underlying physics.

5.4 Extraction of scattering length functions from data

To model the observed molecular resonances based on Eqs. 5.1 and 5.2, four scattering-length functions $a_l^i(k)$ are required. In order to fit the functions from the data, a way to parameterize them is needed. To summarize our approach, for each scattering-length function, we use the short-range potential provided in Ref. [68], and integrate the radial Schrödinger equation using a single tuning parameter equivalent to a wavefunction phase shift near the atomic core. We evaluate the scattering wavefunctions at a specified distance from the ground-state atom perturber. The scattering lengths then follow from textbook equations [91]. The modeled resonances based on the scattering lengths are compared with the experimental data and the differences are used to adjust the aforementioned tuning parameters for the subsequent iteration of calculating the scattering length functions. The process is shown in a high-level outline in Fig. 5.5 and explained in the following.

5.4.1 Rydberg electron scattering and radial Schrödinger equation

The Rydberg electron is treated as a plane wave incident upon a perturbing potential that causes an outgoing spherical wave through elastic scattering. The difference in phase between the incoming wave and the outgoing wave at a distance far away from the interaction are referred to as a scattering phase shift, and it characterizes the interaction for each order of the scattering angular momentum ($l = 0, 1, \ldots$) and channel (singlet or triplet). Because the electron energies are very low and the internuclear distances are high, the $l \geq 2$ orders are neglected. The phase shift appears in the solution to the radial Schrödinger equation for the electronic wavefunction.

The radial component of the wavefunction may be expanded in terms of Legendre polynomials:

$$\Psi(\mathbf{r}) = \sum_{l=0}^{\infty} R_l(r) P_l(\cos\theta) \tag{5.3}$$

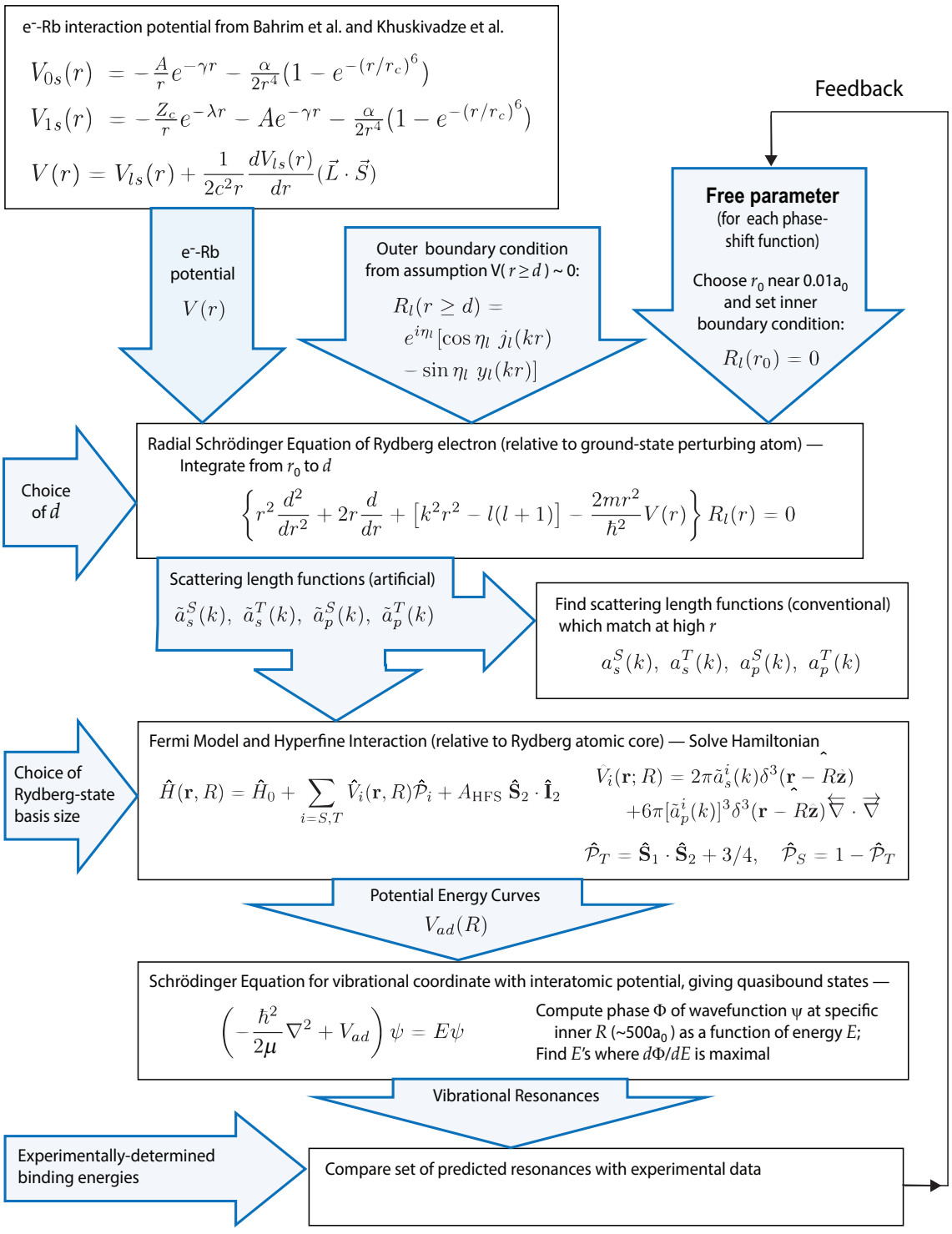

Figure 5.5: Outline of iterative fitting procedure to fit electron-atom scattering lengths using molecular resonance data. The feedback process is explained in section 5.4.3.

The radial part of the Schrödinger equation, relative to the ground-state perturbing atom, may be written as:

$$\left\{ r^2 \frac{d^2}{dr^2} + 2r\frac{d}{dr} + \left[k^2 r^2 - l(l+1)\right] - \frac{2mr^2}{\hbar^2} V(r) \right\} R_l(r) = 0 \tag{5.4}$$

5.4.1.1 Outer boundary condition and derivation of scattering phase shifts

At very far distances, the scattering potential $V(r)$ approaches zero. We choose an arbitrary evaluation distance from the perturbation d where we approximate that $V(r) \simeq 0$ when $r \geq d$. In this region, the most general solution to the Eq. 5.4 is then:

$$R_l(r \geq d) = e^{i\eta_l}[\cos\eta_l \; j_l(kr) - \sin\eta_l \; y_l(kr)] \tag{5.5}$$

where j_l and y_l are l-th order spherical Bessel functions of the first and second kind. To find the scattering phase shift η_l, we first take the logarithmic derivative of Eq. 5.5 evaluated at d and define it as β (see also Ref. [91, 92]):

$$\beta \equiv \frac{1}{R_l} \left.\frac{d}{dr} R_l(r)\right|_{r=d} = kd \left(\frac{\cos\eta_l \; j_l'(kd) - \sin\eta_l \; y_l'(kd)}{\cos\eta_l \; j_l(kd) - \sin\eta_l \; y_l(kd)} \right) \tag{5.6}$$

The above equation may be rearranged to solve for the phase shift $\eta_l(k)$:

$$\eta_l(k) = \tan^{-1}\left(\frac{kd \; j_l'(kd) - \beta \; j_l(kd)}{kd \; y_l'(kd) - \beta \; y_l(kd)} \right) \tag{5.7}$$

The scattering lengths are then related to the scattering phase shifts by

$$\tilde{a}_l(k)^{2l+1} = -\frac{\tan\eta_l(k)}{k^{2l+1}}. \tag{5.8}$$

The values of the resulting scattering length functions $\tilde{a}_l^i(k)$ at very low k are artificial because they depend on the evaluation distance d, whereas the true scattering length functions $a_l^i(k)$, obtained in the limit $d \to \infty$, are independent of d. Here,

we choose $d = 150a_0$, corresponding to the typical width of the outermost lobe of the Rydberg-electron wavefunction for $24D$. Our approach of using a finite value of d avoids the problem that for $k \to 0$ the p-wave scattering lengths diverge [93], which would cause an unphysical divergence in the adiabatic potentials at the classical turning point of the Rydberg electron when using the Fermi method. Due to the localization of the Rydberg electron within the lobes of its wavefunction, the probability of finding it at very low k is negligible, allowing us to use $\tilde{a}_l^i(k)$ to calculate the potentials.

The scattering lengths may be calculated numerically when $R_l(d)$ and $\frac{d}{dr}\ R_l(d)$ are known. To find these, we assume a potential for $V(r)$ in Eq. 5.4 and an inner boundary condition, which are discussed in the following, and then integrate Eq. 5.4.

5.4.1.2 Electron-atom interaction potential

We use a model developed by Bahrim et al. [94, 95] for the interaction potential for an electron with an alkali-metal atom in its ground-state. The interaction potential is

$$V(r) = V_{ls}(r) + \frac{1}{2c^2 r}\frac{dV_{ls}(r)}{dr}(\vec{L}\cdot\vec{S}), \tag{5.9}$$

where r is the electron-atom separation, l and s denote the angular momentum and spin of the two electrons relative to the ground-state atom, L and S are the angular momentum and spin of the Rydberg electron. The forms of V_{ls} are taken to be

$$V_{0s}(r) = -\frac{A}{r}e^{-\gamma r} - \frac{\alpha}{2r^4}(1 - e^{-(r/r_c)^6}) \tag{5.10}$$

$$\text{and } V_{1s}(r) = -\frac{Z_c}{r}e^{-\lambda r} - Ae^{-\gamma r} - \frac{\alpha}{2r^4}(1 - e^{-(r/r_c)^6}). \tag{5.11}$$

Here Z_c is the nuclear charge ($Z_c = 37$ for Rb), λ is the nuclear screening parameter, α if the ground-state-atom polarizability, and A, γ, and r_c come from the fit

that reproduces the low-energy scattering eigenphases for $J \leq 2$ from Dirac R-matrix calculations [52–54] and negative ion binding energies. We use the parameters for Rb given in Ref. [68] (except for an updated value of polarizability, $\alpha = 319.8$ a.u.), which are:

λ	state	A	γ	r_c
7.4975	^1S	4.5642	1.3438	1.8883
	^3S	68.576	9.9898	2.3813
	^1P	24.2625	1.0055	1.8869
	^3P	21.4523	4.8733	1.8160

Table 5.2: Parameters for the e^--Rb(5s) interaction potential.

5.4.1.3 Inner boundary condition with adjustable zero-crossing

We find $R_l(d)$ and $\frac{d}{dr}R_l(d)$, needed to evaluate Eq. 5.6, by first choosing a location near $r = 0.01a_0$ (near the center of the perturber atom) where $R_l(r)$ is set to zero. Then we integrate the radial Schrödinger equation (Eq. 5.4) outward using the interaction potentials defined in Eq. 5.9-5.11. The zero-crossing in the inner region is the parameter we fine-tune for each of the scattering length functions $\tilde{a}_l^i(k)$ to fit the modeled molecular resonances to our data. Adjusting these parameters is equivalent to adjusting the wavefunction phases at a fixed position near $0.01a_0$, and it essentially provides short-range corrections to the Rb^- scattering potentials.

5.4.2 Vibrational resonances from scattering lengths

Once the scattering length functions are defined, the Hamiltonian of Eq. 5.2 is solved to find the adiabatic PECs of the system as a function of internuclear distance. The PECs exhibit several potential wells near the outer edge of the Rydberg electronic wavefunction that are capable of supporting quasibound vibrational states. The states are only quasibound, as opposed to truly time-independent, because the PECs have a steep decline on the inner side of the potential wells, into which the vibrational

resonances slowly "leak" to form Rb_2 molecules of the conventional type. The energies of the resonances are found by solving the Schrödinger equation for a series of energies and examining the phase of the vibrational wavefunction at a fixed point in the inner region (that is chosen to be several hundred a_0 from the core). The phase as a function of energy exhibits increases of π with slopes of varying steepness. The resonance energies are centered where the phase change has local maxima, and for each resonance the energy range over which the phase changes by π is the energy width ΔE. The resonance line shapes follow the Breit-Wigner formula [91], where the resonance lifetime is proportional to the inverse of ΔE, i.e. $\tau = h/(4\Delta E)$.

The vibrational resonances and their corresponding adiabatic potentials are shown in Fig. 5.6. The resonances used for the fitting were chosen based on how well they meet two criteria, namely that their respective peaks in the recorded ion signal are sufficiently high to be observed clearly, and secondly, that the resonance to which each data peak belonged can be assigned with a high degree of certainty, even while the scattering length parameters used in the calculations are adjusted. Such criteria favor resonances whose wavefunction is approximately a symmetrical, single lobe in the first or second outermost potential well (that is, what would be the vibrational ground-state of the well if the wavefunction were completely confined to that well alone). These resonances tend to have the highest photoassociation rate and thus more distinguished spectral peaks. The wavefunctions of higher-order resonances, which have antisymmetry and/or more oscillations, are less likely to have good overlap with the lower-state wavefunction (i.e. the Franck-Condon factors are generally worse) and thus such resonances have lower photoassociation rates. The ion peaks from resonances in the inner potential wells are likewise smaller in amplitude because they are often broadened from higher tunneling-induced decay rates, and because there is comparatively less time during the excitation pulse when two atoms have the appropriate (smaller) separation distance. These postulated trends are corroborated

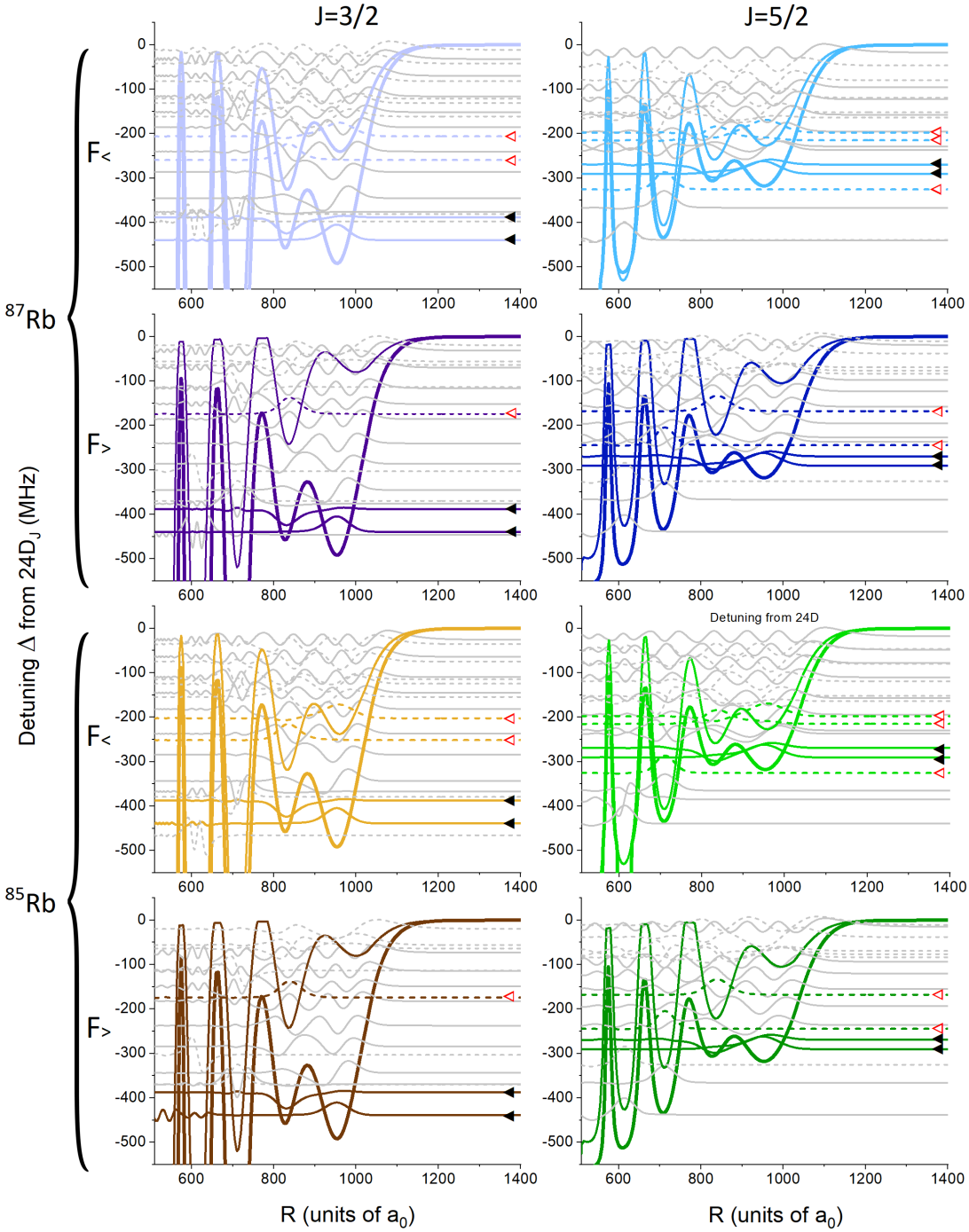

Figure 5.6: Vibrational wavefunctions for triplet (solid) and mixed singlet-triplet (dashed) molecular resonances and their adiabatic PECs for the 8 cases in Fig. 5.3. The wavefunctions have arbitrary vertical scaling and are vertically offset by their respective resonance energies. The wavefunctions for the resonances selected for fitting are emphasized by being colored and marked with black or open red triangles to facilitate comparison with Fig. 5.3. The other vibrational wavefunctions are shown in gray.

when comparing the shapes of the simulated wavefunctions in Fig. 5.6 with their corresponding peaks in the data presented in Fig. 5.3. Higher-order and inner-well resonances do not meet the second criterion well either because they are more sensitive to the exact shape of the potentials, which makes it more difficult to conclusively match the observed peaks with the simulated ones. Furthermore, the relative dependence of these resonances is overly weighted on the four single tuning parameters that we adjust, instead of other details such as the additional parameters that would be needed to more precisely characterize the scattering length functions over an energy range. Thus, even though in Fig. 5.3 there are many observable peaks in addition to the labeled ones, and most even have probable correspondence with the simulated resonances (see depressed, light-shaded triangles in Fig. 5.3), we do not find them to be very useful for our modeling approach here.

5.4.3 Fitting procedure

In our fitting procedure, we begin with the inner-region zero-crossings that yield scattering length functions matching those given in Ref. [68]. Every set of four $\tilde{a}_l^i(k)$ yields eight PECs through solving Eq. 5.2. From the PECs we obtain the vibrational resonances and determine their rms deviation from the 32 measured values in Table 5.1. The four adjustable zero-crossings are varied and the procedure is repeated until the rms deviation is minimized.

The process of fitting the modeled resonances to the data by adjusting the zero-crossings can be somewhat time-consuming and laborious. To reduce the number of iterations by making better-informed guesses, we invoked the following method. We make a crude assumption of linear dependence of each resonance on the zero-energy values of each scattering function, i.e.

$$b = \sum_j A_j x_j \qquad \text{for } j = \tilde{a}_s^T,\ \tilde{a}_s^S,\ \tilde{a}_p^T,\ \tilde{a}_p^S\ , \tag{5.12}$$

where b is the frequency shift in a particular resonance due to shifts in zero-energy values of each of the four scattering length functions (x_j), and each A_j is a constant to be determined. For a set of n resonances, we extend Eq. 5.12 to the matrix form

$$\mathbf{A}\mathbf{x} = \mathbf{b}, \tag{5.13}$$

or explicitly,

$$\begin{bmatrix} A_{1\alpha} & A_{1\beta} & A_{1\gamma} & A_{1\delta} \\ A_{2\alpha} & A_{2\beta} & A_{2\gamma} & A_{2\delta} \\ \vdots & \vdots & \vdots & \vdots \\ A_{n\alpha} & A_{n\beta} & A_{n\gamma} & A_{n\delta} \end{bmatrix} \begin{bmatrix} x_\alpha & \dots \\ x_\beta & \dots \\ x_\gamma & \dots \\ x_\delta & \dots \end{bmatrix} = \begin{bmatrix} b_1 & \dots \\ b_2 & \dots \\ \vdots & \vdots \\ b_n & \dots \end{bmatrix}, \tag{5.14}$$

where the Greek subscripts indicate the four types of scattering functions. We run the simulations (i.e. find the molecular resonances) for an initial set of zero-energy scattering values as a reference and for four test cases, labeled *a*-*d*, in which the zero-energy value offset vectors are varied in independent ways. By using the arbitrary input chosen for the four cases $\{\mathbf{x}_a, \mathbf{x}_b, \mathbf{x}_c, \mathbf{x}_d\}$ as $\mathbf{x}$ and the output $\{\mathbf{b}_a, \mathbf{b}_b, \mathbf{b}_c, \mathbf{b}_d\}$ as $\mathbf{b}$, we may compute $\mathbf{A}$ via the relation $\mathbf{A} = \mathbf{b}\mathbf{x}^{-\mathbf{1}}$. Ideally, we would like to find the vector solution for Eq. 5.13 when $\mathbf{b}$ is the experimental dataset vector, which I denote by $\hat{\mathbf{b}}$. However, a unique solution does not necessarily exist, and is unlikely when $\mathbf{A}$ is not invertible. In our particular situation, where we use $n = 32$ resonances in $\hat{\mathbf{b}}$, it is not possible for $\mathbf{A}$ to be invertible because it is not square. Instead, as long as $\mathbf{A}$ is full column rank, we may use its Moore-Penrose pseudoinverse to find the solution $\hat{\mathbf{x}}$ where $\mathbf{A}\hat{\mathbf{x}}$ has the least squares error from $\hat{\mathbf{b}}$. The solution is

$$\hat{\mathbf{x}} = (\mathbf{A}^{\mathrm{T}}\mathbf{A})^{-1}\mathbf{A}^{\mathrm{T}}\hat{\mathbf{b}}. \tag{5.15}$$

Because the assumption of linearity (Eq. 5.13) is only an approximation, $\hat{\mathbf{x}}$ does not

necessarily provide the optimal zero-energy scattering length offsets from the initial case, but it is a good guess. We iterate the procedure with the new initial reference case as the former one shifted by $\hat{\mathbf{x}}$, and we gradually decrease the step sizes in $\{\mathbf{x}_a, \mathbf{x}_b, \mathbf{x}_c, \mathbf{x}_d\}$ as $\hat{\mathbf{x}}$ becomes vanishingly small.

Besides increasing efficiency, an additional benefit of this approach is that the calculated $\mathbf{A}$ explicitly offers insight on the dependencies of each resonances on the four scattering length functions. For example, the $\mathbf{A}$ matrix elements for the dependence of the A and C resonances (refer to Fig. 5.3) are found to be nonzero only for the two triplet scattering-length functions, whereas the B and D resonances have nonzero elements for all four scattering-length functions. The way the dependency strengths vary among the set of 32 resonances is what leads $\mathbf{A}$ to be full column rank and makes possible the simultaneous fitting of the four scattering length functions.

5.4.4 Scattering length results

The rms deviation of the resonances is found to be minimized at 3.8 MHz. The corresponding calculated resonances are shown as triangles in Fig. 5.3.

To estimate the zero-energy values of the true scattering length functions, we also calculate the functions $a_s^i(k)$ using an evaluation distance $d = 2 \times 10^4 a_0$. Figure 5.7 shows the four extracted scattering length functions $\tilde{a}_l^i(k)$ and their corresponding $a_l^i(k)$. As expected, $\tilde{a}_l^i(k)$ and $a_l^i(k)$ match at $k \gtrsim 0.015$ ($E = \hbar^2 k^2 / 2m \gtrsim 3$ meV). We anticipate the predicted scattering lengths to be the most useful in the range $k = 0.012 - 0.030$ (shaded vertical strip in Fig. 5.7), which corresponds to $E = 2 - 12$ meV and $R = 700 - 960 a_0$, because this is the region probed by the measured molecular bound states.

We quantify the uncertainty in $\tilde{a}_l^i(k)$ and $a_l^i(k)$ by varying several parameters in our procedure. First, we perform the fitting procedure for three Rydberg-state basis sets $21.1 - j \leq n^* \leq 24.1 + j$, with effective principal quantum number n^*, for $j =$

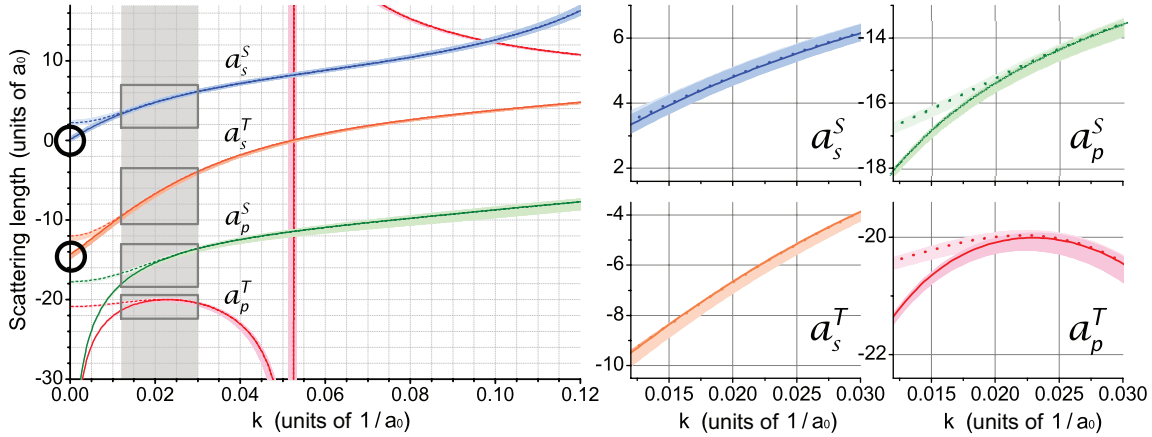

Figure 5.7: Scattering length functions for the $a_l^i(k)$ (solid lines; $d = 2 \times 10^4 a_0$) and $\tilde{a}_l^i(k)$ (dashed lines; $d = 150 a_0$) that correspond to the predicted resonances in Fig. 5.3. Shaded backdrops behind the curves show the uncertainties. Vertical gray strip corresponds to the experimentally relevant energy range; the four inscribed rectangles correspond to the zoom-ins shown in the four panels on the right. Black circles indicate the two zero-energy values included in Table 5.3 for this work. The figure is from my paper [50].

	$a_s^T(0)$	$a_s^S(0)$	Ref.
Theory	-16.1	0.627	[53]
	-16.9	0.63	[96]
Experiment	-15.7(1)	neglected	[60]
	-15.7(1)*	-0.2(5)	[59]
	-14.0(5)	neglected	[58]
	-15.2(5)	neglected	[90]
	-14.7(3)	0.0(3)	This work

Table 5.3: Zero-energy scattering lengths in a_0. $^*a_s^T(0)$ was fixed while $a_s^S(0)$ was fitted.

0, 1 and 2. In Fig. 5.3, the $j = 2$ basis size is used. Secondly, we include or omit resonances in the inner potential well at $R = 710 a_0$ (see Fig. 5.1). Thirdly, we increase or decrease the measured resonance values by the experimental frequency uncertainty ($\sim 0.2\%$). We use the combination of the three sources as the estimated uncertainty (in Fig. 5.7 and Table 5.3).

We are able to simultaneously fit the four scattering lengths because we analyze a large set of binding energies on PECs for a variety of spin cases, which have different sensitivities to the singlet and triplet s-wave and p-wave scattering-length functions.

For instance, the inner-well resonances at $710a_0$ (e.g., D_x) and $820a_0$ (e.g., A_2, B_1, C_2, D_1) depend strongly on $\tilde{a}_p^T(k)$ (whose shape resonance is responsible for the steep drop-off in Fig. 5.1(a) at $600a_0$) and weakly on $\tilde{a}_s^T(k)$, while outer-well resonances show the opposite trend. Meanwhile, substantial dependencies on $\tilde{a}_s^S(k)$ and $\tilde{a}_p^S(k)$ are only found in the B and D resonances. Some small codependencies of the scattering lengths remain. For instance, fixing $\tilde{a}_s^S(k)$ would significantly decrease the uncertainty in $\tilde{a}_p^S(k)$.

We are quoting an experimental result for $a_p^S(k)$ [and for $a_l^i(k)$ for $E = 2-12$ meV] derived from a fitting procedure applied in a Rydberg-ground molecule experiment. In Table 5.3, we show our median values (within the uncertainty bounds) of $a_s^T(0)$ and $a_s^S(0)$ for comparison with other published zero-energy values.

5.4.5 Relation to other work

Previous measurements of vibrational energies of low-angular-momentum diatomic Rydberg-ground molecules have spanned principal quantum numbers n = 26-45, angular momentum S, P, and D states, and atomic species rubidium, cesium, and strontium [29, 55–60, 80]. For Sr, the s-wave and p-wave zero-energy scattering lengths, $a_s(0)$ and $a_p(0)$, were extracted from S-state data [55]. In Rb and Cs electron-scattering, there are two relevant electrons. For Cs, the corresponding singlet and triplet s-wave scattering lengths, $a_s^S(0)$ and $a_s^T(0)$, were extracted from mixed singlet-triplet resonances in P-states [56] using a model developed in Ref. [79]. In Rb, $a_s^T(0)$ was extracted from S- and D-state molecular resonances [29, 57, 58] and $a_p^T(0)$ from S-state resonances [57]. Mixed singlet-triplet resonances in Rb S-states [59] allowed an extraction of $a_s^S(0)$ after determining $a_s^T(0)$ from previous data [29, 60]. Subsequent to this work, $a_s^S(0)$ and the p-wave shape resonance energy were extracted for Rb in S-states [90]. To our knowledge, $a_p^S(k)$ at any k has not been measured.

5.4.6 Discussion

We note several deficiencies of the method we have used for extracting electron-atom scattering lengths. First, the choice of basis size used to calculate the adiabatic potentials affects the depth of the potentials. We explored the convergence behavior of the adiabatic potentials as a function of basis size, ranging from $21.1 \leq n^* \leq 24.1$ to $17.1 \leq n^* \leq 28.1$ (i.e. we varied the range in n^* from about 3 to 11). Over this substantial variation in n^* range, we found that the outer potential wells increased in depth by 13% over the entire range, and that they do not seem to converge with growing basis size (but the incremental changes decrease). This is problematic and raises the question of which basis choice leads to the most accurate potentials. The issue of non-convergence has also been noted elsewhere and discussed in comparison to alternative techniques for calculating the adiabatic potentials [75, 97–99], and the topic has been described as controversial. A second deficiency of our method is that the Fermi model may have fundamental inaccuracies at low n, where the size of the perturber atom relative to the Rydberg wavefunction increases. This could possibly be addressed by using a Green's function calculation [68]; however, in a recent subsequent work where a Green's-function-based approach was used [90], a similar value for $a_s^T(0)$ was found with no improvement in uncertainty.

The minor discrepancies between our quoted zero-energy scattering lengths and previous results have several possible causes. Methods for calculating the k-dependence of $a_l^i(k)$ vary. The inaccuracy of the Fermi model at low n may contribute. We also note that the previously-quoted experimental scattering lengths did not account for p-wave scattering, which may have caused the extracted s-wave values to be overly negative. Finally, we note that in Ref. [57] two values for $a_s^T(0)$ are presented, -16.05a_0 and -19.48a_0, along with a zero-energy p-wave scattering length $a_p^T(0)$ of -21.15a_0.

5.5 Photoassociation in the 180μK regime

Previously it has been suggested that, to observe photoassociation of low-ℓ Rydberg molecules, low temperatures are necessary in order to avoid collisions during excitation [29]. Prior experimental efforts have used atomic samples of only several tens of μK at most. Here, the reported results are obtained with atoms prepared at a temperature of $\sim$180 μK, densities of only $\gtrsim 10^{11}$ cm^{-3}, and a quantum state as low as $n = 24$. The ability to photoassociate Rydberg-ground-state molecules whose constituent atoms are prepared using only a standard MOT and a single-axis dipole trap (without using a BEC, magnetic trap or a compressed MOT) greatly simplifies the experimental requirements, making their observation accessible with a wider variety of experimental setups.

The strongest molecular signal we observe is about 1% of the signal on the atomic line (not shown in Fig. 5.3). This is surprising because under the given conditions the instantaneous probability of finding a second ground-state atom within a Rydberg-atom radius of an atom is only about 0.01%. This discrepancy may be resolved by interpreting the molecule excitations as photo-assisted collisions. The estimates we make in the following subsections show that the excitation pulse duration, Rydberg-excitation Rabi frequency, thermal velocities and atom density are such that during the excitation pulses the fraction of atom pairs that undergo collisions at distances of the typical vibrational bond length ($\sim$1000a_0) is sufficient to explain the molecular-signal strength. In a photo-assisted collision, in contrast to the concept of a frozen Rydberg gas, the molecule excitation can be considered a non-adiabatic transition of atomic wave-packets between intersecting dressed-atom ground-ground and ground-Rydberg PEC's that are coupled by the Rydberg Rabi frequency. Our analysis not only explains how photoassociation is not prohibited by the thermal motion, but also suggests that the higher temperature actually enhances the photoassociation rate when the atomic density is low, and the optical Rabi frequency is sufficiently high.

5.5.1 Photo-assisted collision picture of molecular excitation

In the following, we describe a simple kinematic model of photoassociation in a warm atomic vapor. The fraction of atoms excited to molecules in a single experimental cycle ($2N_m/N_a$) is equal to the rate per atom of photoassociation "attempts" R (i.e. instances when the atom is within the appropriate separation distance of a second atom r_m), times the excitation pulse length T_p, times the efficiency η (or success rate) of photoassociation when the atoms are at the right separation, i.e.,

$$\frac{2N_m}{N_a} = R\,T_p\,\eta. \tag{5.16}$$

The rate per atom at which photoassociation attempts are made is

$$R = \sqrt{2}\,n_{\mathrm{v}}\,\pi\,r_m^2 v, \tag{5.17}$$

where n_{v} is the volume density, πr_m^2 is the cross-section of the Rydberg molecular state with internuclear separation r_m, and v is the thermal velocity (mean magnitude of the velocity). Therefore, the molecular photoassociation probability is

$$\frac{2N_m}{N_a} = \sqrt{2}\,n_{\mathrm{v}}\,\pi\,r_m^2 v\,T_p\,\eta. \tag{5.18}$$

The subsequent subsections are dedicated to evaluating various parameters in Eq. 5.18 in order to estimate N_m, with a particular emphasis on how the atom temperature may influence the parameters directly or limit the validity of the equation.

5.5.2 Role of temperature in photoassociation rate

First, we consider the efficiency η. We regard the excitation to a molecular state as a fraction of an incomplete Rabi oscillation, and write the efficiency as

$$\eta = \eta_0 \ \sin^2\left(\frac{\Omega_{\text{eff}}\ t}{2}\right), \tag{5.19}$$

where η_0 accounts for the imperfect Franck-Condon overlap of the ground atomic and excited molecular states, Ω_{eff} is the effective Rabi frequency of the optical excitation, and t is the time during which an atom pair experiences the excitation light *and* has a separation distance of about r_m. The t is the time it takes for an atom to traverse the span of the outer well Δ_w (assuming that this time is short in comparison to the excitation pulse time), and its value is about $\Delta_w/(\sqrt{2}v)$. If the optical intensities of the excitation beams are not a limitation, the efficiency may be maximized by setting the intensities such that $\Omega_{\text{eff}}/(2\pi) \approx 1/(2t) \approx v/(\sqrt{2}\Delta_w)$. The optimal value of Ω_{eff} then depends on temperature, but the maximal value of η does not, with the tentative assumption that η_0 is temperature-independent. In any case, the maximal value of η is η_0, or equivalently $\eta/\eta_0 \leq 1$. The value of η/η_0 in our experiment is discussed in subsection 5.5.4.

For a fixed atomic density and target molecular state and a maximized η, the only tunable parameters remaining in Eq. 5.18 are v and T_p. The maximum effective T_p is practically limited by the decay time of the molecular states (usually tens or hundreds of μs). The remaining v is proportional to the square root of the temperature. Thus, if the optical excitation intensities are not a practical limitation, then increasing the temperature actually improves the molecular photoassociation rate until $v \sim (\sqrt{2}n_{\text{V}}\pi r_m^2 \text{T}_p)^{-1}$.

Our experimental parameters are listed in Table 5.4. For our atomic density and $T_p = 20\mu$s, the temperature at which $v \sim (\sqrt{2}n_{\text{V}}\pi r_m^2 \text{T}_p)^{-1}$ is about 2 K, and

for BEC densities ($\sim 10^{14}$ cm^{-3}) it is about 7 μK. Of course, the atoms must also remain within the excitation volume during the pulse, which imposes a maximum temperature restraint of several mK or more, depending on the dimensions of the excitation volume.

Independent parameters	N_a	atom number	$\sim 2 \times 10^4$ atoms
	n_v	volume density	1.8×10^{11} cm^{-3}
	n^*	effective principal q. number	22.7
	T	atom temperature	180 μK
	T_p	excitation-pulse duration	20 μs
Derived or contingent parameters	r_m	internuclear separation ($\sim 2n^{*2}$)	$\sim 1000a_0$ (see Fig. 5.6)
	Δ_w	width of outer potential well	$150a_0$ (see Fig. 5.6)
	v	thermal velocity $[\sqrt{8k_BT/(\pi m)}]$	0.21 m/s
	t	atom traversal time ($\approx \Delta_w/v$)	38 ns
	R	rate of PA attempts ($\sqrt{2}n_v\pi r_m^2 v$)	470 Hz
	η	efficiency of PA attempts	≤ 1

Table 5.4: Experimental parameters and molecular characteristics for estimating photoassociation (PA) rates

5.5.3 Thermal effects on molecular bond stability

If the atom cloud temperature is very high, a typical atom pair is not able to sustain a Rydberg molecular bond because of the relative momentum between the two atoms. At the time of photoassociation, the kinetic energy corresponding to relative momentum is transferred to vibrational and rotational energies of the diatomic molecule. We note that the quantization of vibrational energies, as already demonstrated in Fig. 5.6, is on the order of 30 MHz and thus resolvable with our $\sim$ 1 MHz-linewidth excitation light. In contrast, the rotational energy quantization is on the order of $\hbar/(4\pi m r^2) \approx 20$ kHz.

For an atom pair to remain intact after photoassociation despite vibrational motion, the initial thermal energy of the atoms should be less than the binding energy E, i.e. $T < Eh/k_B \approx 20$mK for $E = 400$MHz. The maximum allowed rotational

energy for the centrifugal force to not pull the atoms apart corresponds to a temperature that is at least as high. The centrifugal force F_c should be less than the force corresponding to the maximum slope of the adiabatic potential on the outer edge, which is about the binding energy over a small fraction of the separation distance Δ_r, so $F_c < E/\Delta_r$. For two atoms of mass m with equal and opposite velocities perpendicular to their internuclear axis, and separated by a distance r, the centrifugal force is $F_c = 2mv^2/r$. Assuming $k_B T = mv^2/2$, then $F_c = 4k_B T/r$ and the temperature requirement is $T < (Eh/k_B) \cdot r/(4\Delta_r)$. The factor $r/(4\Delta_r)$ will in practice always be somewhat greater than one (in our case it is about 2.5), so the temperature limit is higher for the ability to contain rotational energy in the molecular bond. The atom temperature in our experiment is two orders of magnitude less than both temperature limits, so it should not prohibit photoassociation.

Although F_c and $F_{\max}$ are separated in scale in our experiment, both are extremely weak. For $(24D_J{+}5S_{1/2})$ Rydberg molecules and our atomic temperature of 180μK, F_c is about 2×10^{-19} N and $F_{\max}$ is about 5×10^{-17} N. For perspective, typical forces in a biological environment or to rupture weak conventional molecular bonds are on the order of 10^{-12} N.

5.5.4 Rabi frequencies

We estimate the optical Rabi frequency for the two-photon transition between the ground-state atom pair state to the molecular state in order to compare the timescales of excitation and atomic motion, and to roughly estimate η/η_0 from Eq. 5.19.

The Rabi frequency for a field of strength $\mathcal{E}$ and polarization $\hat{\varepsilon}$, resonantly driving the transition $|a\rangle \rightarrow |b\rangle$ is

$$\Omega = \frac{\vec{d}_{ab} \cdot \mathcal{E}\hat{\varepsilon}}{\hbar} = \frac{\mu_{ab}\, \mathcal{E}}{\hbar}, \tag{5.20}$$

where μ_{ab} is the scalar value of the effective transition dipole moment. Using

the intensity relations $I = c\varepsilon_0\mathcal{E}^2/2 = 2P/(\pi w^2)$ gives $\mathcal{E} = 2\sqrt{P/(\pi w^2 c\epsilon)}$. The Rabi frequency for a Gaussian beam of power P and waist w is then

$$\Omega = \frac{2\mu_{ab}}{\hbar}\sqrt{\frac{P}{\pi w^2 c\epsilon_0}}. \tag{5.21}$$

According to the Wigner-Eckhart theorem, the effective transition dipole moment may be separated into a factor characterizing the relevant $|m_j\rangle \rightarrow |m'_j\rangle$ transitions and light polarization, and the reduced dipole moment (which is independent of m_j, m'_j, and polarization). For the latter, we use the convention

$$\langle \alpha\ j||\mathbf{d}||\alpha'\ j'\rangle = \sum_{m'q}\langle \alpha\ j\ m|d_q|\alpha'\ j'\ m'\rangle\langle j\ m|j'\ m';1\ q\rangle. \tag{5.22}$$

For π-polarized and far-detuned light, the effective transition dipole moment includes all $|m_j\rangle \rightarrow |m'_j\rangle$ transitions and equals

$$\mu_{ab} = \frac{1}{\sqrt{3}}\langle \alpha\ j||\mathbf{d}||\alpha'\ j'\rangle. \tag{5.23}$$

The estimated powers and waists of the excitation beams, along with the effective transition dipole moments and calculated single-beam Rabi frequencies, are shown in Table 5.5.

Transition $\lvert a\rangle \rightarrow \lvert b\rangle$	Power (P)	Beam waist (w)	Effective dipole moment (μ_{ab})	Rabi frequency, single (Ω)
$\lvert 5S_{1/2}\rangle \rightarrow \lvert 5P_{3/2}\rangle$	$\sim 20\mu$W	$\sim 43\mu$m	$2.44ea_0$ [43]	$2\pi \times 71$ MHz
$\lvert 5P_{3/2}\rangle \rightarrow \lvert 24D_{5/2}\rangle$	$\sim$15mW	$\sim 70\mu$m	$0.037ea_0$ (see [100])	$2\pi \times 18$ MHz

Table 5.5: Experimental parameters, theoretical effective dipole moments, and Rabi frequencies for both of the transitions relevant to the molecule excitation process.

For large detunings Δ from the intermediate state, the effective 2-photon Rabi frequency Ω_{eff} is

$$\Omega_{\text{eff}} = \frac{\Omega_1\Omega_2}{2\Delta}. \tag{5.24}$$

For the intermediate-state detuning we use, $\Delta \approx 700$ MHz, we have $\Omega_{\text{eff}} \approx 2\pi \times 11$ MHz. With Eq. 5.19, this leads to $\eta/\eta_0 = 0.88$, though we note that this is likely an overestimate since the width of a vibrational wavefunction lobe also matters and is substantially shorter than Δ_w.

We consider the timescales of the excitation Rabi frequency and atom interaction time. An atom with velocity $v_{rms} = 0.21$ m/s interacting with on-resonant light experiences an effective π-pulse over $\sim$180 a_0. Despite this being much shorter than the distance traveled by the atom during the length of the 20-μs pulse (8.6×10^4 a_0), it is slightly longer than the span of the typical vibrational wavefunction for 24D-ground molecules ($\Delta_w \approx 150 a_0$). Thus, the long excitation pulse does not cause Rabi oscillations in a resonant atom pair because of the brevity of one single pair encounter. Nevertheless, the length of the pulse provides more opportunities for photoassociation by allowing more atom pair encounters to occur, for any given atom.

5.5.5 Estimated photoassociation rates

We estimate the photoassociation rates using Eq. 5.18, the previously derived $\eta/\eta_0 = 0.88$, and the values in Table 5.4, including the atom number $N_a \sim 2 \times 10^4$, which we estimate from absorption imaging of the atoms in the dipole trap. We obtain $2N_m/N_a = 0.008\eta_0$ and $N_m = 80\eta_0 \leq 80$. We typically observe the ion signals from the molecules to be a little less than 1 ion count. The factor of ~ 100 difference is easily accounted for by probable overestimations and significant uncertainties. In the first place, the observed N_m should be less than the predicted N_m/η_0 because η_0 should be somewhat less than 1, the ion detection efficiency of our system is limited ($\sim 30\%$), η may have been overestimated, and possible slight misalignment of the excitation beams would lead to a smaller effective N_a. Secondly, there are substantial uncertainties introduced from uncertainties in our beam intensities and atom number, and from our simplification of the physical picture of the photo-assisted collisions.

The strongest support for the photo-assisted collision analysis is that the predicted ratio $N_m/N_a \lesssim 0.004$ for $\eta_0 \lesssim 1$, which is independent of excitation beam overlap and ion detection efficiency, is quite close to our observation that N_m/N_a (where N_a is the ion count from the Rydberg atom resonance) is on the order of 0.01. In contrast, N_m/N_a based on the frozen gas approximation would be $(4\pi/3)(r_m^3 n_{\rm V}/2) = 6 \times 10^{-5}$.

5.5.6 Analysis of resonance linewidths

The linewidths of the molecular resonances vary from about 4 to 17 MHz. To account for these linewidths, we consider several sources of line broadening. Some broadening mechanisms which affect all resonances similarly are the combined linewidth of the excitation lasers (∼1 MHz), the Doppler broadening (∼0.3 MHz), and the thermal broadening due to stored mechanical energy such as discussed in subsection 5.5.3 ($< k_B T/h = 3.8$MHz). The linewidths due to tunneling decay vary significantly among the resonances but are typically in the range 1-100 kHz. Because none of these broadening sources account for the observed linewidths, I additionally consider broadening due to the short interaction time of an atom pair undergoing photoassociation.

The short interaction time comes from the relative velocity $\sqrt{2}v$ of the two atoms being photoassociated and limited width of the potential well Δ_w, i.e. the time $t = \Delta_w/(\sqrt{2}v)$ mentioned in subsection 5.5.2. The interaction-time broadening $\Delta\nu_i$ adds to the broadening from all other sources $\Delta\nu_0$ in quadrature to compose the total linewidth $\Delta\nu_t =$, i.e.

$$(\Delta\nu_t)^2 = (\Delta\nu_i)^2 + (\Delta\nu_0)^2. \tag{5.25}$$

To examine whether the magnitude and variance of observed linewidths may be due to interaction-time broadening, I use several crude approximations to relate the resonance linewidth, the vibrational wavefunction linewidth and the temperature. I

estimate that the interaction time broadening is

$$\Delta\nu_i = \frac{\sqrt{2}v}{2\pi\Delta_w}, \tag{5.26}$$

with a Δ_w proportional to the width of the largest peak in the vibrational wavefunction. For vibrational states that approach ground states of an isolated potential well, the wavefunctions are a single smooth peak. Higher vibrational states in a well have multiple peaks with narrower individual widths, and wavefunctions of states spanning multiple potential wells have more complex shapes. In the real ensemble of atoms undergoing random collisions, there is a distribution of path lengths traveled by the atom pair during which they are have the separation distance necessary for photoassociation, or in other words, during which they are in an imaginary spherical shell of a certain thickness and diameter. For an outer radius R and inner radius r, the path length is $R - r$ for a trajectory perpendicular to the shell and spans from 0 to $2\sqrt{R^2 - r^2}$ for an atom glancing the shell. For the present scenario where $(R - r)/R \approx 5 - 10\%$, the average path length for trajectories spread uniformly over the shell's cross-section, the average path length is about $2.5(R - r)$. I assume this to be representative of path length distribution and use 2.5 times the vibrational wavefunction peak width for Δ_w.

I use the thermal velocity $v^2 = 8k_BT/(\pi m)$ and Eq. 5.26 together with Eq. 5.25 to arrive at the linear equation

$$(\Delta\nu_t)^2 = \frac{4k_BT}{\pi^3 m}\left(\frac{1}{\Delta_w}\right)^2 + (\Delta\nu_0)^2. \tag{5.27}$$

I sample the observed linewidths and calculated vibrational wavefunction central widths for the resonances that are both observable in the spectra and able to be assigned to predicted resonances with reasonable certainty. For the observed linewidths, I use the data in Appendix A because the better signal quality allows a greater variety

of resonance widths to be included. The squares of the linewidths and of the inverse vibrational wavefunction widths are plotted in Fig. 5.8. The aggregate plot suggests that there may be an overall linear trend. The extracted linear slope and intercept (shown in the figure) correspond respectively to $T = 120\mu$K and $\Delta\nu_0 = 6$ MHz.

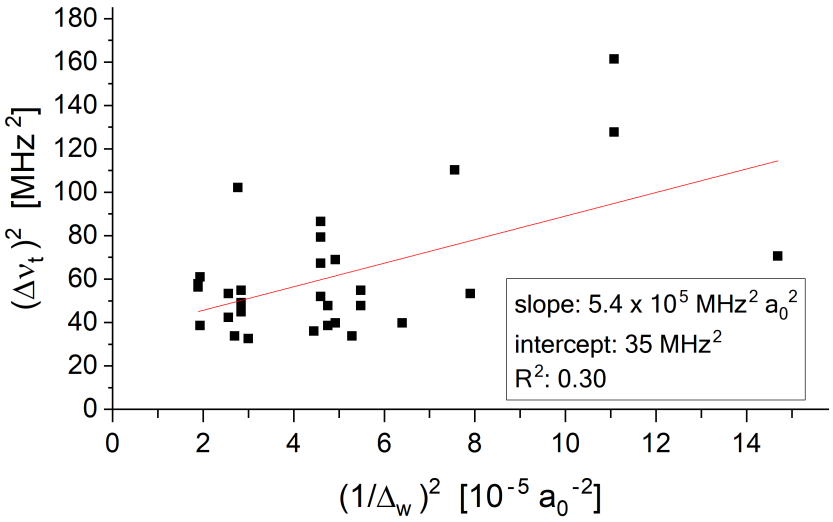

Figure 5.8: Observed linewidths from molecular resonances and inverse estimated effective widths of their corresponding vibrational wavefunctions.

The extracted temperature agrees surprisingly well with the measured temperature of 180μK, given the large uncertainties in the slope, the rudimentary nature of this model, and the fact that the linewidths were recorded on different days (allowing the possibility of different temperatures and Rabi frequencies). The extracted $\Delta\nu_0$ value, reflecting the broadening from other sources, also has large uncertainty. The true value may be more similar to that estimated for broadening due to stored mechanical energy ($\lesssim 3.8$ MHz), or it may be higher due to power broadening. While the analysis presented here is clearly insufficient to completely explain the variance in linewidths, it provides basis for the postulation that the primary source of broadening could be the short interaction times.

A proper estimation of the linewidth broadening from interaction times would involve a fully quantum mechanical calculation. It would account for the dynamic

Franck-Condon overlap of the traveling atomic wavepackets, comprising the ground state of the system, with the vibrational wavefunction of the excited (i.e. photo-associated) state. Interestingly, because the laser light's excitation of the two-atom system is coherent, it effectively entangles the center-of-mass dynamics with the internal state of the system.

5.5.7 Conclusion

Overall, we find reasonable agreement between our experimental observations and estimates made based on a simple kinematic model using a collisional picture. The estimates suggest—and the experiment confirms—that even with atom cloud temperatures and densities far from BEC conditions, photoassociation of Rydberg molecules may be readily observable.

5.6 Summary and outlook

In this chapter, I presented an experiment in which I probed long-range Rydberg molecules formed by a Rydberg atom and a ground-state atom. Three coupled angular momenta exist in the Rydberg molecule system presented here, and different combinations of their orientations correspond to molecular adiabatic potentials that vary, sometimes dramatically. I particularly focused on comparing the molecular binding energies resulting from each possible combination, and on using the binding energies to extract electron-atom scattering length functions. I outlined one of the standard ways to model the molecular potentials arising from such scattering, i.e. the Fermi pseudopotential together with diagonalization of the perturbed Hamiltonian of the Rydberg atom in a finite Rydberg basis, and showed how we adapted this model for translating the measured binding energies into scattering length functions. Finally, I discussed our experimental observation of substantial photoassociation rates despite, relative to BEC conditions, the significantly higher temperature and lower

density of the atom cloud. I considered several ways in which atom temperature could affect photoassociation, and showed how a simple photo-assisted collision picture can account for the observed rates, which are several orders of mag greater than those predicted from a frozen gas model.

Some tangible results of our experiment are as follows. We have measured 32 binding energies of $(24D_J{+}5S_{1/2})$ Rydberg-molecular states on PECs for both Rb isotopes. The low value of n leads to sub-% relative uncertainties and pronounced sensitivities to p-wave scattering. We have simultaneously fitted the s-wave and p-wave singlet and triplet scattering length functions $a_s^S(k)$, $a_s^T(k)$, $a_p^S(k)$, and $a_p^T(k)$, and we have highlighted the range of k for which the scattering length functions are most probed in this set of molecular resonances. These results as well as much of the content of this chapter have published in Ref. [50], which has garnered 14 citations according to Google Scholar as of August 2020.

The electron-atom scattering interaction may be characterized with a model as simple as a Fermi pseudopotential with considerable success; the model well-reproduces the qualitative features of the observed (albeit indirectly) molecular potentials in our experiment as well as those in many others [29, 56–61]. However, the model's reliability for making quantitative predictions is less clear. At small enough internuclear separations, it becomes fundamentally inaccurate to characterize the electron-atom interaction with scattering lengths because the electron can no longer be treated as a plane wave. Furthermore, even if the Fermi model were a perfect description, the diagonalization methods used in conjunction with it have convergence issues which limit the ultimate accuracy of the predicted potentials [97, 99]. Achieving accuracies on par with or better than the measurements of some experiments may be possible with the development of alternative approaches such as using R-matrix methods [96, 101–103], Greens-function-based models [68] that are adapted to account for spin interactions, or generalized local frame transformation theory (GLFT) [104].

The behavior of $a_p^T(k)$ near a shape resonance has a strong effect on states in the multiple-GHz-deep, inner wells around $610a_0$ and $710a_0$. Resonances of some of the shallowest of these wells, the wells at $710a_0$ for the $(24D_{5/2} + 5S_{1/2},\ F_<)$ potential, have small enough binding energies to be within the energy range we explored and appear in our data. The potential wells from resonances of the $24D_{3/2}$ are much deeper and even more strongly influenced by triplet p-wave scattering. In subsection 5.3.4, we show preliminary data that might be signatures of resonances in these potential wells. Additional studies could be done to verify the identity of the observed peaks and explore their properties—for example, by observing their dependence on n.

There are several interesting avenues to explore using the Rb molecular resonances that are strongly affected by p-wave scattering. First, the fine-structure splitting of the ${}^3P_{J=0,1,2}$ state of the Rb^- resonance can be probed with the molecular resonances [90, 105]. Along the same line, the resonance energies can be useful for estimating the location of the p-wave shape resonance or conversely, testing the models which predict resonances from scattering lengths. The J-averaged value of the p-wave shape resonance has been theoretically estimated to be about 22 meV [52, 54], while experimental studies have made estimates of < 50 meV using electron transmission spectroscopy [106], and most recently, 26.6 meV using spectroscopy of the deep inner potential wells in nS Rydberg molecules [90]. While our fitting procedure has not been designed to estimate the p-wave shape resonance nor do we necessarily expect it to do so accurately, it is possible to extract a value from our fitted functions. We note that it is about 37 meV (see Fig. 5.7), which significantly deviates from most of the aforementioned values given in the literature and may merit further investigation. Another intriguing possible application of molecular states with strong p-wave dependence, such as the ones discussed here, is to use them as an intermediate step in the creation of heavy-Rydberg states through stimulated emission [107].

Our experiment demonstrates successful photoassociation of Rydberg molecules

from an atom cloud at a temperature significantly higher than other experiments. We have constructed a basic picture for understanding how the thermal atomic motion contributes to higher count rates than would be expected from a frozen gas model, and may cause broadening of the resonance spectra that is dependent on the shape of each vibrational wavefunction. This effort paves the way to investigate dynamical processes in long-range Rydberg molecules, a subject which is full of exciting prospects but yet unexplored [30].

CHAPTER VI

Polarizability Measurement of Rb $5D_{3/2}$-State

"This is interesting stuff, but we can get even more interesting stuff."

– Paul Berman

6.1 Overview

The $5D_{3/2}$ dynamic polarizability and photoionization (PI) cross-section are proposed to be measured using double resonance spectroscopy in a ladder-type 3-level system, where the system is perturbed by the high-intensity 1064-nm dipole trap described in chapter IV, which induces substantial AC Stark shifts ("light shifts") on the levels. The method is similar to the one in Ref. [108] in that the upper-transition frequency is scanned for a set of various detunings of the lower-transition frequency, and the resulting ionization spectra give a ratio of the state polarizabilities that are independent of the 1064-nm intensity. It is difficult to extract a polarizability value from measuring the light shift of a single resonance relative to the light intensity because the light intensity is typically difficult to measure precisely. The technique of using double resonance spectroscopy circumvents this difficulty by relying on knowledge of other state polarizabilities instead of the light intensity. We expand and develop the earlier method by incorporating PI to extract a cross-section measurement from the spectra linewidth, and using a more sophisticated setup for laser frequency control

with improved precision.

6.2 Motivation

Atomic dynamic polarizabilities characterize the shift of atomic energy levels in response to an external alternating electric field. The polarizabilities depend on the atomic state and frequency of the external field. In optically trapped atoms, the state dependence leads to differential light shifts in the atomic transition frequencies. Thus precise knowledge of the dynamic polarizabilities becomes crucial in many applications such as in optical atomic clocks [109], magnetometers [110], atom interferometers [111, 112], and neutral-atom qubits [23, 113], where the differential light shifts must be either very well known or eliminated using carefully determined "magic" wavelengths for the dipole trap [114, 115].

If the frequency of the external electric field exceeds the ionization threshold, the light induces photoionization (PI) in addition to the atomic transition frequency shift. PI plays a role in a large variety of physical systems including astrophysical [116–118], ultracold [119, 120] and laser plasmas [121–123]. Experimental tests of PI cross-sections and of polarizabilities are both useful for refining fundamental theory of atomic structure calculations. The former reveal information about the coupling of the atomic wavefunctions to the continuum free states. The latter contain information mainly on bound-to-bound state matrix elements, which determine fundamental properties such as oscillator strengths, state lifetimes, and van der Waals C_6 coefficients. These topics are discussed in a number of publications, most notably in works by Safronova et. al. in which theoretical values are rigorously calculated [124–126] and in which experimental measurements have directly informed and refined the theoretical derivations [127–130].

Measurements of PI cross-sections have typically relied on the saturation technique [131] or the trap loss (or loading) technique [132]. Experimental challenges include

calibrating metrics for determining the absolute values of the photoionizing light intensity, the number of initial atoms, and the number of ions collected. In Rb, cross-sections (at various frequencies) have been measured for $5S_{1/2}$ [132–134], $5P_{3/2}$ [134–136], $6P_{1/2}$ and $6P_{3/2}$ [131], and $5D_{5/2}$ [137]. PI cross-sections for Rydberg states have also been measured in Rb [138, 139] and Cs [140].

The experimental determination of the dynamic polarizability of $5D_{3/2}$ is the primary goal of our experiment. No theoretical or experimental estimate has been made for this state at any wavelength. However, the static polarizabilities have been investigated [10, 141–143], as well as the dynamic polarizability at 778.1nm for $5D_{5/2}$ [144].

The Rb $5D$ states in particular are appealing to study for several reasons. First, there has been continued interest ranging from earlier decades [39, 145, 146] to recent years [147–149] in using the two-photon transition $5S_{1/2} \rightarrow 5D_J$ as an optical frequency reference, which necessitates precise calculation or cancellation of the relevant light shifts [150, 151]. The transition is favorable because it is narrow (natural linewidth < 1 MHz), stable, relatively strong, and can be Doppler-free without using laser cooling. At the same time, the transition wavelength (778 nm) is both experimentally convenient and a second harmonic of 1556 nm, which falls within the telecommunication band. The $5S_{1/2} \rightarrow 5D_{5/2}$ transition is also one of the recommended transitions by the Consultative Committee of Length (CCL) for the practical definition of the meter [152]. A further advantage of probing a Rb $5D$ state is that the PI rate by 1064nm light is the same order of magnitude as the shift in transition frequency, which means that, using the method described here, information about the state's polarizability and PI cross-section is accessible simultaneously.

6.3 Principles of experiment

6.3.1 Lattice-induced AC Stark Shifts

The experiment probes a stepwise two-photon-transition $5S_{1/2} \rightarrow 5P_{1/2} \rightarrow 5D_{3/2}$ of Rb atoms trapped in the 1064-nm one-dimensional lattice dipole trap. The electric field of the linearly-polarized dipole trap is $\mathbf{E} = \hat{\boldsymbol{\epsilon}} E_0(\rho, z)\cos(\omega t)$, where E_0 is the amplitude, $\omega = 2\pi c/1064\text{nm}$, and $(\rho,\, z)$ denote the spatial coordinates of the center-of-mass of an atom. In the presence of the dipole trap, each of the atomic energy levels experiences a light shift proportional to the square of the electric field amplitude [or alternatively, to light intensity, since $E_0^2 = 2I/(c\epsilon_0)$]. To establish the conceptual framework, we first consider the light shifts neglecting hyperfine structure and later expand the analysis to incorporate hyperfine structure. Without hyperfine structure included, the level shifts are:

$$\Delta_i(\rho, z) = -\frac{1}{4}\alpha_i(\omega) E_0^2(r, z), \quad i = 5S,\ 5P,\ 5D \tag{6.1}$$

where $\alpha_i(\omega)$ is the *total* dynamic polarizability of state $|i\rangle$. For ease of notation, we will refer to the states $5S_{1/2}$, $5P_{1/2}$, and $5D_{3/2}$ as simply $5S$, $5P$, and $5D$. Note, however, that the polarizabilities for states of different J are not equivalent. It is also noteworthy that Eq. 6.1 is only applicable when the size of the atoms is small enough in comparison to the spatial variation of the electric field so that only the electric field at the location of the center of the atom is relevant. This condition is not the case, for example, for Rydberg atoms in an optical lattice.

6.3.2 Dynamic polarizabilities

Polarizabilities have at least an m_J-independent scalar component, and, for some values of J and light polarizations, vector components and/or rank-2 tensor components with m_J-dependent factors. For linear polarization (as in the present case),

there is no vector component. The total polarizability is then:

$$\alpha_i(\omega) = \alpha_i^{(0)}(\omega) + \eta(m_J)\alpha_i^{(2)}(\omega) \tag{6.2}$$

where $\alpha_i^{(0)}(\omega)$ and $\alpha_i^{(2)}(\omega)$ are the scalar and rank-2 tensor components respectively, and m_J-dependence is contained in η. First, we concentrate on the scalar component and neglect hyperfine structure, leaving the tensor component and hyperfine structure for further discussion in section 6.4.

The scalar component $\alpha^{(0)}(\omega)$ is a sum of transition matrix elements from state $|i\rangle$ to all other states $|k\rangle$ with factors related to the energy difference between states:

$$\alpha_i^{(0)}(\omega) = \frac{2}{3}\sum_k \frac{\omega_{ki}|\langle i \parallel \mathbf{d} \parallel k\rangle|^2}{\hbar(\omega_{ki}^2 - \omega^2)} \tag{6.3}$$

where $\omega_{ki} = (E_k - E_i)/\hbar$, E_i and E_k are the energies of states $|i\rangle$ and $|k\rangle$, and $\langle i \parallel \mathbf{d} \parallel k\rangle$ is the reduced electric dipole matrix element between states $|i\rangle$ and $|k\rangle$. Note that in general, the sum over k should include an integration over the continuum states in addition to the summation of the bound ones. This increases in importance when the photon energy exceeds the ionization energy, as is the case for $|i\rangle = 5D_{3/2}$ at $\omega = 2\pi c/1064\text{nm}$.

The sign and magnitude of the polarizability values for each state may be intuitively understood from considering the strong transitions from that state. For $5S_{1/2}$, the dominant contributions to the polarizability are from transitions to $5P_{1/2}$ and $5P_{3/2}$. Because these are higher-energy states and blue-detuned from ω ($\omega_{ki} > 0$, $\omega_{ki}^2 > \omega^2$), the polarizability is positive (corresponding to a negative light shift). For Rb $5P_{1/2}$, the transitions to $4D_{3/2}$, $6S_{1/2}$, and $5S_{1/2}$ contribute strongly. For all three of these, the transitions are either red-detuned and positive ($\omega_{ki} < 0$, $\omega_{ki}^2 > \omega^2$) or blue-detuned and negative ($\omega_{ki} > 0$, $\omega_{ki}^2 < \omega^2$), leading to a large negative polarizability (positive light shift).

The quantitative values of the dynamic polarizabilities of $5S_{1/2}$ and $5P_{1/2}$ at 1064nm have been theoretically estimated to be 687.3(5) [34] and -1226(18) [153]. We use these values in determining the $5D_{3/2}$ polarizability from the measurement. The value we determine can be adapted with improved values of $5S_{1/2}$ and $5P_{1/2}$ at any time, if and when they become available. For $5S_{1/2}$, an experimental estimate [154] and earlier theoretical estimate [155] have also been made.

Before collecting experimental data, an initial estimate of the polarizability was made in order to guide the experimental setup. The estimated contributions from various transitions are summarized in Table 6.1 and explained as follows. In Refs. [125, 126], the listing of either the dipole matrix elements themselves or the contributions of each transition to other polarizabilities allow the calculation of the equivalent contribution for the dynamic polarizability at an arbitrary frequency, using Eq. 6.3. In this way, I estimated most of the important contributions to get an approximate value of the dynamic polarizability. Some transitions that are important for 1064nm but not for the static case are missing from the published data, requiring alternative methods of estimation with greater uncertainty. In Table 6.1, the contribution from $5D_{3/2} \rightarrow 6F_{5/2}$ was estimated using the contribution to the static tensor polarizability and the J-dependent factors which relate the scalar and tensor contributions. The $(7 \leq n \leq 30)F_{5/2}$ and $(9 \leq n \leq 13)P_J$ contributions were found using the reduced dipole matrix elements given using an online atom calculator [156]. The contributions from high-n bound transitions were approximated by observing the trend of the contributions with increasing n. The core contribution was estimated to be of a comparable value as that at 778nm [144]. The continuum contribution was not estimated but may be significant since it is integrated across the point where the difference of the square frequencies $\omega_{ki}^2 - \omega^2$ (the denominator in Eq. 6.3) equals zero. The sum of the contributions has a high degree of uncertainty, which makes an experimental determination the more important.

The rank-2 tensor polarizability of $5D_{3/2}$ is estimated to be small, on the order of 20. Because this is comparable to the uncertainty we expect in the scalar polarizability measurement, it may be too small to measure with our current experiment.

6.3.3 Intensity profile of lattice

Spatially, the light shifts follow the Gaussian profile of the intensity in the radial direction and sine-squared lattice pattern in the longitudinal direction. The squared electric field (proportional to intensity) is:

$$E^2(\rho, z) = E_0^2 e^{-(2\rho/w_0)^2} \frac{(1 + \cos 2kz)}{2}, \quad k = \frac{2\pi}{\lambda} \tag{6.4}$$

where w_0 is the lattice waist diameter (23 μm), and λ is the trapping laser wavelength (1064 nm).

6.3.4 Measuring polarizability from atomic transition shifts

The transition shifts are, using Eq. 6.1:

$$\Delta_{5S\to5P}(\rho, z) = \Delta_{5P}(\rho, z) - \Delta_{5S}(\rho, z) = -\frac{1}{4}E^2(\rho, z)(\alpha_{5P} - \alpha_{5S}) \tag{6.5}$$

$$\Delta_{5P\to5D}(\rho, z) = \Delta_{5D}(\rho, z) - \Delta_{5P}(\rho, z) = -\frac{1}{4}E^2(\rho, z)(\alpha_{5D} - \alpha_{5P}) \tag{6.6}$$

Because of the spatial distribution of the atoms in the lattice, there is a range of transition shifts available within the atomic sample. A lower-transition laser at a certain detuning from the unperturbed transition frequency will interact with a select fraction (if any) of the atoms, i.e. the ones which happen to be located at the appropriate intensity that makes the lower-transition resonant. The upper-transition laser in turn will only be able to excite the same fraction of atoms and at a specific detuning. In this way, the upper-transition shift is directly related to the lower-transition shift regardless of the intensity class that is being probed.

State $\|k\rangle$	$2\pi c/\omega_{ki}$ (nm)	Contribution to static polarizability (a_0^3)	Dipole reduced matrix element $\langle J \,\|\mathrm{d}\|\, J'\rangle$ (a.u.)	Contribution to 1064nm dynamic polarizability (a_0^3)
$6P_{1/2}$	-5037	$-6100(59)$[a]		284.9
$7P_{1/2}$	4685	$1910(91)$[a]		-103.9
$6P_{3/2}$	-5241	$-1291(9)$[a]		55.5
$7P_{3/2}$	4609	$356(18)$[a]		-20.0
$4F_{5/2}$	9161	$21546(95)$[a]		-294.6
$5F_{5/2}$	2795	$898(54)$[a]		-152.1
$5P_{1/2}$	-762.1		1.616[b]	-14.9
$8P_{1/2}$	2419		2.463[a]	-12.9
$5P_{3/2}$	-776.2		0.787[b]	-3.8
$8P_{3/2}$	2408		1.096[a]	-2.6
$6F_{5/2}$	2029			-73.9[c]
$7F_{5/2}$	1742		0.985[d]	-44.8
$8F_{5/2}$	1595		0.529[d]	-29.7
$9F_{5/2}$	1508		0.321[d]	-21.1
$10F_{5/2}$	1452		0.212[d]	-15.7
$11F_{5/2}$	1412		0.148[d]	-12.1
$12F_{5/2}$	1384		0.108[d]	-9.5
$13F_{5/2}$	1362		0.082[d]	-7.6
(14-30)$F_{5/2}$				-40.3[e]
(n>30)$F_{5/2}$				~ -7[f]
(9-13)$P_{1/2}$				-11.6[e]
(9-13)$P_{3/2}$				-2.3[e]
(n>13)P_J				~ -3[f]
Core				~ 10[g]
Continuum				?
Sum				$\sim$ **−533**

[a] Safronova et. al. PRA 83(5) 052208, 2011.
[b] Safronova et. al. PRA 69(2) 022509, 2004.
[c] Calculated from tensor polarizability given in:
Safronova et. al. PRA 83(5) 052208, 2011.
[d] https://atomcalc.jqc.org.uk/.
[e] Calculated from reduced dipole matrix elements given by:
https://atomcalc.jqc.org.uk/.
[f] Estimated from trend of reduced dipole matrix elements given by:
https://atomcalc.jqc.org.uk/.
[g] Guess based on core contribution to dynamic polarizability at 778nm:
Martin et. al. PRA 100(2) 0234117, 2019.

Table 6.1: Initial estimate of $5D_{3/2}$ scalar polarizability at 1064nm, using published theoretical values of static polarizability contributions and dipole matrix elements.

The stepwise two-photon excitation and transition shifts are illustrated in Fig. 6.1. Outside the lattice, when $\rho \gg w_0$, the levels are unshifted and the transitions have resonance frequencies ω_1, ω_2 equal to the field-free resonance frequencies ω_1^*, ω_2^*. Within the lattice, the atomic levels are shifted according to their positions, and the resonance frequencies become $\omega_1 = \omega_1^* + \Delta_{5S\to5P}(\rho, z)$ and $\omega_2 = \omega_2^* + \Delta_{5P\to5D}(\rho, z)$.

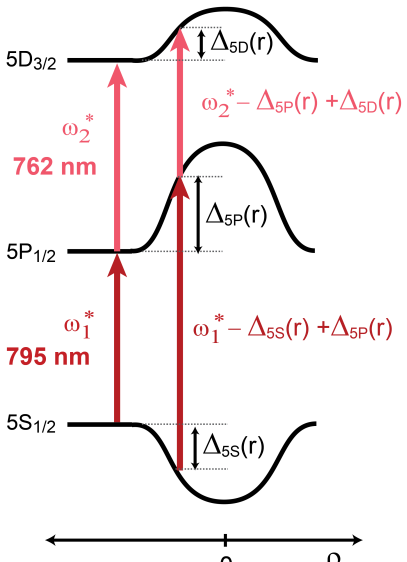

Figure 6.1: Illustration of the AC Stark shifts of the relevant energy levels as a function of radial position with respect to the 1064-nm dipole trap, at a fixed longitudinal position z that does not coincide with a node, and corresponding shifts in resonance frequencies.

The ratio of Eqs. 6.5 and 6.6 relate the two transition shifts to the state polarizabilities independently of the intensity at the atom location. The pairs of upper- and lower-transition detunings that correspond to a doubly-resonant excitation may be found experimentally, as will be described. Then, if two of the three polarizabilities are known (in this case, α_{5S} and α_{5P}), the third may be solved for:

$$\alpha_{5D} = \left(\frac{\Delta_{5P\to5D}(\rho, z)}{\Delta_{5S\to5P}(\rho, z)}\right)(-\alpha_{5S} + \alpha_{5P}) + \alpha_{5P} \tag{6.7}$$

We define the detunings of the lower- and upper-transition lasers from the field free resonances as Δ_{795} and Δ_{762}. Finding a single pair of laser detunings (Δ_{795}, Δ_{762}) that are doubly resonant with a pair of level shifts ($\Delta_{5S\to5P}$, $\Delta_{5P\to5D}$) is in principle

sufficient to deduce a polarizability estimate, but the experimental uncertainty can be improved by obtaining a series of spectra at various detunings. In the experiment, we create a 2-dimensional map of the spectra (as a function of the Δ_{795} and Δ_{762}) and extract the slope of the dominant spectral feature, which is then used in Eq. 6.7.

For the available 1064-nm intensity of $I_{max} \sim 1.7 \times 10^7$ W/cm^2 and the previously estimated polarizabilities, the anticipated maximum shifts are about $\Delta_{5S\rightarrow 5P,max} = +1.5$ GHz and $\Delta_{5P\rightarrow 5D,max} = -0.5$ GHz. It is important to know these approximate ranges while designing the experiment in order to ensure that the excitation lasers can be locked and scanned in the appropriate ranges.

We note that a second peak should appear in the spectra when both transitions $5S_{1/2} \rightarrow 5P_{1/2}(F'=1) \rightarrow 5D_{3/2}$ and $5S_{1/2} \rightarrow 5P_{1/2}(F'=2) \rightarrow 5D_{3/2}$ are possible. This means that there may be two values of $E_0^2/4$ present where the lower excitation is on resonance:

$$\frac{E_0^2}{4} = \begin{cases} \dfrac{\Delta_{795}}{-\alpha_{5S_{1/2}} + \alpha_{5P_{1/2}}} \\ \\ \dfrac{\Delta_{795} + \Delta_{HF}}{-\alpha_{5S_{1/2}} + \alpha_{5P_{1/2}}} \end{cases} . \tag{6.8}$$

We use the fact that a resonance with $5D$ requires that, regardless of the intermediate state,

$$\begin{aligned} \Delta_{795} + \Delta_{762} &= \Delta_{5D} - \Delta_{5S} \\ &= -\frac{E_0^2}{4}(\alpha_{5D} - \alpha_{5S}). \end{aligned} \tag{6.9}$$

Combining this relation with Eq. 6.8, and assuming a fixed detuning for Δ_{795} gives

two values for Δ_{762} where there are doubly-resonant transitions,

$$\Delta_{762} = \begin{cases} (\alpha_{5D} - \alpha_{5S}) \left(\dfrac{\Delta_{795}}{-\alpha_{5S} + \alpha_{5P}} \right) - \Delta_{795} \\ \\ (\alpha_{5D} - \alpha_{5S}) \left(\dfrac{\Delta_{795} + \Delta_{HF}}{-\alpha_{5S} + \alpha_{5P}} \right) - \Delta_{795} \quad , \end{cases} \tag{6.10}$$

which give a difference in Δ_{762} of

$$[\Delta_{762}\,]_1 - [\Delta_{762}\,]_2 = \Delta_{HF} \left(\frac{-\alpha_{5S} + \alpha_{5D}}{-\alpha_{5S} + \alpha_{5P}} \right). \tag{6.11}$$

Using values of $\Delta_{HF} = 361.6$ MHz (for ^{85}Rb), the theoretically calculated polarizabilities $\alpha_{5S_{1/2}} = 687.3(5)$ and $\alpha_{5P_{1/2}} = -1226(18)$, and our rough estimate $\alpha^{(S+T)}_{5D_{3/2}} = -533$, we estimate the separation to be about 230 MHz.

6.3.5 Photoionization cross section

The photoionization (PI) rate is:

$$R_{PI} = \frac{I}{\hbar\omega}\sigma(\omega) \tag{6.12}$$

where I and ω are the intensity and frequency of the photoionizing light, and $\sigma(\omega)$ is the PI cross-section. The expected contribution of the PI to the resonance linewidth is, in frequency units:

$$W_{PI} = \frac{R_{PI}}{2\pi} = \frac{I\lambda}{(2\pi)^2\hbar c}\sigma(\omega) \tag{6.13}$$

The PI cross section of $5D_{3/2}$ at $\lambda = 1064$ nm is expected to be similar to that of $5D_{5/2}$, which has been measured to be 18 Mb [137]. Using this value as an estimate and an intensity of 1.7×10^7 W/cm^2, the expected broadening is $\sim$260 MHz. The expected PI broadening is smaller but of the same order of magnitude as the transition

light shifts, which is a good experimental scenario for being able to measure both the polarizability and the PI cross-section. The PI linewidth is small enough so that the linecenters of the shifted spectra may still be determined with good precision, but also large enough so that it can be distinguished from other broadening mechanisms.

6.4 AC Stark shifts in high and low optical intensities

Dynamic polarizabilities of an atomic state encapsulate the relation between the energy shift of the state due to an optical field, and the intensity of the field. First, I present an analytical derivation of the polarizabilities and light shifts neglecting hyperfine structure. Subsequently I discuss how to include the hyperfine structure, and how the Hamiltonian may be diagonalized in different bases depending on whether the optical intensity is high or low in comparison to the hyperfine coupling strength.

6.4.1 AC Stark shifts neglecting hyperfine structure

The basic procedure for deriving the scalar, vector, and rank-2-tensor polarizabilities in terms of dipole matrix elements is outlined here. An even more thorough derivation and analysis may be found in Ref. [9].

We begin with a monochromatic optical field of general polarization and propagating in the z-direction,

$$\mathbf{E} = \frac{1}{2}E_0(\rho, z)\hat{\boldsymbol{\varepsilon}}e^{i(kz-\omega t)} + \frac{1}{2}E_0(\rho, z)\hat{\boldsymbol{\varepsilon}}^* e^{-i(kz-\omega t)}, \tag{6.14}$$

where $\hat{\boldsymbol{\varepsilon}}$ is the complex unit vector $\hat{\boldsymbol{\varepsilon}} = \cos\phi\ \hat{\mathbf{e}}_x + i\sin\phi\ \hat{\mathbf{e}}_y$, and ϕ is related to the polarization of the beam. For the case of linear polarization (which we will assume later), ϕ is an integer multiple of $\pi/2$. For linear polarization in an arbitrary direction, the field is $\mathbf{E}^{(\mathrm{lin})} = \hat{\boldsymbol{\epsilon}}E_0(\rho, z)\cos(kz - \omega t)$ where $\hat{\boldsymbol{\epsilon}}$ is a real-valued unit vector transverse to $\hat{\mathbf{z}}$. We define the angles θ_k and θ_p in relation to the quantization

axis for the atomic angular momentum, $\hat{\boldsymbol{e}}_M$, as

$$\cos\theta_k = \hat{\mathbf{e}}_z \cdot \hat{\boldsymbol{e}}_M$$
$$\cos^2\theta_p = |\hat{\boldsymbol{\varepsilon}} \cdot \hat{\boldsymbol{e}}_M|^2;$$

these angles will be used in our final result for the energy shift for the general case of any polarization and choice of quantization axis, in Eq. 6.32. The atom-field interaction Hamiltonian in the electric dipole approximation is

$$H_{AF} = -\mathbf{d}\cdot\mathbf{E} = -\frac{1}{2}E_0(\mathbf{d}\cdot\hat{\boldsymbol{\varepsilon}}e^{i(kz-\omega t)} + \mathbf{d}\cdot\hat{\boldsymbol{\varepsilon}}^* e^{-i(kz-\omega t)}). \tag{6.15}$$

For non-hydrogenic states (where the state is not degenerate) and when the dipole approximation has been made, there is no energy shift due to first-order perturbation. In second-order perturbation theory, the time-averaged energy shift in the atomic state of interest $|i\rangle$ by perturbing states $|k\rangle$ is

$$\begin{aligned}\Delta E_i &= -\frac{|E_0|^2}{4}\sum_k \left[\frac{\langle i|\mathbf{d}\cdot\hat{\boldsymbol{\varepsilon}}^*|k\rangle\langle k|\mathbf{d}\cdot\hat{\boldsymbol{\varepsilon}}|i\rangle}{E_{ki}-\hbar\omega} + \frac{\langle i|\mathbf{d}\cdot\hat{\boldsymbol{\varepsilon}}|k\rangle\langle k|\mathbf{d}\cdot\hat{\boldsymbol{\varepsilon}}^*|i\rangle}{E_{ki}+\hbar\omega}\right] \\ &= -\frac{|E_0|^2}{4}\sum_k \frac{\langle i|d_\mu|k\rangle\langle k|d_\nu|i\rangle}{\hbar(\omega_{ki}^2-\omega^2)}\left[\varepsilon_\mu^*\varepsilon_\nu(\omega_{ki}+\omega) + \varepsilon_\mu\varepsilon_\nu^*(\omega_{ki}-\omega)\right],\end{aligned} \tag{6.16}$$

where $E_{ki} = E_k - E_i$, $\omega_{ki} = E_{ki}/\hbar$, E_i and E_k are the respective energies of states $|i\rangle$ and $|k\rangle$, μ and ν are Cartesian coordinates, and the Einstein summation convention is used.

Here, we will consider the $|J\ m_J\rangle$ basis, which is applicable when neglecting hyperfine structure, or when the field-induced AC shifts far exceed the hyperfine structure. The equivalent solution for the $|F\ m_F\rangle$ basis may be found by substituting J and m_J

with F and m_F. Now, Eq. 6.16 is

$$\Delta E_{J,m_J} = -\frac{E_0^2}{4} \sum_{J'} \frac{1}{\hbar(\omega_{J'J}^2 - \omega^2)} S_{\mu\nu} Q_{\mu\nu}, \tag{6.17}$$

where $S_{\mu\nu}$ and $Q_{\mu\nu}$ are the rank-2 tensors

$$S_{\mu\nu} = \sum_{m'_J} \langle J\ m_J | d_\mu | J'\ m'_J \rangle \langle J'\ m'_J | d_\nu | J\ m_J \rangle \tag{6.18}$$

$$Q_{\mu\nu} = \varepsilon_\mu^* \varepsilon_\nu (\omega_{JJ'} + \omega) + \varepsilon_\mu \varepsilon_\nu^* (\omega_{JJ'} - \omega). \tag{6.19}$$

Any rank-2 tensor $T_{\mu\nu}$ may be decomposed into irreducible parts as

$$T_{\mu\nu} = \frac{1}{3} T^{(0)} \delta_{\mu\nu} + \frac{1}{4} T_\sigma^{(1)} \epsilon_{\sigma\mu\nu} + T_{\mu\nu}^{(2)}, \tag{6.20}$$

where $\epsilon_{\sigma\mu\nu}$ is the Levi-Civita symbol and the scalar $T^{(0)}$, the vector $T^{(1)}$ and the rank-2 tensor $T^{(2)}$ are Cartesian tensors,

$$T^{(0)} = T_{\mu\mu} \tag{6.21}$$

$$T_\sigma^{(1)} = \epsilon_{\sigma\mu\nu} (T_{\mu\nu} - T_{\nu\mu}) \tag{6.22}$$

$$T_{\mu\nu}^{(2)} = \frac{(T_{\mu\nu} + T_{\nu\mu})}{2} - \frac{1}{3} T_{\sigma\sigma} \delta_{\mu\nu}. \tag{6.23}$$

Using Eq. 6.20 for $S_{\mu\nu}$ in Eq. 6.17 yields

$$\Delta E_i = -\frac{E_0^2}{4} \sum_{J'} \frac{1}{\hbar(\omega_{J'J}^2 - \omega^2)} \left(\frac{1}{3} S^{(0)} \delta_{\mu\nu} + \frac{1}{4} S_\sigma^{(1)} \epsilon_{\sigma\mu\nu} + S_{\mu\nu}^{(2)} \right) Q_{\mu\nu}. \tag{6.24}$$

Using the Wigner-Eckhart theorem allows us to write each of the scalar, vector,

and tensor components of $S_{\mu\nu}$ in terms of reduced dipole matrix elements, as

$$S^{(0)} = S_{\mu\mu} = |\langle J \parallel \mathbf{d} \parallel J\rangle|^2 \tag{6.25}$$

$$S^{(1)} = (-1)^{J+J'}(-i)\sqrt{\frac{24(2J+1)}{J(J+1)}} \begin{Bmatrix} 1 & 1 & 1 \\ J & J & J' \end{Bmatrix} |\langle J \parallel \mathbf{d} \parallel J\rangle|^2 m_J \delta_{q0} \tag{6.26}$$

$$S^{(2)} = (-1)^{J+J'}\sqrt{\frac{5(2J+1)}{J(J+1)(2J-1)(2J+3)}} \begin{Bmatrix} 1 & 1 & 2 \\ J & J & J' \end{Bmatrix} \times \ |\langle J \parallel \mathbf{d} \parallel J\rangle|^2 [m_J^2 - J(J+1)]\delta_{q0}, \tag{6.27}$$

where q is the qth component in the spherical basis of a tensor $T_q^{(k)}$, and the spherical basis is defined such that $q = 0$ corresponds to the axis of quantization $\hat{\mathbf{e}}_M$. Here, the reduced dipole matrix elements are written according to the convention defined by [9, 157]:

$$|\langle \alpha j \parallel \mathbf{T}^{(k)} \parallel \alpha' j'\rangle|^2 = \sum_{m'q} |\langle \alpha j m | T_q^{(k)} | \alpha' j' m'\rangle|^2 = \sum_{m'} |\langle \alpha j m | \mathbf{T}^{(k)} | \alpha' j' m'\rangle|^2 \tag{6.28}$$

There is a common alternate convention that leads to a difference in the square reduced matrix elements by a factor of $(2J + 1)$.

Now we turn to $Q_{\mu\nu}$ and the other remaining tensors in Eq. 6.24. The rank-0 part is

$$\delta_{\mu\nu} Q_{\mu\nu} = Q_{\mu\mu} = (\varepsilon \cdot \varepsilon^*)\ 2\omega_{J'J} = 2\omega_{J'J}. \tag{6.29}$$

Since the rank-1 and rank-2 parts each include δ_{q0} from the results of $S^{(1)}$ and $S^{(2)}$, we convert the remaining tensor components to the spherical basis in order to apply

it.

$$\begin{aligned}
\delta_{q0}\left[\epsilon_{\sigma\mu\nu}Q_{\mu\nu}\right] &= \delta_{q0}\left[(\boldsymbol{\varepsilon}^* \times \boldsymbol{\varepsilon})(\omega_{J'J}+\omega) + (\boldsymbol{\varepsilon} \times \boldsymbol{\varepsilon}^*)(\omega_{J'J}-\omega)\right] \\
&= 2\omega\delta_{q0}\left[(\boldsymbol{\varepsilon}^* \times \boldsymbol{\varepsilon})\right] \\
&= 2\omega\delta_{q0}\left[\sqrt{2}i(\varepsilon^*\varepsilon)^{(1)}_q\right] \\
&= 2\omega(\boldsymbol{\varepsilon^*} \times \boldsymbol{\varepsilon}) \cdot \hat{\mathbf{e}}_M \\
&= 2\omega(i\sin 2\phi)\ \hat{\mathbf{e}}_z \cdot \hat{\mathbf{e}}_M \\
&= 2\omega(i\sin 2\phi\ \ \cos\theta_k)
\end{aligned} \tag{6.30}$$

$$\begin{aligned}
\delta_{q0}\left[Q^{(2)}_{\mu\nu}\right] &= (Q_{\mu\nu})^{(2)}_0 \\
&= (Q_{\nu\mu})^{(2)}_0 \\
&= 2\omega_{J'J}(\varepsilon_\mu\varepsilon^*_\nu)^{(2)}_0 \\
&= 2\omega_{J'J}\frac{(3\varepsilon_0\varepsilon^*_0 - \varepsilon\cdot\varepsilon^*)}{\sqrt{6}} \\
&= 2\omega_{J'J}\frac{(3|\varepsilon\cdot\hat{\mathbf{e}}_M|^2 - 1)}{\sqrt{6}} \\
&= 2\omega_{J'J}\frac{(3\cos^2\theta_p - 1)}{\sqrt{6}}
\end{aligned} \tag{6.31}$$

Now we use Eq. 6.25-6.31 in Eq. 6.24 to obtain:

$$\begin{aligned}
\Delta E(J, m_J; \omega) = -\frac{E_0^2}{4}\Bigg[&\alpha^{(0)}(J;\omega) + \sin 2\phi\cos\theta_k\left(\frac{m_J}{2J}\right)\alpha^{(1)}(J;\omega) \\
&+ \left(\frac{3\cos\theta_p^2 - 1}{2}\right)\left(\frac{3m_J^2 - J(J+1)}{J(2J-1)}\right)\alpha^{(2)}(J;\omega)\Bigg], \\
&\text{(general polarization and quantization axis)}
\end{aligned} \tag{6.32}$$

where the last term equals zero when $J = 1/2$ and

$$\alpha^{(0)}(J;\omega) = \sum_{J'} \frac{2\omega_{J'J}|\langle J \parallel \mathbf{d} \parallel J'\rangle|^2}{3\hbar(\omega_{J'J}^2 - \omega^2)} \tag{6.33}$$

$$\alpha^{(1)}(J;\omega) = \sum_{J'} (-1)^{J+J'} \sqrt{\frac{6J(2J+1)}{J+1}} \begin{Bmatrix} 1 & 1 & 1 \\ J & J & J' \end{Bmatrix} \frac{2\omega|\langle J \parallel \mathbf{d} \parallel J'\rangle|^2}{\hbar(\omega_{J'J}^2 - \omega^2)} \tag{6.34}$$

$$\alpha^{(2)}(J;\omega) = \sum_{J'} (-1)^{J+J'} \sqrt{\frac{10J(2J+1)(2J-1)}{3(J+1)(2J+3)}} \begin{Bmatrix} 1 & 1 & 2 \\ J & J & J' \end{Bmatrix} \frac{2\omega_{J'J}|\langle J \parallel \mathbf{d} \parallel J'\rangle|^2}{\hbar(\omega_{J'J}^2 - \omega^2)}. \tag{6.35}$$

When the light polarization is linear, which implies that ϕ is an integer value of $\pi/2$, the vector (rank-1 tensor) term becomes zero. Choosing the quantization axis to be perpendicular to the direction of the light (i.e. $\cos^2\theta_p = 1$) then leads to the energy shift

$$\boxed{\Delta E(J, m_J;\omega)^{(\mathrm{lin})} = -\frac{E_0^2}{4}\left[\alpha^{(0)}(J;\omega) + \left(\frac{3m_J^2 - J(J+1)}{J(2J-1)}\right)\alpha^{(2)}(J;\omega)\right]. \quad \text{(linearly polarized, quantization axis } \hat{\mathbf{e}}_M \perp \hat{\mathbf{e}}_z\text{)}} \tag{6.36}$$

Thus we see that, for this case, the relation between energy shift and the field is contained in only two parameters, $\alpha^{(0)}$ and $\alpha^{(2)}$, which represent contributions from many dipole matrix elements (according to Eqs. 6.33 and 6.35) between bound-bound states $|i\rangle$ and $|k\rangle$ and should also include contributions from transitions to the continuum states.. The polarizabilities should also include contributions from transitions to the continuum free states. Our objective is to measure these polarizability parameters for the $5D_{3/2}$ state, as well as its photoionization cross-section.

6.4.2 Hamiltonian including hyperfine structure

The Hamiltonian for an atom interacting with a linearly polarized light field $\mathbf{E}(t) = \mathbf{E}_0 \cos(\omega t)$, including the atomic hyperfine structure, is

$$H = -\mathbf{d}(\omega) \cdot \mathbf{E}(\omega) + A_{\mathrm{HFS}} \hat{\mathbf{I}} \cdot \hat{\mathbf{J}} + B_{\mathrm{HFS}} \frac{3(\hat{\mathbf{I}} \cdot \hat{\mathbf{J}})^2 + \frac{3}{2}\hat{\mathbf{I}} \cdot \hat{\mathbf{J}} - I(I+1)J(J+1)}{2IJ(2I-1)(2J-1)} \quad (6.37)$$

where $\mathbf{d}(\omega)$ is the induced dipole of the atomic state with polarizability α ($\mathbf{d}(\omega) = \alpha(\omega)\mathbf{E}(\omega)$), A_{HFS} and B_{HFS} are the magnetic-dipole and electric-quadrupole hyperfine constants of the atom.

In general, the polarizabilities depend on all of the angular momentum couplings present in the system; the Hamiltonian is not necessarily diagonal in either of the $|JIm_J m_I\rangle$ or $|\gamma J m_J\rangle$ bases. We use Eq. 6.37 to numerically model of the system at arbitrary optical intensities, but further insight can be gained from considering two scenarios of optical intensities: when the AC Stark shift is much higher than the hyperfine coupling strength, and when it is much lower.

6.4.3 High-optical-intensity (strong field) regime

When the AC Stark shift is larger than the hyperfine coupling strength (but still smaller than the fine structure coupling), the Hamiltonian is approximately diagonal in the $|JIm_J m_I\rangle$ basis. Assuming that the light is linearly polarized in a direction perpendicular to the quantization axis, we may follow the same method as in section 6.4.1 an atom in state $|\gamma J m_J\rangle$ experiences the approximately the same energy shift as that in Eq. 6.36, i.e.

$$\begin{aligned} \Delta E_{\gamma J m_J}(\omega) &\approx \frac{1}{2}\alpha_{\gamma J m_J}(\omega)\mathbf{E}_0^2 \\ &= -\frac{1}{4}(\alpha_\gamma^{(0)}(\omega) + \eta_{J m_J}\alpha_\gamma^{(2)}(\omega))\mathbf{E}_0^2 \end{aligned} \quad (6.38)$$

where $\alpha_\gamma^{(0)}$ and $\alpha_\gamma^{(2)}$ are the scalar and tensor components of the total polarizability $\alpha_{\gamma J m_J}(\omega)$, and $\eta_{J m_J}$ is:

$$\eta_{J m_J} = \begin{cases} \dfrac{3m_J^2 - J(J+1)}{J(2J-1)}, & \text{for } J \geq 1 \\ 0, & \text{otherwise} \end{cases}$$

6.4.4 Low-optical-intensity (weak field) regime

When the light field is negligible compared to the hyperfine splitting, the eigenstates of the system will be the $|F, m_F\rangle$ states instead of the $|J, I, m_J, m_I\rangle$ states. The analysis in section 6.4.1 may be followed to get results that are identical to Eqs. 6.32-6.36 except with each instance of J and m_J are replaced by F and m_F respectively. The new scalar and rank-2 tensor polarizabilities $\alpha^{(0)}(F;\omega)$ and $\alpha^{(2)}(F;\omega)$ are related to their J-based counterparts by [9]

$$\alpha^{(0)}(F;\omega) \approx \alpha^{(0)}(J;\omega) \tag{6.39}$$

and

$$\alpha^{(2)}(F;\omega) \approx \frac{3X(X-1) - 4F(F+1)J(J+1)}{(2F+3)(2F+2)(2J-1)} \alpha^{(2)}(J;\omega), \tag{6.40}$$

where

$$X := F(F+1) - I(I+1) + J(J+1). \tag{6.41}$$

6.5 Experiment

6.5.1 Procedure

The atoms are prepared in the MOT and optical lattice while the optical lattice is at low intensity. Before excitation, the optical intensity is ramped to a value about 20 times higher. The atoms are then two-photon excited into the $5D_{3/2}$ state; the drive pulses are below saturation intensity and have durations of about 10 μs for the 795nm and 200 ns for the 762nm. In a simplified picture, atoms become excited when they are located at or move through (because of thermal motion) positions where both lasers are resonant on the potential landscape. Multiple spectra are recorded in which the upper-transition laser is scanned while the lower-transition laser is fixed, for a set of lower-laser detunings. The ionization signal is collected on an MCP.

6.5.2 Frequency locking and scanning of excitation lasers

In this experiment, the excitation lasers must be locked and scanned over a wide range far from the field-free atomic resonance, and the detunings must be precisely known for an accurate measurement of the polarizability. Common methods for laser frequency control rely on using AOMs, which have comparatively small offsets and scanning ranges; scanning the grating or current of the laser, a method which suffers from low precision in the frequency; and/or using a reference cavity, which can be susceptible to frequency drifts caused by temperature fluctuations in its environment, and sometimes has too large of a spectral range to be useful. A PLL setup is much more involved to construct and to use, but allows large scanning ranges with high precision.

Without a frequency reference (preliminary data) For the first set of preliminary data we collected, we initially let the 795-nm laser frequency float, i.e. instead of locking it to anything. While the data visually appears promising, the significant

variance of times at which the scans were taken (especially for the scans with the biggest difference in 762-nm detuning) is such that the uncertainty in 795-nm drift is very large and precludes extracting polarizability values with reasonable uncertainty.

With Fabry-Pérot interferometer (FPI) references The FPI spectra of the 795-nm and 762-nm light may each be recorded together with the ion spectra in order to provide relative frequency references. The FPI is temperature-controlled to stabilize the resonance spectrum against temperature fluctuations. Small fluctuations remain; however. These were found to be within 1 MHz within the span of a couple of hours. This stability is expected to be sufficient for making a polarizability measurement with good uncertainty.

With PLL references Even better performance is offered by using the PLLs discussed in Chapter IV (layout shown in Fig. 4.2). In this scheme, the scans of the 795-nm and 762-nm excitation lasers are each phase-locked to an additional laser that is nearly the same wavelength and locked to an atomic reference (see Fig. 4.3). The frequency offsets between each pair are determined by an RF signal generator, whose frequency may be held constant or scanned. When locked, the beat note between the two lasers was found to be $<$10 Hz, which is far smaller than the absolute precision of the laser locked to the atomic reference (estimated to be $\sim$1 MHz). The scheme allows large, multi-GHz detunings (accommodating the expected maximum light shifts given in subsection 6.3.4) and with high absolute precision. It is planned to collect future data for the polarizability measurement using this method. Though the precision will still be limited by the reference laser to $\sim$1 MHz, using the PLLs will allow the detuning frequencies to be known on an absolute scale, to be controlled easily, and to be recorded automatically in the collected data.

6.5.3 Preliminary data

The initial dataset is shown in Fig. 6.2. The two main regions of ion signal come from transitions through either of the hyperfine levels of the ^{85}Rb $5P_{3/2}$ intermediate state ($F = 3$, left region; $F = 2$, right region). They correspond to each other with one shifted from the other by +362 MHz in 795-nm frequency and -362 MHz in the 762-nm frequency. At a fixed 795-nm frequency, the splitting between them is related to the hyperfine splitting and the polarizabilities of all of the states (Eq. 6.11). In the data, it is similar to the value we estimated earlier (230 MHz). The lengths of the lines reflect the distribution of atoms across different regions of lattice intensity. For a given hyperfine level of the intermediate state, the upper left signal corresponds to higher intensity regions. The lines become broader at higher intensities because the PI rate increases. In principle, the rate linewidth of increase can be used to determine the PI cross-section. The slope of the lines may be used to extract a value for the $5D_{3/2}$ polarizability using Eq. 6.7. In the preliminary data here, the uncertainties from the laser drifts are too wide to make the slope extraction useful (the slopes suggest a value around -600 with an uncertainty of around 30%). At the same time, it demonstrates potential for much better precision. By using frequency references and collecting similar data, we anticipate an uncertainty around $5 - 10\%$.

6.6 Outlook

The immediate next step for this experiment is to repeat the collection of data corresponding to Fig. 6.2 but while using one or more frequency references for the excitation lasers. Since acquiring the preliminary data, we have built two PLL setups (including the installation of two additional laser systems to use as references) for improved control of the excitation laser frequencies. We have tested and confirmed the ability to phase-lock each pair, and to scan the excitation lasers (the slave lasers)

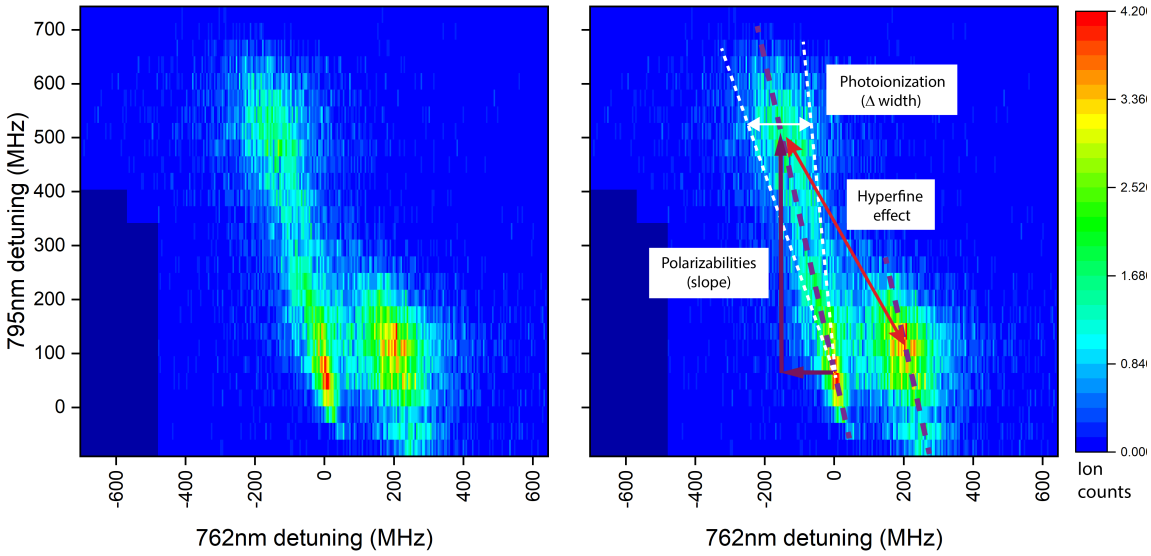

Figure 6.2: Ion counts from excitation of atoms to $5D_{3/2}$ while in the high-intensity optical-lattice dipole trap, as a function of the excitation laser detunings. The right side shows the same data but with the most important features annotated. The frequency detuning scales in the graph are not absolute; they are related to Δ_{795} and Δ_{795} by small offsets that are approximately fixed.

by changing the frequencies of the RF generators. With these developments, we expected that new data for a new measurement will be able to be collected in the near future.

On the theoretical side, a model should be developed for fitting the whole data set with polarizability and PI cross-section values. The simple relations between basic features in the experimental data and the PI rates and polarizabilities is useful to guide the experiment and to develop insights, but the real physical system has several layers of complexities that solicit more sophisticated models. The atoms are multi-level quantum-mechanical systems—with hundreds of levels, if the magnetic sublevels are included—and with coherent couplings by the excitation lasers. The excited states have many decay paths, and the $5D_{3/2}$ states may be irreversibly excited into the continuum by photoionization. Further, the atoms may move over the timescale of the pulse, which is complicated by the fact that they experience different dipole forces from the optical lattice depending on their internal state (and the $5P_J$- and $5D_{3/2}$-

states are repulsed from the light intensity). In principle, this scenario is treatable with Tullys surface hopping method [158, 159], which accounts for center-of-mass forces on vibrational wavepackets without requiring a full quantum treatment of the center-of-mass motion. Finally, the model should account for the distributions in atom location and thermal velocity, lattice intensity, and excitation beam intensities.

CHAPTER VII

Spectroscopy of Lattice-Mixed Rydberg States

"Here you are, a happy little atom. If you're in a standing wave, what do you see, moving around?"

– Paul Berman

7.1 Overview

This chapter describes the basis and design of an experiment to optically excite and spectroscopically observe "hydrogenic" Rydberg states mixed by a high-intensity optical lattice. I discuss how, in an optical lattice of comparable spacing, Rydberg atoms experience light shifts based on ponderomotive potentials instead of the typical dipole-interaction-based AC Stark shifts. Because the electron quiver motion corresponding to the ponderomotive interaction is many orders of magnitude faster than the timescale of the Rydberg atomic center-of-mass motion, the Rydberg atom experiences an adiabatic potential. In such a scenario, the optical lattice is referred to as a ponderomotive optical lattice (POL). At high-intensities, POLs mix the high-angular-momentum (also known as hydrogenic) states with themselves and with small portions of low-angular-momentum states. The lattice-mixed high-angular-momentum states, which were previously energetically degenerate within a given n-manifold, develop a rich structure and become accessible to excite from low-angular-momentum states.

The proposed experiment is to spectroscopically probe the lattice-mixed high-angular-momentum states. In order to inform the experimental design, I examine several design parameters and compare how they affect the quality of the conditions for observing the states. I describe the experimental setup and progress toward making the measurement.

7.2 Motivation

High-angular-momentum (high-ℓ) states of Rydberg atoms have attracted interest over the decades for several reasons. Their exceptionally long lifetimes often make them the candidate of choice for applications where long probe times are beneficial, such as in cavity quantum electrodynamics [160], quantum sensing [5, 6], and quantum simulations of spin systems [161]. Because of the absence of atomic core penetration by the Rydberg electron, they closely resemble the corresponding states of hydrogen. They deviate due to the long-range effect of the core polarizability [162] and thus may be used to sensitively probe it [162–164]. Additionally, high-ℓ-character states in a dense gas can form Rydberg molecules [28] of exotic types [32, 61, 76].

The production of high-ℓ states is not straightforward; in accordance with the optical dipole selection rule $\Delta\ell = \pm 1$, either i) many photons must be supplied for stepwise excitation, or ii) ℓ-mixing must be present. The former has been done, particularly for "aligned circular states," through combined optical and RF excitations and a time-varying electric field using the rapid adiabatic passage method [165, 166] or derivatives of it, and is also possible to do with specially-designed optical traps [167]. Aligned circular states are those with maximal ℓ and magnetic quantum number m, i.e. the states $|n, \ell = n-1, |m| = n-1\rangle$. These states have often been favored because they have been the easiest to produce with high-purity, which, for many applications, is a necessary condition to be useful. In the second case, ℓ-mixing collisions and recombination processes have explained the population of high-ℓ states after ini-

tial optical excitation to low-ℓ states [168–171] and have been exploited accordingly [172], though these processes result in a mixture of high-ℓ states as opposed to a pure state. In addition, ℓ-mixing induced by electric, magnetic, and/or RF fields during or following the optical excitation has allowed production of circular states with techniques such as the crossed-fields method [173, 174], as well as high-ℓ, low-m states [162, 175–180].

Purely optical mixing of Rydberg angular momenta has also been proposed by means of short, intense laser pulses. In one such proposal [181], it was suggested that the ultra-strong couplings between Rydberg states could allow the nondegenerate states to be ℓ-mixed by a non-resonant optical pulse of sufficient intensity, such that high-ℓ states could be directly photoexcited from a ground-state with only a single laser pulse and no external static fields. The proposal sparked a flurry of papers in which the nature of couplings between Rydberg states in strong optical fields was vigorously debated [182–197]. Theoretical progress eventually made clear that the electric dipole approximation fails for couplings between Rydberg states ($n > 10$) [193–197] and that a calculation using the full electric operator must be done in order to correctly evaluate angular momentum distributions. Nevertheless, such a calculation [194] indicated that the generated wave packet indeed consists of multiple angular momenta, and that there is some degree of preferential parity depending on the intensity and duration of the pulse (results which appear to be confirmed in recent experimental results [198]). The angular momentum distributions generated with short, intense laser pulses continues to be an area of active research, especially in their relation to excited-state population in strong field ionization through multiphoton processes and tunneling ionization [198–205], and for their use in quantum information processing [206].

Mixing of high- and low-angular-momentum states has also been studied in the context of accelerating excited-state decay [207] and is thus relevant for deexcitation

of antihydrogen for improved collection ability [208].

Here, we demonstrate a method that allows for all-optical excitation of states with high-ℓ character without the use of quasistatic field ramps. It is based on the ℓ-mixing induced by ponderomotive light shifts from a high-intensity, far-off-resonant optical lattice [209, 210]. A ponderomotive light shift originates from the kinetic energy imparted to the quasi-free Rydberg electron by the off-resonant optical field [209]. Inside an optical lattice, the effective light shift depends not on the field at the point location of the atomic center of mass, but on the intensity distribution in the whole spatial extent of the electron wavefunction, which, for Rydberg atoms, is typically of a comparable size to the lattice periodicity. At sufficiently high intensities, the variation of the optical field within the electron wavefunction induces ℓ-mixing, such that the hydrogenic manifold is optically accessible without additional fields and exhibits a rich structure with features reminiscent of rotor, vibrational, and Stark states. Because m is conserved during the lattice mixing (due to the cylindrical symmetry of the 1-D lattice), the excited states have low-m. This high-ℓ, low-m character is a property shared with the electronic wavefunctions of Rydberg molecular states, particularly for the high-ℓ class of molecules (e.g. "trilobite" molecules [28]) but also for the low-ℓ class. Rydberg molecules are a core part of this work and are discussed in detail in Chapter V.

Because the method requires only optical excitations, the excitation region may in principle be in the range of microns, which would allow single-site addressability and wave packet engineering. Alternative methods relying on microwave and ramped fields, however, require RF antennas, magnetic field coils, and/or electrodes. Use of these leads to an excitation volume in the range of cubic centimeters or more and therefore prohibits site selectivity.

The method presented here is in contrast to the previously discussed scenario of optical ℓ-mixing (see several paragraphs before), primarily because the ℓ-mixings

have different origins. In the present case, it arises from the spatial variation of ponderomotive potential within the electron wavefunction. The mixing is induced by cw laser light that is far from any atomic resonance and whose intensity ($\sim 10^7$ W/cm^2) is lower than those of the other optical ℓ-mixing schemes, in most cases by several orders of magnitude. Furthermore, as opposed to generating a dynamical wave packet or a distribution of states, selective excitation to a single stationary eigenstate is possible.

7.3 Ponderomotive light shifts in optical lattices

The light-shift of a PEC of a Rydberg atom in an optical lattice is fundamentally different than a conventional light shift of an atomic ground or low-lying excited state. The latter is due to a field-induced dipole-moment arising from state-couplings that are (typically) in the frequency range of the optical field, i.e. the $\mathbf{A} \cdot \mathbf{p}$ term in the minimal coupling Hamiltonian of the electron:

$$H = \frac{[\mathbf{p} + e\mathbf{A}(\mathbf{r}, t)]^2}{2m_e}, \tag{7.1}$$

where $\mathbf{p}$ is the electron momentum, m_e is the electron mass, and $\mathbf{A}(\mathbf{r}, t)$ is the vector potential of the field. In the case of a Rydberg atom, transitions to nearby Rydberg states are strong but very far from optical field frequencies, and for the frequency chosen here of $c/1064$nm, the transition strengths to the states nearest resonance are extremely weak. Thus, these do not contribute significantly to the light shift. Instead, the shift is predominantly from the ponderomotive potential of the Rydberg electron, which results from the often-neglected A^2 term. The quasi-free electron is driven by the oscillating electric field (quiver motion), and the resulting time-averaged kinetic energy of the electron is equivalent to a change in the potential energy of the Rydberg atom. Treating the electron quiver motion as a static time-averaged

potential is appropriate because the timescale of the quiver motion ($\sim 10^{15}$ Hz) is orders of magnitude faster than that of the Kepler frequency ($\sim 10^{11}$ Hz for $n \sim 40$), which is the fastest orbital motion of the electron about the atomic core. The intensity gradient of the optical lattice exerts a force on the Rydberg electron, and the ionic core of the atom experiences the force mediated by its tenuous bond to the electron.

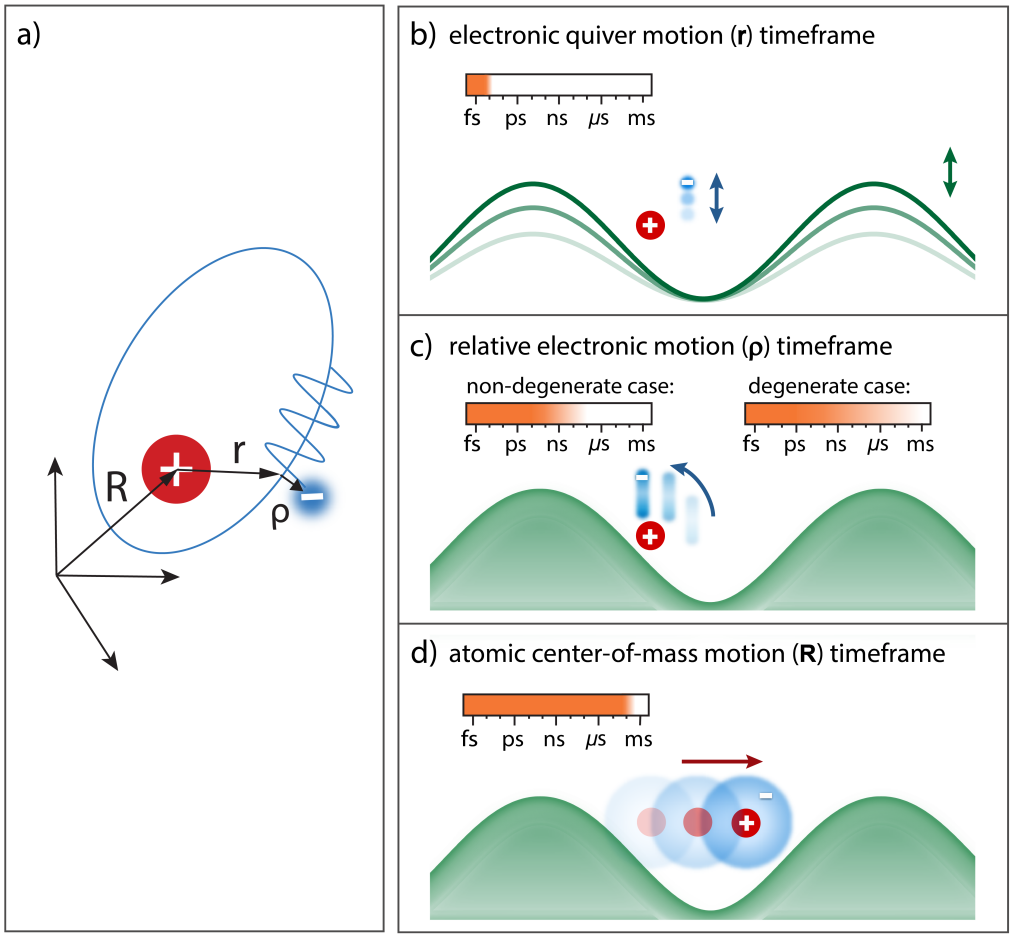

Figure 7.1: (a) Three coordinates of motion, adapted from Ref. [209]. (b)-(d) Illustrations of the timescales of each of the three types of motion. Within the timescale of each motion, other motions of vastly different timescales appear static; if slower, their positions appear fixed, and if faster, they appear time-averaged.

Besides the electronic quiver motion and motion relative to the atom, a third type of motion is at play, which is that of the atomic center-of-mass. The three types of motion are represented by three coordinates, ρ, $\mathbf{r}$, and $\mathbf{R}$, respectively (Fig. 7.1a).

The quiver motion (Fig. 7.1b) and motion relative to the atomic core (Fig. 7.1c) may always be separated from each other, and the atomic center-of-mass motion (Fig. 7.1d) may sometimes be treated separately from the others, as will be discussed in the following.

7.3.1 Nondegenerate case of ponderomotive shifts

We consider two particular cases of ponderomotive shifts of Rydberg atoms. In the simpler case, the perturbation from the external field is sufficiently small compared to the energy difference between the considered state and states of other angular momenta. This is true, for example, for Rydberg Rb atoms with $\ell < 3$ and ponderomotive shifts of tens of MHz, because the $\ell < 3$ quantum defects δ have non-integer parts that are large and well-separated from each other ($\delta_s = 3.13$, $\delta_p = 2.65$, and $\delta_d = 1.34$). The slowest frequencies of the electronic motion about the atom, the precession frequencies, are orders of magnitude faster than the center-of-mass atomic motion. This allows the Born-Oppenheimer approximation to be applied, which is that the electronic motion and the nuclear motion can be treated separately.

For low-ℓ Rydberg atoms with low-enough n to be small compared to the lattice period, nondegenerate first-order perturbation theory may be applied. The perturbative shifts in the atom's adiabatic energy levels are simply equal to the ponderomotive energy, $V_P = e^2|\mathbf{E}|^2/(4m_e\omega^2)$. For moderate- to large-sized Rydberg atoms, the optical field varies substantially within the Rydberg electron wavefunction and a spatial average must be taken to find the adiabatic lattice potential at the point-like location of the atom,

$$V_{ad}(\mathbf{R}) = \int d^3r V_P(\mathbf{r}+\mathbf{R})\ |\psi_0(\mathbf{r})|^2, \tag{7.2}$$

where $\mathbf{R}$ is the atomic center-of-mass coordinate, $\mathbf{r}$ is the relative coordinate of the

Rydberg electron, $V_P(\mathbf{r}+\mathbf{R})$ is the free-electron ponderomotive potential, and $\psi_0(\mathbf{r})$ is the unperturbed Rydberg electronic wavefunction.

The transition between the regime where the atom's adiabatic potential energy levels follow the shape of the lattice intensity, to the regime where they are modified according to a spatial average weighted by the electronic wavefunction, is shown by example in Fig. 7.2(a)-(c). Adiabatic potential energy levels are shown for $D_{5/2}$ states with effective principal quantum numbers $n^* \approx 20, 40$ and 60 in a $\lambda = 1064$nm optical lattice. For increasing Rydberg atom sizes (diameter $\sim 4n^{*2}$), the adiabatic potentials become flatter and show dependence on the m_j value (which is conserved because of the azimuthal symmetry of the lattice potential). For $n^* \approx 60$, more than one lattice spacing ($\lambda/2$) is spanned by the Rydberg wavefunction, and the potential becomes inverted for some m_j-states. The low-m_j state wavefunctions are elongated along the z-axis, meaning that the spatial averaging in Eq. 7.2 is more widespread. As n increases, their corresponding potentials flatten and invert earlier than higher m_j states. In contrast, the high-m_j state wavefunctions are donut-shaped with comparatively short spread along the z-axis, so their adiabatic potentials retain the shape of the lattice potential up to much higher values of n. Similar trends are seen in adiabatic potentials for the degenerate case [Fig. 7.2(d)-(f)], which is discussed in the next section.

7.3.2 Degenerate case of ponderomotive shifts

In the second case, which is when i) the perturbation is large with respect to the energy separation between a low-ℓ state and the high-ℓ states and ii) the Rydberg atom diameter is on the scale of the lattice periodicity, mixing of high-ℓ and low-ℓ states occurs. The adiabatic lattice potential,

$$V_{ad}(\mathbf{R}) = \int d^3r V_P(\mathbf{r}+\mathbf{R})\ |\psi(\mathbf{r})|^2, \tag{7.3}$$

has the same appearance as Eq. 7.2, but there is a critical difference: the electron wavefunction $\psi(\mathbf{r})$ may no longer be approximated as the unperturbed wavefunction $\psi_0(\mathbf{r})$. Thus, the integral may not be immediately evaluated because $\psi(\mathbf{r})$ is not known. Instead, finding the potential energy curves and wavefunctions requires rediagonalization of the electronic Hamiltonian, including the atomic fine structure. The Hamiltonian in atomic units is:

$$H = \frac{p^2}{2} - \frac{1}{r} + V_c(r) + V_{LS} + V_P(z + z_0) \tag{7.4}$$

where $V_c(r)$ is a short-range core potential, V_{LS} is the fine structure, z is the z-coordinate of the electron, z_0 is the z-coordinate of the atomic center-of-mass, the axis of the one-dimensional lattice is oriented along $\hat{\mathbf{z}}$, and it is assumed that the lattice potential varies slowly in the transverse direction.

The ponderomotive potential of the lattice is a sinusoidal standing wave that may be expanded in a Taylor series of $z = r\cos\theta$ about $z = 0$, that is,

$$V_P(z + z_0) = \frac{1}{2}V_0(1 + \cos(2k(z + z_0))) = \frac{1}{2}V_0 \sum_{p=0}^{\infty} K_p(2kr\cos\theta)^p, \tag{7.5}$$

where V_0 is the free electron ponderomotive potential $V_0 = e^2E_0^2/(m_e\omega^2)$ for the single-beam electric field E_0, and K_p are Taylor coefficients given by [210, 211]

$$K_p = \frac{1}{p!}\begin{cases} (-1)^{p/2}\cos(2kz_0) + \delta_{p,0}, & p \text{ even} \\ (-1)^{(p+1)/2}\sin(2kz_0), & p \text{ odd.} \end{cases} \tag{7.6}$$

In general, there are nonzero matrix elements for a wide range of $|n, \ell, j, m_j\rangle \leftrightarrow |n', \ell', j', m_j\rangle$ couplings. In practice, due to the $(2kr)^p$ factor in Eq. 7.5, the number of terms that matter depend on the size of the atom relative to the lattice period.

The angular matrix elements from the $cos^p\theta$ factors depend on ℓ, j and m_j, and have selection rules that depend on p.

Diagonalization of the electronic Hamiltonian with the additional lattice potential (Eq. 7.4) leads to the hydrogenic states mixing with each other and also, for strong enough lattice potentials, with low-ℓ states. The presence of low-ℓ character in the hydrogenic states allows the usually dipole-forbidden excitation from low-ℓ states.

The adiabatic potentials of several hydrogenic manifolds and the transition strengths from $5P_{3/2}$ are shown in Fig. 7.2(d)-(f). The shape of the hydrogenic manifold does not significantly depend on V_0 because the levels are already degenerate; it is very similar for $V_0 = 0.05 - 5$ GHz (not shown) and the depth of the pattern merely scales with V_P. More significant is the fact that mixing with low-ℓ states is present for lattice depths in the GHz range because the gaps between the hydrogenic manifold and the nearest low-ℓ states are of that range (see headline of Fig. 7.2). In frames (d)-(f), The transition strengths are proportional to the area of the red circles, multiplied by a scaling factor γ_{scale} that varies by frame. In this example, where the excitations are out of the $5P_{3/2}$ state, the excitation strength depends on the amount of S- and D-character mixed into the Rydberg states. The rapidly increasing strength of the mixing with n, which is reflected in γ_{scale}, is due to multiple factors: the atomic size ($4n^2$) growing to be comparable with lattice period ($\lambda/2$), the energy gaps between the hydrogenic manifold and the closest low-ℓ states decreasing, and stronger intrashell coupling among states in the same hydrogenic manifold.

7.3.3 Effective electric and magnetic fields

Further insights into the structure of the lattice-mixed adiabatic potentials may be gained by considering their similarities with Rydberg states in effective electric and magnetic fields. We consider the case when the Rydberg wavefunction spread along the lattice direction $\hat{\mathbf{z}}$, which depends on both n and m_j, is sufficiently *small*

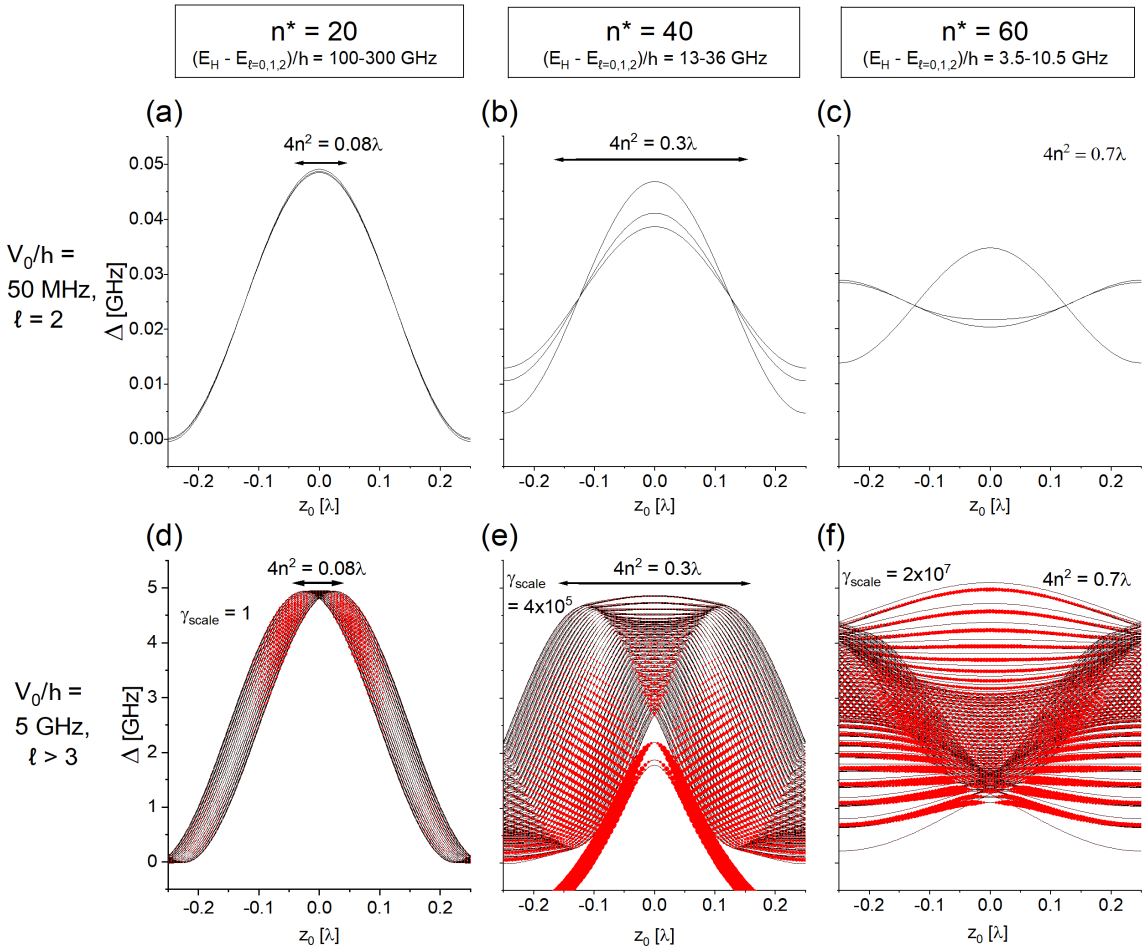

Figure 7.2: Examples of adiabatic potentials for nondegenerate and degenerate cases in a $\lambda = 1064$ nm lattice for $n^* \approx 20, 40$, and 60. (a)-(c): For $V_0/h = 50$ MHz, the $n^*D_{5/2}$ states have no ℓ-mixing. The adiabatic potentials are proportional to the optical lattice intensity for $n^* \approx 20$ and become flatter for $n^* \approx 40$ and 60 due to the spatial averaging in Eq. 7.2. (d)-(f): At $V_0/h = 5$ GHz, the n^*H hydrogenic manifolds acquire low-ℓ character, allowing them to have nonzero transition strengths from $5P_{3/2}$. The transition strengths are proportional to the area of the red circles, multiplied by the displayed scaling factor γ_{scale}.

compared to the lattice period. The effective electric and magnetic fields are discussed in detail in Ref. [210], whose main findings are summarized here.

The gradient of the optical potential exerts a force on the Rydberg atom as does an electric field on an electron. The maxima and minima of a slope gradient occur at the inflection points. For the potential of Eq. 7.5, the inflection points are at $z_0 = \lambda/8 \pm N\lambda/4$, for which the gradient values are $\pm V_0 k$. This corresponds to

"effective electric fields" of

$$E_{\text{eff}}\ (\lambda/8 \pm N\lambda/2) = +\frac{V_0 k}{e}, \tag{7.7}$$

$$\text{and}\ \ E_{\text{eff}}\ (3\lambda/8 \pm N\lambda/2) = -\frac{V_0 k}{e}. \tag{7.8}$$

For example, a lattice depth of $V_0/h = 2$ GHz has a corresponding field of $E_{\text{eff}} = 490$ mV/cm at the lattice inflection points. For perspective, when using optical spectroscopy, the sensitivity level of Rydberg states to electric fields is about 1-10 mV/cm. When the effective-electric-field comparison is valid, the splitting between adjacent adiabatic potentials is equivalent to those of the effective electric field, which is $3nE_{\text{eff}}$ (a.u.). In Ref. [210], a numerical comparison of the splittings showed that, for $\lambda = 1064$nm, the comparison is approximately valid for $n \lesssim 37$ for $m_j = 2.5$, and likely valid for n up to ~ 250 for $m_j = n - 2.5$.

The concept of the effective magnetic field is most useful at the lattice maxima and minima because the potentials are approximately quadratic. The diamagnetic interaction term of a Rydberg atom in a magnetic field is $(e^2B^2/8m_e)\ r^2 \sin^2\theta$. The lattice potential of Eq. (7.5) in the second-order Taylor expansion, at the lattice minima and maxima, is

$$V = \frac{V_0}{2} \pm \left(\frac{V_0}{2} + V_0 k^2 r^2 \sin^2\theta - V_0 k^2 r^2 \right), \tag{7.9}$$

where the positive and negative signs apply for the lattice maxima and minima, respectively. Because of the term proportional to $r^2 \sin^2\theta$, the lattice potentials have a resemblance to the energy levels induced by a magnetic field. Equating the $r^2 \sin^2\theta$ terms directly leads to an expression for an "effective magnetic field" experienced by

the Rydberg atom at the lattice maxima,

$$B_{\text{eff}}\ (z_0 = 0, \pm\lambda/2, \pm\lambda, \ldots) = \frac{2\sqrt{2}E_0}{c}, \tag{7.10}$$

where E_0 is electric field amplitude of a single laser beam forming the POL. The B_{eff} for $V_0/h = 1$ GHz and $\lambda = 1064$nm is 0.081 teslas. A Rydberg atom in a strong magnetic field has a combination of vibrator-like states, where the energy level spacing is constant, and rotor-like states, where the energy level spacing progressively increases. At the lattice minima, the sign of the potential is flipped, leading to a reverse ordering of vibrational and rotational states. This explains why the same qualitative behavior can be seen in POLs at the lattice maxima and minima.

Near the lattice maxima and minima, one may also include the presence of an effective linearly-varying electric field. The force, which is the derivative of the potential in Eq. 7.5, is $-V_0 k\ \sin(2kz_0))$. In the small-angle approximation, it is $-2V_0k^2z_0$, so that $E_{\text{eff}} = -2V_0k^2z_0/e$. In comparison to Rydberg states in actual parallel electric and magnetic fields [212], the structure of the lattice potentials at the antinodes is remarkably similar.

7.4 Experiment

7.4.1 Experimental considerations for lattice-mixed-Rydberg-state spectroscopy

The goal of this experiment is to obtain the first conclusive spectra of atoms excited to Rydberg hydrogenic states in an optical lattice with ponderomotive interaction. This requires sufficient excitation strengths, energy separations between adjacent states, and detection rates, warranting careful consideration of related experimental design parameters.

7.4.1.1 Excitation scheme

In principle, a number of different optical excitation paths to hydrogenic states are possible. We define the launch state as the penultimate state of the stepwise multiphoton transition to the hydrogenic states. The specific angular momentum of the launch state is perhaps the most significant parameter influencing the strength of the transition to the high-angular-momentum state. The transition strengths largely depend on the $\ell' = \ell \pm 1$ character of the field-mixed hydrogenic states, which depends on the number of steps between ℓ' and $\sim$4 (the angular momentum at which the Rydberg states become approximately degenerate), and the proximity in energy of each of the $n'\ell''$ Rydberg states for $\ell'' = \ell', \ell' + 1, \ldots$ $\sim$4 to the nearest hydrogenic manifold (or equivalently, the non-integer part of their quantum defects), as well as the $n\ell \rightarrow n'\ell'$ dipole matrix elements. In rubidium, both the amount of $\ell \pm 1$ character contained in the mixed hydrogenic states and the dipole matrix elements tend to increase for higher values of ℓ.

The significant dependence of transition strength on ℓ may be seen by example. Let us consider the transition strengths to the $n' = 50$ hydrogenic manifold for four different launch states in Rb: $5S_{1/2}$, $5P_{3/2}$, $5D_{3/2}$, and $4F_{5/2}$. Examples of excitation schemes with these launch states are shown in Fig. 7.3. The adiabatic potentials, which are independent of launch state, are shown in Fig. 7.4 for a free-electron ponderomotive shift of 1 GHz. The transition strengths of the adiabatic potentials, which vary by launch state, are represented by colored circles. The relative transition strengths are assigned colors on a logarithmic scale and, within a given panel, are proportional to the areas of the colored circles. Among the panels, the scale of the circle areas is varied by the factor γ_{scale} in order to keep them in a visible range. The scaling factors (and similarly, the colors) give indications of how the transition strengths from different launch states compare overall. For example, the $5P_{3/2}$ launch state transition strengths are about 500 times larger than those for $5S_{1/2}$, and those

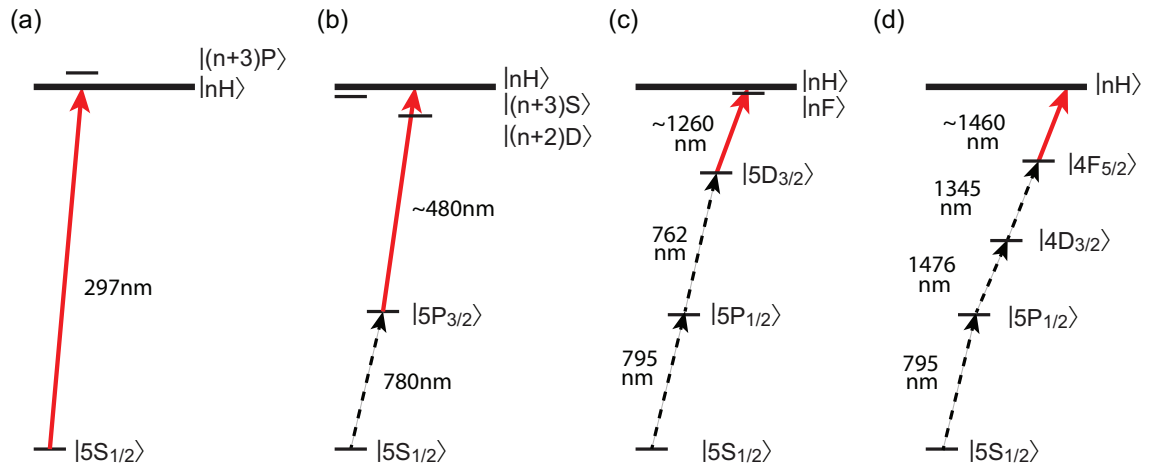

Figure 7.3: Examples of excitation schemes with launch states of $5S_{1/2}$, $5P_{3/2}$, $5D_{3/2}$, and $4F_{5/2}$. The red arrows show the transitions from the 4 choices of launch states to the same Rydberg hydrogenic manifold. How the excited launch states are populated is not significant; the dashed arrows show possible paths. Also shown are the Rydberg levels that have $\ell' = \ell \pm 1$ and are energetically close to the hydrogenic manifold.

of the $5D_{3/2}$ are about 10^4 times larger than those of $5P_{3/2}$.

The increase in excitation rates with increasing ℓ for low ℓ can be understood by considering the energy proximity of the ℓ' Rydberg states for which $\ell' = \ell \pm 1$, as illustrated in Fig. 7.3. For example, a D- launch state couples to the Rydberg F-states, which mix strongly with the hydrogenic manifold because they are energetically close (having a non-integer part of the quantum defect of only 0.016) compared to the states coupled to a P launch state, namely S- and D-states, whose respective non-integer parts of the quantum defects are 0.13 and 0.35 and have higher-order couplings to the hydrogenic manifold. To explain what is meant by higher-order coupling, an S-launch state would require third- or fourth-order coupling ($S \to P \to D \to F \to nH$). Additionally, the first three couplings have a large energy denominator because of the quantum defects. Both the high-order couplings and the large energy separations serve to make the excitation strength from an S-launch state much smaller than using, for a contrasting example, F-launch states.

Initial probing of the hydrogenic states with the same deep optical lattice setup was attempted previously (to this work) with two-photon excitation to the Rydberg states,

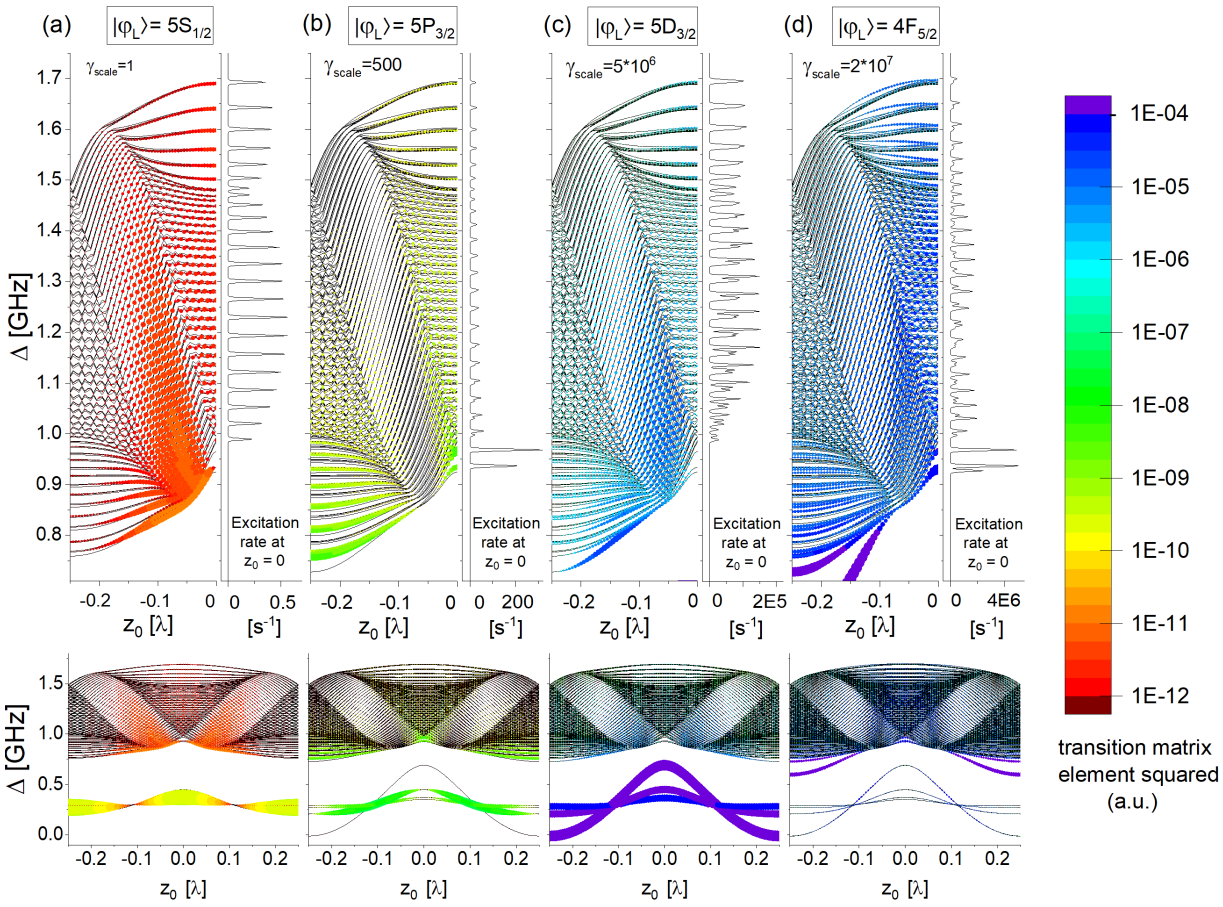

Figure 7.4: Adiabatic potentials, transition strengths, and excitation spectra for the $n = 50$ hydrogenic manifold with 1 GHz free-electron POL depth, shown for four different launch states. Each vertical strip (a)-(d) corresponds to a different launch state. Within each strip, the lowest panel shows the adiabatic potentials and transition strengths over large scale that extends low enough below the hydrogenic manifold to include the $50F$-states. The upper left panel shows a close-up version of the same plot. The spectrum in the upper right panel show the relative excitation rates for atoms located at the maximum lattice intensity ($z_0 = 0$) for a fixed intensity and pulse length of the excitation laser. The circles in the potential plots are colored by transition strength (transition matrix element squared) according to the scale on the right. The areas of the colored circles are proportional to the transition strengths and, in each panel, are scaled by the factor γ_{scale} displayed near the top of each strip.

using $5P_{3/2}$ as the launch state [33]. The signal-to-noise ratio was too low to reveal much structure or to conclusively indicate hydrogenic state detection. As exemplified in Fig. 7.4, D- launch states are expected to have extremely high excitation rates to the lattice-mixed hydrogenic manifold, compared to P- launch states. This motivated our implementation of an excitation scheme with $5D$ as the launch state, specifically $5S_{1/2} \rightarrow 5P_{1/2} \rightarrow 5D_{3/2} \rightarrow nH$. We expect to be able to achieve sufficient signal with this scheme with the significantly increased excitation rates predicted by the calculations.

A caveat of using the $5D_{3/2}$ state in the excitation scheme is that it has a large photoionization cross-section at the wavelengths of the dipole trap (1064nm) as well as the red excitation beams (795nm and 762nm). To avoid photoionization before the Rydberg excitation, the hydrogenic states must be excited off-resonantly through the $5D_{3/2}$ state with a detuning (i.e. from the light-shifted resonance) somewhat greater than the $5D_{3/2}$ photoionization rate at the chosen lattice intensity. The expected photoionization broadening and natural linewidth of the state are about 0.5 GHz and 0.6 MHz. The anticipated factor of improvement from $5P_{3/2}$ to $5D_{3/2}$ is thus significantly reduced from 10,000. In principle, it's possible to make cases where photoionization of intermediate state does not occur, e.g. by changing the launch state or the lattice wavelength. One can also devise schemes where atoms are excited at the lattice minimum and therefore the PI rates are low.

The $5S \rightarrow 5P$ and $5P \rightarrow 5D$ transitions have substantial differential light shifts (hundreds of MHz or more) in the presence of the strong 1064-nm field. In the radial direction, they vary according to the Gaussian profile of the lattice trap.

We choose $5P_{1/2}$ as the first intermediate state instead of $5P_{3/2}$ because of its simpler hyperfine structure and absence of tensor polarizability. Tensor polarizability would cause an intensity-dependent splitting of the hyperfine levels, which would complicate the spectra. We note that the tensor polarizability of the $5D_{3/2}$ is very

small and matters less anyway because of the earlier choice to use a significant detuning from that state. On-resonance excitation of a $5P$ state is not prohibited by photoionization effects because, among other reasons, the $5P$ levels are too low in energy to be photoionized by 1064nm light. Furthermore, because of the $5S \rightarrow 5P$ differential light shift, on-resonance excitation critically provides selectivity of atoms in spatial regions whose local 1064-nm intensities are within a narrow range, instead of the wider range corresponding to the spatial distribution of the thermal atomic ensemble. Exciting only atoms within a narrow intensity range yields cleaner, more well-defined spectra.

The 3-step excitation scheme and relevant hyperfine structure is shown in Fig. 7.5. Implementing the 3-step excitation involved setting up new lasers for each of the three wavelengths of the new transitions (795nm, 762nm, and 1260nm). To facilitate better frequency control and precision, a second pair of 795nm and 762nm lasers was installed. The excitation lasers are phase-locked to them while the each of the second pair is locked to an atomic frequency reference. The phase-locking is explained in much greater detail in Section 6.5.2.

7.4.1.2 Principal quantum number of hydrogenic-state manifold

The choice of principal quantum number n influences several factors relevant to the desired qualities of the lattice-mixed-Rydberg-state spectra. On one hand, lower values of n correspond to greater transition dipole moments for the field-free transitions from low-lying to Rydberg states, and the POL-shifted hydrogenic manifolds for $n \leq 50$ exhibit a simpler pattern because the Rydberg electronic wavefunction spans less than a single lattice period. On the other hand, at higher n values, the energy gap decreases between the hydrogenic manifold and the low-angular-momentum Rydberg states, leading to stronger mixing between them and additionally to generally wider separations between sequential hydrogenic states within a single manifold.

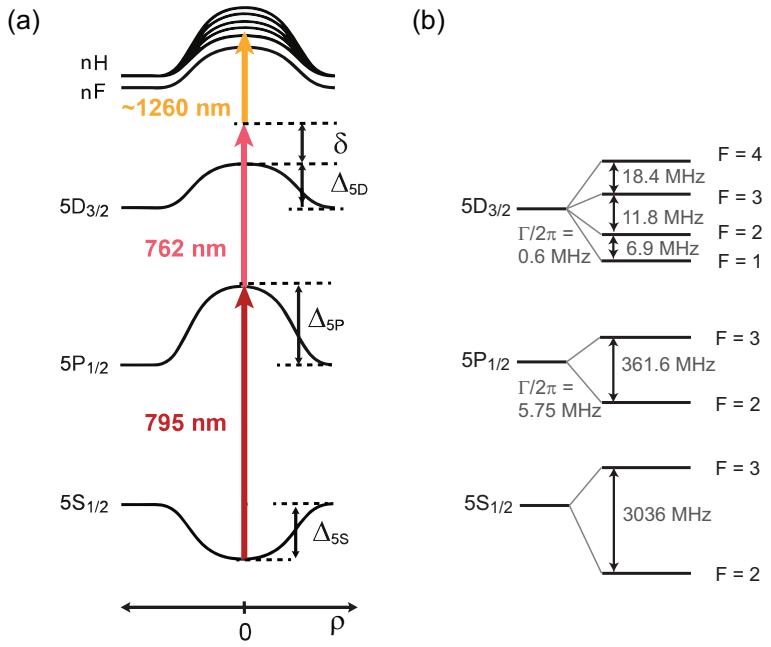

Figure 7.5: (a) Excitation scheme, with AC Stark shifts dependent on the radial position of the atom. (b) Hyperfine structure and natural linewidths of the lower energy levels.

To appraise the n-scaling of the transition rates, several factors must be considered. The dipole matrix element from the launch state to an unperturbed Rydberg state scales as $n^{-3/2}$. The strength of the hydrogenic mixing scales as the intrashell coupling and as the inverse of the energy gap between the hydrogenic manifold and the nearby Rydberg state that is dipole-allowed from the launch state (in the present case, nF). In the electric dipole approximation (EDA), the intrashell couplings scale as $n\sqrt{n^2-\ell^2} = n^{1.5-2}$; however, the EDA is known to overestimate the true intrashell couplings in a strong optical field [193, 194]. The inverse energy gap scales as n^3. Summing all of the scaling factors and doubling the result gives a rough estimate for the transition-rate scaling of n^{6-7}. Not accounted for is the fact that the lattice potential gradient changes within the Rydberg wavefunction and also varies significantly with n. Numerical calculations yield an estimate of n^{4-11} depending on n, launch state, and potential depth. In any case, in the current experimental regime, the effect on the transition strength due to the increase in hydrogenic state mixing with n is found to

outweigh that due to the diminishing dipole moments of transitions from the launch state.

7.4.1.3 Lattice intensity

High lattice intensity creates stronger mixing of the hydrogenic manifold with proximal states, and also increases the separation between sequential mixed hydrogenic states such that they are more easily resolvable. At the same time, it broadens the photoionization linewidth of the $5D_{3/2}$ state, necessitating increasing detuning from the state and thus a loss in signal for fixed excitation power. At high lattice intensities and high n, the manifolds of different principal quantum numbers may become coupled, complicating the physics. Further, it is unclear how much the power may be increased before the optical cavity incurs permanent damage from burning, and this risk must be considered when increasing the lattice intensity.

7.4.1.4 Method of detection of lattice-mixed Rydberg hydrogenic states

For Rydberg state detection, we ionize the Rydberg states and subsequently collect the ions with a micro-channel plate (MCP). At least two ionization methods are potentially available in the current experimental setup: ionization by application of a strong static electric field, or photoionization using the high-intensity 1064nm light. Concerning the first method, it is feasible to apply a static electric field up to about 135 V/cm in the existing setup, corresponding to 370 V applied at the electrode with highest voltage. This field strength can ionize Rydberg states of any ℓ and m for effective principal quantum numbers $n^* \geq 56$ (low-ℓ and/or $m = 0$ states may be ionized with $n^* \geq 40$). Photoionization should happen for any n^* in the Rydberg regime. The rates depend on the angular momenta and also are proportional to the local intensity of the light at the atomic center-of-mass location. The relative rates are shown in Fig. 7.6.

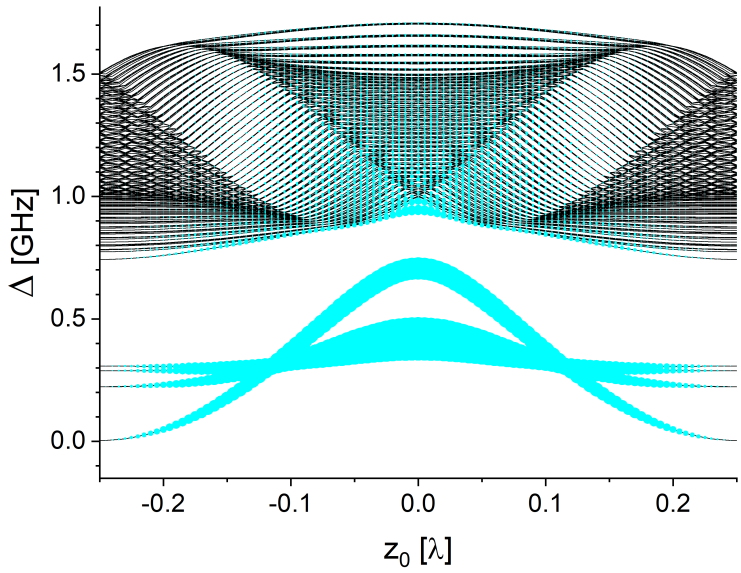

Figure 7.6: Photoionization rates for the $n = 50$ hydrogenic manifold in a $\lambda = 1064$ nm lattice with $V_0/h = 1$ GHz, represented by the areas of the blue circles. Here, the rates for the highest-energy hydrogenic states are about 5 mHz, while for the F-states they are about 100 mHz. The rates are calculated based on methods developed in Ref. [213].

At the high estimated intensity in our experiment, the photoionization rates for high-ℓ states are so slow (1-10 mHz) that only about 10^{-7} of the populated Rydberg states would be photoionized. We conclude that for our initial trial of probing hydrogenic states, we should use the field ionization method and choose n^* in the range of $56 - 70$, where field ionization is possible and also the Rydberg electronic wavefunction is not considerably larger than the lattice spacing (it is twice the lattice spacing at $n = 70$).

7.4.1.5 Configurations of excitation beams

The 1260nm laser is sent into the chamber propagating perpendicularly to the lattice axis. A cylindrical lens (f=150mm) is used to focus the beam in the horizontal dimension such that the beam has a highly-elliptical shape and overlaps better with the lattice-trapped atoms. The 795nm and 762nm beams are combined using a dichroic, after which they pass through a fiber. They are then combined with the

orthogonally-polarized 1064nm beam using a polarizing beam splitter. The beam configuration at the location of the lattice-trapped atoms is illustrated in Fig. 7.7.

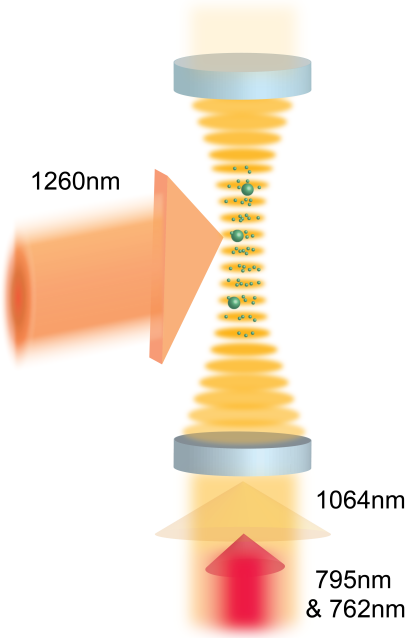

Figure 7.7: Excitation beam configuration relative to lattice-trapped atoms in the 1064-nm optical cavity. The 1260-nm beam is focused in the horizontal direction to a roughly 40μm for improved overlap with the atoms collected in the lattice.

7.4.2 Experiment preparation and timing sequence

The 795-nm and 762-nm lasers may be locked and frequency controlled using the PLLs described in Chapter IV and also used for the polarizability experiment in Chapter VI. First, the 795-nm laser frequency is calibrated to the lattice-shifted transition. When frequency is be scanned while the transmitted light though the atoms trapped in the lattice is monitored, the signal exhibits two dips in absorption for each of the $5P_{1/2}$ $F = 1, 2$ levels (see, for example, Fig. 4.5). A narrow peak corresponds to absorption from atoms outside the lattice, and a broad, blue-shifted peak results from interaction with atoms trapped in the lattice. The breadth in the blue-shifted peak arises from the distribution of atoms at different locations (and thus experiencing different lattice light intensities) within the lattice potential.

The 762-nm laser frequency is set to be a few hundred MHz blue-detuned from the light-shifted $5P_{1/2} \rightarrow 5D_{3/2}$ transition in order to suppress photoionization from $5D_{3/2}$ by the 1064-nm lattice. Next, the 1260-nm laser is scanned using the fiber EOM near the predicted region of the hydrogenic state manifold. The excitation of atoms outside the lattice region to the nearby F-state can be used as a reference line. As in the polarizability experiment, the lattice loading is be accomplished through adiabatic compression, i.e. loading the lattice at low intensity and then adiabatically ramping up the power so as to retain most of the atoms in the trap [33]. The excitation pulses are applied while the lattice is at high intensity. The experimental progress is ongoing. The scanning of the 1260nm beam and the detection of nF-states have already been demonstrated.

CHAPTER VIII

Conclusion and Outlook

"That's the good news; there are still plenty of things to figure out."

– Paul Berman

In this thesis, I have presented several experiments to probe unusual Rydberg states and states in the presence of a deep optical lattice. The near-concentric cavity used in all of the experiments enables not only ground-state-atom trapping but also the generation of very high optical intensities, which induce AC Stark shifts in low-lying atomic states and ponderomotive shifts in Rydberg atomic states.

In the first experiment, I have investigated binding energies of long-range Rydberg molecules. Binding energy measurements test low-energy electron-atom scattering interactions, on which the novel binding mechanism for this molecule is based, and which are relevant for fundamental processes in chemical physics. The two spins of the ground-state- and Rydberg-atom valence electrons, which are already coupled to other angular momenta within their respective atoms, become coupled with each other by the molecular scattering interaction, forming a chain of four angular momenta linked by three couplings. In this work, the differences in molecular binding energy spectra from varying each of the couplings have been directly observed. An initial effort has been made to model the data and extract electron-atom scattering information.

While the model is moderately successful, it has significant inherent shortcomings and also does not fully agree with the measurements. The measurements thus motivate a new model and may serve in the development of one.

Several new avenues of experimental research to explore, as discussed in Chapter V, include the molecular resonances in the multi-GHz-deep wells of the same molecular potentials, which are likely to show evidence of the J-splitting of the triplet p-wave scattering, and dynamical processes of long-range Rydberg molecules. Regarding the latter, for example, photoassociation beyond the frozen gas model could be explored by numerically simulating the photoassociation with long laser pulses in warm atom clouds.

The latter two experiments, which are yet in progress, aim to examine the response of atoms in high optical intensities at 1064nm. Measurements of the width of the $5D_{3/2}$ state and its shift relative to lower levels will allow estimations of its dynamic polarizability and photoionization cross-section, which will provide tests atomic structure theory and has applications for atomic clocks [109], magnetometers [110], and atomic interferometers [111, 112]. Rydberg atoms in the same high-intensity optical lattice are predicted [210] to exhibit a new type of potential energy curves that mix a large number of Rydberg states and are yet to be observed.

We have completed the construction of the setup for these two experiments. A significant achievement was the installation of new excitation lasers and the implementation of systems to precisely control their frequencies. We also have performed basic theoretical analyses to inform the experimental design parameters and our expectations of the anticipated data. These efforts have provided a solid foundation for the next step, which is to perform the experiments and collect data. For the polarizability measurement, initial data has already been obtained; though it lacks usability, it demonstrates that the experiment is feasible with our setup.

The near-concentric-cavity optical lattice [108] offers many possibilities for new

experiments beyond the ones outlined here. Potential topics include Rydberg-atom-ion molecules (e.g. detection, binding energy spectroscopy, study of vibrational wavepacket dynamics) [214], Rydberg EIT effects, and light propagation guided through elongated atomic clouds [33]. One could also make use of the optical cavity's ability to sustain higher-order modes, which would trap multiple parallel, elongated clouds of cold atoms. These would allow interesting experiments using Rydberg polaritons and the Rydberg blockade effect [33].

APPENDICES

APPENDIX A

Additional Data for Long-Range Rydberg Molecules

"We make profits the old-fashioned way."

– Paul Berman

The initial data of the molecular spectra corresponding to those in Fig. 5.3 is shown here in Fig. A.1. Because of highly favorable experimental conditions, it has a much better signal-to-noise ratio. However, frequency uncertainty of the detuning was several MHz due to mechanical imperfections in the system used to scan the upper-transition laser frequency, and thus did not allow conclusive determination of whether some differences among the 8 cases were indeed present. In Fig. 5.3, the data is recorded using a new scanning system with improved precision, though the high quality of the initial experimental conditions was not able to be matched.

The high signal-to-noise in Fig. A.1 reveals broad resonances that are not clearly resolvable in Fig. 5.3—for example, the three peaks in the detuning region of -300 to -200 MHz in the left bottom panel. The better resolution of the broad peaks allows some of them to be used in the linewidth analysis of subsection 5.5.6 such that a wider diversity of resonances may be considered.

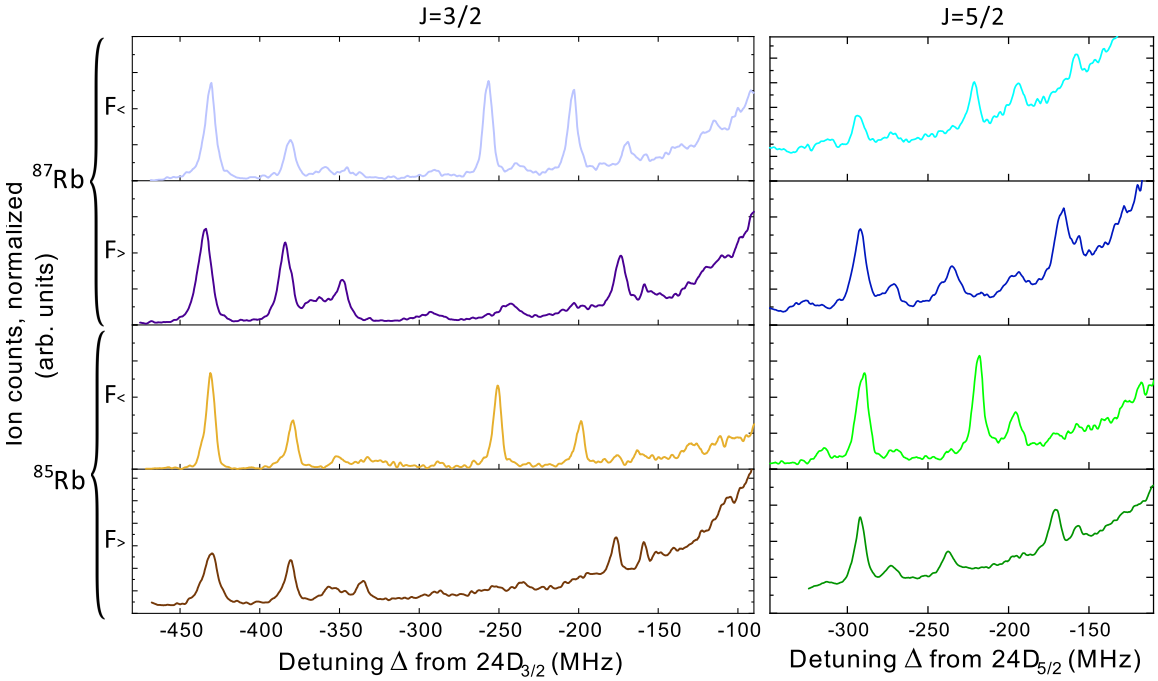

Figure A.1: Detected ions vs. detuning relative to the $24D_J$ atomic state, for the same eight (I_2, F_2, J)-combinations as Fig. 5.3.

APPENDIX B

Calibration and Uncertainty Analysis for 960-nm Laser Frequency Scanning

"Would you rather use 200 equations, or 3 equations? It depends on your personality."

– Paul Berman

One objective in the long-range Rydberg molecule experiment was to measure the binding energies with the best precision that was reasonably possible. Higher precision makes the measurements more useful for refining the underlying theory and also discernment of smaller differences among the spectra for different cases of angular momentum coupling. For instance, in the end, the model used to fit the binding energy resonances was able to fit them within 3.8 MHz. The redesign and analysis described here ultimately reduced the detuning uncertainties from 4 MHz to 1 MHz or less, which means that the data is much better-suited for improving the models. As a second example, the leftmost lines in the molecular resonance data (see Figs. 5.3 and A.1) vary between the those of different isotopes by $\sim$3 MHz and, probably, between the those of different ground-state hyperfine orientations by $\sim$1 MHz. The frequency uncertainty of the initial data was small enough to hint

at differences but too large to conclusively verify them; whereas the latter frequency uncertainty confirmed the existence of the 3 MHz differences.

Achieving better precision required careful work, both to improve and to characterize the uncertainty of the upper-transition-laser detuning frequency. I initially determined the frequency uncertainty to be roughly 4 MHz. I reduced this to 1 MHz maximum (for the most deeply-bound resonances that were observed) by redesigning the mechanical control of the scanning system, developing a model for the frequency shift, and calibrating the system experimentally.

The upper-transition laser is locked and scanned using a pressure-tun ed Fabry-Pérot interferometer (FPI) as a frequency reference, shown in Fig. B.1 and based on the design presented in Ref. [215]. A portion of the 960-nm light from the laser is split off to use for locking, while the rest is frequency-doubled to 480nm for exciting Rb atoms from the $5P_{3/2}$ state to a Rydberg state (for excitation scheme, refer to Fig. 5.1). The FPI cavity mirrors are glued on either end of a hollow rod made of ultralow-expansion (ULE) material. The rod sits inside in a sealed chamber with windows allowing the laser light to pass through the FPI cavity. The ULE rod has a hole in its side which allows the air pressure between the cavity mirrors to be at equilibrium with the surrounding air in the chamber. A compressible bellows connected to one end of the chamber allows control of the air pressure inside.

The linear motion of the bellows was originally controlled by a stepper motor rotating a micrometer screw. I found that the rotational motion of the screw produced periodic oscillations in the ratio of linear displacement per step with an amplitude on the order of ten microns, changing the FPI resonances by a few MHz. I replaced the micrometer screw and stepper motor system with a motorized linear stage (Newport model VP-25XA), which is controlled in steps of 0.1μm and reportedly has a linear positioning accuracy of 1.0μm or less. The model and data collection for calibrating the change in resonance frequency to change in step number of the linear stage is

described in the following sections.

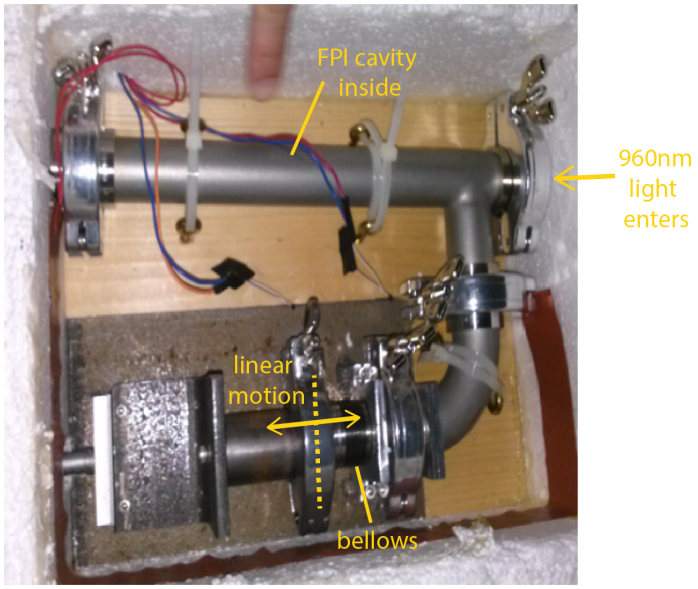

Figure B.1: Picture of the chamber containing the FPI cavity. The 960-nm light passes horizontally through the segment at the top of the picture. The segment at the bottom left is pushed with motorized control (not shown) and linearly compresses or extends the bellows shown in the bottom center. The setup is contained in a styrofoam box so that the ambient temperature of the FPI can be stabilized.

B.1 Theory of pressure-tuned FPI-based frequency scanning mechanism

During a spectroscopic scan, the 960-nm laser is locked to some peak of a FPI. The FPI has a series of resonances that are equally spaced in frequency, such that a resonance has a frequency $f = q\nu$, where q is a positive integer (on the order of 10^5 in the present case) and ν is the free spectral range (FSR) of the FPI. When the laser is locked to a FPI resonance, the q will remain fixed, and the frequency will change proportionally to the FSR, so that $f = f_0\nu/\nu_0$, where f_0 and ν_0 are the original frequency and FSR respectively.

In general for the FSR of a FPI, $\nu = c/(2n\ell)$, where c is the speed of light, n is the index of refraction of the material through which the light is traveling, and ℓ is the

distance in steps between the two cavity mirrors of the FPI. In the scanning system used here, ℓ remains fixed, but n changes due to the change of air pressure inside the cavity. Thus, we have

$$f = \frac{f_0 n_0}{n}, \tag{B.1}$$

where n and n_0 are the new and original indices of refraction of the air, respectively.

The index of refraction of air may be approximated as

$$n_{\text{air}} = 1 + 0.000293 \left(\frac{PT}{P_0 T_0} \right) = 1 + \alpha \left(\frac{PT}{P_0 T_0} \right) \tag{B.2}$$

where P and T are the pressure and temperature, P_0 and T_0 are standard atmospheric pressure and room temperature, and we set $\alpha = 0.000293$.

Changing the length of the bellows changes the pressure inside the sealed chamber. We use the gas law $PV/T = P_0 V_0 / T_0$, and note that the entire volume of the air may be considered as a cylinder with equivalent volume and a constant cross-sectional area times a length L, as long as the cross-sectional area is constant in the region where the length is changed. Assuming no variations in temperature, we obtain the relation $P/P_0 = L_0/L$, which leads to

$$n_{\text{air}} = 1 + \alpha \left(\frac{L_0}{L} \right). \tag{B.3}$$

Combining Eq. B.3 and Eq. B.1 to find the relationship between two frequencies f_1 and f_2 gives

$$f_2 = f_1 \left(\frac{n_1}{n_2} \right) = f_1 \left(\frac{1 + \alpha \left(\frac{L_0}{L_1} \right)}{1 + \alpha \left(\frac{L_0}{L_2} \right)} \right). \tag{B.4}$$

The difference in these two frequencies is

$$\Delta f_{960} = f_2 - f_1 = f_1 \left(\frac{1 + \alpha \left(\frac{L_0}{L_1} \right)}{1 + \alpha \left(\frac{L_0}{L_2} \right)} - 1 \right). \tag{B.5}$$

Using $\Delta L = L_2 - L_1$, Eq. B.5 may be rearranged to get

$$\Delta f_{960} = f_1 \left(\frac{\alpha L_0 \, \Delta L}{L_1 (L_1 + \Delta L + \alpha L_0)} \right) \tag{B.6}$$

To control the length of the bellows, we use a linear stage that moves in steps of fixed size. The length of the equivalent cylinder containing the volume of air is $L = D(x + B)$, where D is a length of a single step (fixed), x is the step number at which the linear stage is set, and B is a constant accounting for the arbitrary length offset of the linear stage. Eq. B.6 becomes

$$\begin{aligned} \Delta f_{960} &= f_1 \left(\frac{\left(\frac{\alpha L_0}{D} \right) \Delta x}{(x_1 + B) \left(x_1 + B + \Delta x + \left(\frac{\alpha L_0}{D} \right) \right)} \right) \\ &= \frac{f_1 \; A \; \Delta x}{(x_1 + B) \, (x_1 + B + \Delta x + A)}, \end{aligned} \tag{B.7}$$

where the constant A is defined as $\alpha L_0 / D$. The values of A and B are constant and correlate to physical properties of the system, so they may be roughly estimated or experimentally determined for better precision, as described in the subsequent section. The absolute frequency of the 960nm light f_1 is presumably known to reasonable accuracy. Thus, this equation relates the change in frequency of the light that is locked to the FPI to the change in step size of the linear stage (Δx), for a given starting position of the linear stage x_1.

The change in 480-nm frequency is double the change in 960-nm frequency,

$$\boxed{\Delta f_{480} = \frac{2 f_1 \; A \; \Delta x}{(x_1 + B) \, (x_1 + B + \Delta x + A)}.} \tag{B.8}$$

Several significant conclusions about the effective calibration factor $\Delta f_{480} / \Delta x$ follow from Eq. B.8 that previously had not been immediately obvious. One is that, not

only is the effective calibration factor not constant across the span of the scanning range (i.e., not constant with respect to the scan starting position x_1)—which had been noticed earlier—but it is also not linear (although it appears so in the relevant region), and it depends on Δx in addition to x_1. Secondly, the effective calibration factor also depends on the frequency of the 960-nm light. This frequency may change on the order of one percent when probing Rydberg states of different principal quantum numbers, which could lead to errors of several MHz (scanning over hundreds of MHz) if it is not accounted for.

B.2 Experimental calibration

The calibration process for the Newport linear stage was done in the following way. I did spectroscopy of a Rydberg atomic line ($26S$) by scanning the linear stage of the FPI to which the 960-nm light is locked. The 780-nm (lower-transition) light travels through an AOM in a double-pass configuration. I take advantage of an initially unintended feature of the light, which is that a small fraction includes other frequency-orders that are shifted by 0, 1, or 3 times the driving RF instead of 2 times. The multi-frequency light results in the appearance of copies of the primary line that are shifted from it by multiples of the RF (in the present case, about 79.8 MHz). The presence of multiple lines at relatively small and well-known frequency spacings provides data that is convenient for calibrating the linear stage. I recorded spectra by locking the 960-nm laser at different frequencies relative to the stage position such that (Δf_{480}, Δx, x_1) triads could be found for a wide range of x_1 values.

B.2.1 Data collection

Part of the data I collected for calibration consists of groups of 6 scans that were taken at 10 different regions of the linear stage's range. Three satellite lines and one main line were observed for each of the scans (see Fig. B.2), but only the main line and the two satellite lines to the blue-detuned side of it were used. The satellite line

to the left was ultimately neglected because its calibration showed a systematic shift in comparison with the others, which we believe to be due to the greater Rydberg-molecule background counts to red side of the main line than to the blue side.

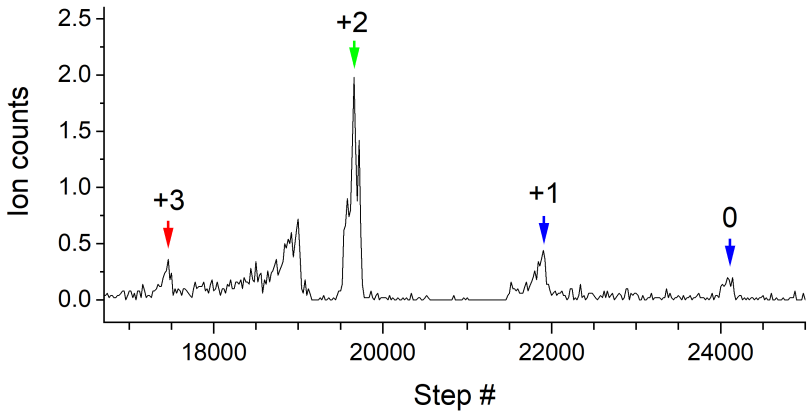

Figure B.2: An example of a 960-nm-laser frequency scan probing the $26S$ state and used for calibration. The tallest peak (indicated by +2) is from light that is frequency-shifted twice due to its double passage through the AOM. Three small components of light are from other AOM orders and produce copies of the atomic line that are offset from main line by well-known frequencies. These peaks are labeled according to their AOM order. In the step number region from 19000 to 21500, the power is dramatically reduced to protect the MCP. As a consequence, there is an extra peak at step #19000, and only a small contrast in ion counts between the main line and the satellite lines.

The line centers were fitted (using OriginPro8.5), and the distance between sequential lines was calculated for each scan—three lines used gives a total of two distances Δx per scan. For each of the 10 regions, the first distance and second distance were each averaged over the 6 scans, resulting in $2 \times 10 = 20$ data points, each containing (Δf_{480}, Δx, x_1) values.

Additional data points were generated by comparing the 4 spectral lines of single scans to the 4 spectral lines of other scans in which the 780-nm frequency was locked to different peaks of a separate FPI. In other words—instead of finding the step sizes for peak separations $+2 \to +1$ and $+1 \to 0$, and comparing it with the AOM driving frequency—the step sizes for peak separations $-1 \to -1$, $0 \to 0$, $+1 \to +1$, $+2 \to +2$ were compared with the FSR frequency. Four sets were able to be used,

which together contribute $4 \times 4 = 16$ data points.

B.2.2 Fitting data to extract model parameters

I used MATLAB to fit the 36 three-dimensional data points to model. I used $f_1 \simeq 309.752$ THz for fitting the data from the $26S$ lines to create the calibration curve. Later, when making use of the calibration curve to calculate the detuning frequency for the $24D$ molecules, I used $f_1 \simeq 309.692$ THz. Note that these numbers correspond to the *non-doubled* frequencies of the laser. By error, I used Eq. B.7 to fit the data points instead of Eq. B.8, which means that the fitted parameters I obtained, A^* and B^*, were not the same as the true A and B that are based on Eq. B.8. However, comparing Eqs. B.7 and B.8, it is most likely that A is very close to A^* and B is similar to $\sqrt{2}B^*$. I obtained $A^* = 1556.104$ steps and $B^* = 3643921$ steps, so I estimate:

$$\boxed{\begin{array}{c} A \approx 1556 \text{ steps} \\ B \approx 5.15 \times 10^6 \text{ steps} \end{array}}$$

Note that the A and B given here correspond to the convention of using x_1 as the lower-frequency/red-detuned step number, and x_2 (for $\Delta x = x_2 - x_1$) is the higher-frequency step number; the same convention should be followed when using these parameters to find a frequency detuning. Also, I note that my using A^*, B^* and Eq. B.7 for calculating the molecular resonances does not invalidate the values and uncertainties I extracted. While it's possible that the calibration uncertainties may have grown by a small amount, their values are already incorporated in the uncertainty estimations.

Using the motorized-stage specifications of $D = 0.1\mu$m per step and the previously given definition $A = \alpha L_0/D$, we may calculate $L_0 = 0.53\text{m} = 20.9$ inches. This value would be the length of a cylinder with the same cross-section of the bellows and the same volume of air as the chamber. Considering the visual size of the chamber, this is

a very reasonable result. We may also estimate that $L_0 \approx BD$, which should be the case if $x_1 = 0$ when the internal pressure is the same as atmospheric pressure. The above estimation of B gives $BD \approx 0.515$m. The closeness of these results suggests that a rough calibration could be achieved fairly well with only a single-parameter fit.

B.3 Uncertainty analysis of molecular binding energies

Once the calibration curve and fitting parameters had been established, they could then be used for finding the molecular binding energies. The molecular binding energies are subject to three types of uncertainties:

1. The first is given by the calibration uncertainty of the 480-nm laser scan, which was found when fitting the calibration data to the model, and reflects only uncertainty in the fitting parameters. The calibration and corresponding uncertainty are a function of two variables (Δx and x_1). In Fig. B.3, I show an example of Δf_{480} and its uncertainty, for a fixed Δx. Across the range of possible x_1 values, the uncertainty is about 0.8 MHz. For one of the most deeply bound resonances observed (i.e. the "A_1" resonance of the ^{87}Rb $24D_{3/2} + 5S_{1/2}$ $F_<$ at 439.1 MHz), the uncertainty was found to be 0.93 MHz.

2. A second type is due to the statistical uncertainty of the Gaussian peak fits to the molecular and atomic lines. In a typical case, the uncertainty in line separation amounts to about 0.23 MHz.

3. Another uncertainty, which is systematic, arises from line pulling due to MOT intensity fluctuations while scanning across the spectroscopic lines. This is found by subtracting (in quadrature) the fit uncertainties from the standard deviation in line separations among multiple scans of the same peaks, and dividing by the square root of the number of scans. This uncertainty is found to

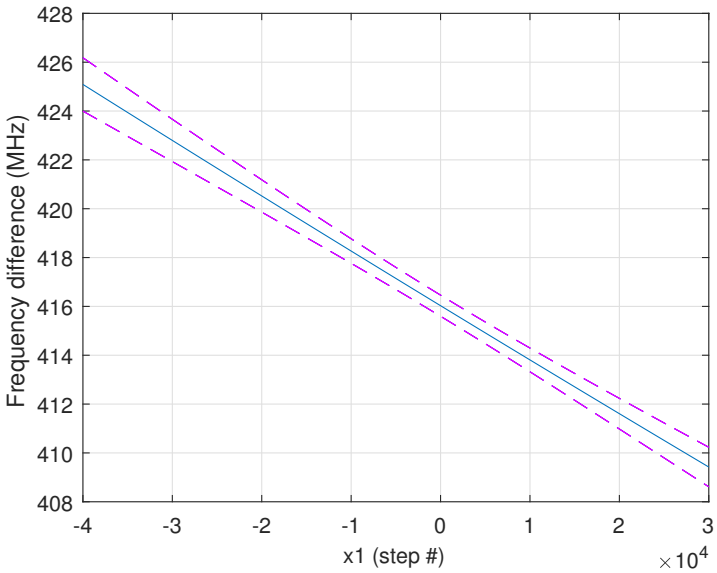

Figure B.3: Sample calibration curve (solid blue) for determining Δf_{480} from a fixed Δx of 11500 steps, and 95% confidence intervals (dashed red).

be 0.15 MHz.

The three uncertainties are summed in quadrature for each molecular line to find the net uncertainty of its detuning from the atomic line. For the aforementioned "A_1" resonance, the total uncertainty was found to be 0.97 MHz. the differences in the resonances corresponding to 0.22% of the binding energy. For less-deeply bound states, the absolute uncertainty drops because the scanning range is shorter; at very small separation distances the first source approaches zero such the net uncertainty becomes 0.27 MHz.

As a result of using the linear stage and the calibration method described here, all of the measured molecular binding energies had 1.0 MHz uncertainty or less. This facilitated pushing the accuracy limits of the model we used and allowed us to conclusively observe isotope-dependent differences in triplet-state binding energies.

BIBLIOGRAPHY

BIBLIOGRAPHY

[1] D Vrinceanu, R Onofrio, and HR Sadeghpour. Angular momentum changing transitions in proton-rydberg hydrogen atom collisions. *The Astrophysical Journal*, 747(1):56, 2012.

[2] Johann Jakob Balmer. Notiz über die spectrallinien des wasserstoffs. *Annalen der physik*, 261(5):80–87, 1885.

[3] JR Rydberg. On the structure of the line-spectra of the chemical elements. *The London, Edinburgh, and Dublin Philosophical Magazine and Journal of Science*, 29(179):331–337, 1890.

[4] Thomas F. Gallagher. *Rydberg Atoms (Cambridge Monographs on Atomic, Molecular and Chemical Physics)*. Cambridge University Press, 1994. ISBN 0521385318.

[5] Adrien Facon, Eva-Katharina Dietsche, Dorian Grosso, Serge Haroche, Jean-Michel Raimond, Michel Brune, and Sébastien Gleyzes. A sensitive electrometer based on a rydberg atom in a schrödinger-cat state. *Nature*, 535(7611):262–265, 2016.

[6] EK Dietsche, A Larrouy, S Haroche, JM Raimond, Michel Brune, and S Gleyzes. High-sensitivity magnetometry with a single atom in a superposition of two circular rydberg states. *Nature Physics*, 15(4):326–329, 2019.

[7] Christopher J Foot et al. *Atomic physics*, volume 7. Oxford University Press, 2005.

[8] Vasant Natarajan. *Modern Atomic Physics*. CRC Press, 2015.

[9] Daniel A Steck. Quantum and atom optics, 2007.

[10] DA Kondratev, IL Beigman, and LA Vainshtein. Polarizability of alkali atoms. *Bulletin of the Lebedev Physics Institute*, 35(12):355–362, 2008.

[11] Maxwell D Gregoire, Nathan Brooks, Raisa Trubko, and Alexander D Cronin. Analysis of polarizability measurements made with atom interferometry. *Atoms*, 4(3):21, 2016.

[12] Martin M Boyd. High precision spectroscopy of strontium in an optical lattice: Towards a new standard for frequency and time, 2007.

[13] Jeffrey D Carter, O Cherry, and JDD Martin. Electric-field sensing near the surface microstructure of an atom chip using cold rydberg atoms. *Physical Review A*, 86(5):053401, 2012.

[14] JA Sedlacek, A Schwettmann, Harald Kübler, and JP Shaffer. Atom-based vector microwave electrometry using rubidium rydberg atoms in a vapor cell. *Physical Review Letters*, 111(6):063001, 2013.

[15] Christopher L Holloway, Joshua A Gordon, Steven Jefferts, Andrew Schwarzkopf, David A Anderson, Stephanie A Miller, Nithiwadee Thaicharoen, and Georg Raithel. Broadband rydberg atom-based electric-field probe for si-traceable, self-calibrated measurements. *IEEE Transactions on Antennas and Propagation*, 62(12):6169–6182, 2014.

[16] Christopher G Wade, Nikola Šibalić, Natalia R de Melo, Jorge M Kondo, Charles S Adams, and Kevin J Weatherill. Real-time near-field terahertz imaging with atomic optical fluorescence. *Nature Photonics*, 11(1):40–43, 2017.

[17] David H Meyer, Zachary A Castillo, Kevin C Cox, and Paul D Kunz. Assessment of rydberg atoms for wideband electric field sensing. *Journal of Physics B: Atomic, Molecular and Optical Physics*, 53(3):034001, 2020.

[18] Charles S Adams, Jonathan D Pritchard, and James P Shaffer. Rydberg atom quantum technologies. *Journal of Physics B: Atomic, Molecular and Optical Physics*, 53(1):012002, 2019.

[19] David H Meyer, Kevin C Cox, Fredrik K Fatemi, and Paul D Kunz. Digital communication with rydberg atoms and amplitude-modulated microwave fields. *Applied Physics Letters*, 112(21):211108, 2018.

[20] David Alexander Anderson, Rachel Elizabeth Sapiro, and Georg Raithel. An atomic receiver for am and fm radio communication. *IEEE Transactions on Antennas and Propagation*, 2020.

[21] David A Anderson, Rachel E Sapiro, and Georg Raithel. Rydberg atoms for radio-frequency communications and sensing: atomic receivers for pulsed rf field and phase detection. *IEEE Aerospace and Electronic Systems Magazine*, 35(4): 48–56, 2020.

[22] Mark Saffman, Thad G Walker, and Klaus Mølmer. Quantum information with rydberg atoms. *Reviews of modern physics*, 82(3):2313, 2010.

[23] Mark Saffman. Quantum computing with atomic qubits and rydberg interactions: progress and challenges. *Journal of Physics B: Atomic, Molecular and Optical Physics*, 49(20):202001, 2016.

[24] Wenhui Li, I Mourachko, MW Noel, and TF Gallagher. Millimeter-wave spectroscopy of cold rb rydberg atoms in a magneto-optical trap: Quantum defects of the ns, np, and nd series. *Physical Review A*, 67(5):052502, 2003.

[25] Jianing Han, Yasir Jamil, DVL Norum, Paul J Tanner, and TF Gallagher. Rb n f quantum defects from millimeter-wave spectroscopy of cold rb 85 rydberg atoms. *Physical Review A*, 74(5):054502, 2006.

[26] G Günter, M Robert-de Saint-Vincent, H Schempp, CS Hofmann, S Whitlock, and M Weidemüller. Interaction enhanced imaging of individual rydberg atoms in dense gases. *Physical review letters*, 108(1):013002, 2012.

[27] Florian Karlewski, Markus Mack, Jens Grimmel, Nóra Sándor, and József Fortágh. State-selective all-optical detection of rydberg atoms. *Physical Review A*, 91(4):043422, 2015.

[28] Chris H. Greene, A. S. Dickinson, and H. R. Sadeghpour. Creation of polar and nonpolar ultra-long-range rydberg molecules. *Phys. Rev. Lett.*, 85:2458–2461, Sep 2000.

[29] Vera Bendkowsky, Björn Butscher, Johannes Nipper, James P. Shaffer, Robert Löw, and Tilman Pfau. Observation of ultralong-range rydberg molecules. *Nature*, 458(7241):1005–1008, apr 2009.

[30] Christian Fey, Frederic Hummel, and Peter Schmelcher. Ultralong-range rydberg molecules. *Molecular Physics*, 118(2):e1679401, 2020.

[31] D. Booth, S. T. Rittenhouse, J. Yang, H. R. Sadeghpour, and J. P. Shaffer. Production of trilobite rydberg molecule dimers with kilo-debye permanent electric dipole moments. *Science*, 348(6230):99–102, 2015. ISSN 0036-8075.

[32] Thomas Niederprüm, Oliver Thomas, Tanita Eichert, Carsten Lippe, Jesús Pérez-Ríos, Chris H Greene, and Herwig Ott. Observation of pendular butterfly rydberg molecules. *Nature communications*, 7(1):1–6, 2016.

[33] Yun-Jhih Chen. *Atom Trapping and Spectroscopy in Cavity-Generated Optical Potentials*. PhD thesis, University of Michigan, 2015.

[34] Bindiya Arora and BK Sahoo. State-insensitive trapping of rb atoms: linearly versus circularly polarized light. *Physical Review A*, 86(3):033416, 2012.

[35] Garrett D. Cole, Wei Zhang, Bryce J. Bjork, David Follman, Paula Heu, Christoph Deutsch, Lindsay Sonderhouse, John Robinson, Chris Franz, Alexei Alexandrovski, et al. High-performance near-and mid-infrared crystalline coatings. *Optica*, 3(6):647–656, 2016.

[36] S. J. M. Kuppens, K. L. Corwin, K. W. Miller, TE Chupp, and CE Wieman. Loading an optical dipole trap. *Physical review A*, 62(1):013406, 2000.

[37] Yun-Jhih Chen, Luís Felipe Gonçalves, and Georg Raithel. Measurement of rb 5 p 3/2 scalar and tensor polarizabilities in a 1064-nm light field. *Physical Review A*, 92(6):060501, 2015.

[38] N Thaicharoen, KR Moore, DA Anderson, RC Powel, E Peterson, and G Raithel. Electromagnetically induced transparency, absorption, and microwave-field sensing in a rb vapor cell with a three-color all-infrared laser system. *Physical Review A*, 100(6):063427, 2019.

[39] F Nez, F Biraben, R_ Felder, and Y Millerioux. Optical frequency determination of the hyperfine components of the 5s12-5d32 two-photon transitions in rubidium. *Optics communications*, 102(5-6):432–438, 1993.

[40] Adela Marian, Matthew C Stowe, John R Lawall, Daniel Felinto, and Jun Ye. United time-frequency spectroscopy for dynamics and global structure. *Science*, 306(5704):2063–2068, 2004.

[41] A Banerjee, D Das, and V Natarajan. Absolute frequency measurements of the d1 lines in 39k, 85rb, and 87rb with 0.1 ppb uncertainty. *EPL (Europhysics Letters)*, 65(2):172, 2004.

[42] Daniel A Steck. Rubidium 85 d line data, 2001.

[43] Daniel A Steck. Rubidium 87 d line data, 2001.

[44] Michel Chéret, Luc Barbier, Werner Lindinger, and Robert Deloche. Penning and associative ionisation of highly excited rubidium atoms. *Journal of Physics B: Atomic and Molecular Physics*, 15(19):3463, 1982.

[45] L Barbier, MT Djerad, and M Chéret. Collisional ion-pair formation in an excited alkali-metal vapor. *Physical Review A*, 34(4):2710, 1986.

[46] L Barbier and M Cheret. Experimental study of penning and hornbeck-molnar ionisation of rubidium atoms excited in a high s or d level (5d⩽nl⩽11s). *J. Phys. B*, 20(6):1229–1248, mar 1987.

[47] Joseph Ladislas Wiza et al. Microchannel plate detectors. *Nucl. Instrum. Methods*, 162(1-3):587–601, 1979.

[48] A Schwarzkopf, DA Anderson, N Thaicharoen, and G Raithel. Spatial correlations between rydberg atoms in an optical dipole trap. *Physical Review A*, 88 (6):061406, 2013.

[49] TF Gallagher, LM Humphrey, WE Cooke, RM Hill, and SA Edelstein. Field ionization of highly excited states of sodium. *Physical Review A*, 16(3):1098, 1977.

[50] Jamie L MacLennan, Yun-Jhih Chen, and Georg Raithel. Deeply bound (24 d j+ 5 s 1/2) rb 87 and rb 85 molecules for eight spin couplings. *Physical Review A*, 99(3):033407, 2019.

[51] I I Fabrikant. Interaction of rydberg atoms and thermal electrons with k, rb and cs atoms. *Journal of Physics B: Atomic and Molecular Physics*, 19(10): 1527–1540, may 1986.

[52] C. Bahrim and U. Thumm. Low-lying $^3P^o$ and $^3S^e$ states of rb^-, cs^-, and fr^-. *Phys. Rev. A*, 61:022722, Jan 2000.

[53] C Bahrim, U Thumm, and I I Fabrikant. 3 s e and 1 s e scattering lengths for e - + rb, cs and fr collisions. *Journal of Physics B: Atomic, Molecular and Optical Physics*, 34(6):L195, 2001.

[54] C. Bahrim, U. Thumm, and I. I. Fabrikant. Negative-ion resonances in cross sections for slow-electron˘heavy-alkali-metal-atom scattering. *Phys. Rev. A*, 63: 042710, Mar 2001.

[55] B. J. DeSalvo, J. A. Aman, F. B. Dunning, T. C. Killian, H. R. Sadeghpour, S. Yoshida, and J. Burgdörfer. Ultra-long-range rydberg molecules in a divalent atomic system. *Phys. Rev. A*, 92:031403, Sep 2015.

[56] Heiner Saßmannshausen, Frédéric Merkt, and Johannes Deiglmayr. Experimental characterization of singlet scattering channels in long-range rydberg molecules. *Phys. Rev. Lett.*, 114:133201, Mar 2015.

[57] V. Bendkowsky, B. Butscher, J. Nipper, J. B. Balewski, J. P. Shaffer, R. Löw, T. Pfau, W. Li, J. Stanojevic, T. Pohl, and J. M. Rost. Rydberg trimers and excited dimers bound by internal quantum reflection. *Physical Review Letters*, 105(16), oct 2010.

[58] D. A. Anderson, S. A. Miller, and G. Raithel. Photoassociation of long-range *nd* rydberg molecules. *Phys. Rev. Lett.*, 112:163201, Apr 2014.

[59] F. Böttcher, A. Gaj, K. M. Westphal, M. Schlagmüller, K. S. Kleinbach, R. Löw, T. Cubel Liebisch, T. Pfau, and S. Hofferberth. Observation of mixed singlet-triplet rb_2 rydberg molecules. *Phys. Rev. A*, 93:032512, Mar 2016.

[60] A. T. Krupp, A. Gaj, J. B. Balewski, P. Ilzhöfer, S. Hofferberth, R. Löw, T. Pfau, M. Kurz, and P. Schmelcher. Alignment of *d*-state rydberg molecules. *Phys. Rev. Lett.*, 112:143008, Apr 2014.

[61] J. Tallant, S. T. Rittenhouse, D. Booth, H. R. Sadeghpour, and J. P. Shaffer. Observation of blueshifted ultralong-range cs_2 rydberg molecules. *Phys. Rev. Lett.*, 109:173202, Oct 2012.

[62] M. A. Bellos, R. Carollo, J. Banerjee, E. E. Eyler, P. L. Gould, and W. C. Stwalley. Excitation of weakly bound molecules to trilobitelike rydberg states. *Phys. Rev. Lett.*, 111:053001, Jul 2013.

[63] Thomas Niederprüm, Oliver Thomas, Tanita Eichert, and Herwig Ott. Rydberg molecule-induced remote spin flips. *Phys. Rev. Lett.*, 117:123002, Sep 2016.

[64] R.F. Stebbings and F.B. Dunning. *Rydberg States of Atoms and Molecules*. Essays in nuclear astrophysics. Cambridge University Press, 1983. ISBN 9780521248235.

[65] D. Klar, B. Mirbach, H. J. Korsch, M. W. Ruf, and H. Hotop. Comparison of rate coefficients for rydberg electron and free electron attachment. *Zeitschrift für Physik D Atoms, Molecules and Clusters*, 31(4):235–244, Dec 1994. ISSN 1431-5866.

[66] F B Dunning. Electron-molecule collisions at very low electron energies. *Journal of Physics B: Atomic, Molecular and Optical Physics*, 28(9):1645–1672, may 1995.

[67] M. T. Frey, S. B. Hill, K. A. Smith, F. B. Dunning, and I. I. Fabrikant. Studies of electron-molecule scattering at microelectronvolt energies using very-high-n rydberg atoms. In *AIP Conference Proceedings*. AIP, 1996.

[68] A. A. Khuskivadze, M. I. Chibisov, and I. I. Fabrikant. Adiabatic energy levels and electric dipole moments of rydberg states of rb_2 and cs_2 dimers. *Phys. Rev. A*, 66:042709, Oct 2002.

[69] H. Hotop, M.-W. Ruf, M. Allan, and I.I. Fabrikant. Resonance and threshold phenomena in low-energy electron collisions with molecules and clusters. In *Advances In Atomic, Molecular, and Optical Physics*, pages 85–216. Elsevier, 2003.

[70] Elahe Alizadeh, Thomas M. Orlando, and Léon Sanche. Biomolecular damage induced by ionizing radiation: The direct and indirect effects of low-energy electrons on DNA. *Annual Review of Physical Chemistry*, 66(1):379–398, apr 2015.

[71] Ilko Bald, Janina Kopyra, and Eugen Illenberger. Selective excision of c5 fromD-ribose in the gas phase by low-energy electrons (0–1 eV): Implications for the mechanism of DNA damage. *Angewandte Chemie International Edition*, 45 (29):4851–4855, jul 2006.

[72] Jack Simons. How do low-energy (0.1-2 eV) electrons cause DNA-strand breaks? *Accounts of Chemical Research*, 39(10):772–779, oct 2006.

[73] Frédéric Martin, Paul D. Burrow, Zhongli Cai, Pierre Cloutier, Darel Hunting, and Léon Sanche. strand breaks induced by 0–4 eV electrons: The role of shape resonances. *Phys. Rev. Lett.*, 93:068101, aug 2004.

[74] L. G. Caron and L. Sanche. Low-energy electron diffraction and resonances in DNA and other helical macromolecules. *Phys. Rev. Lett.*, 91:113201, sep 2003.

[75] Edward L Hamilton, Chris H Greene, and HR Sadeghpour. Shape-resonance-induced long-range molecular rydberg states. *Journal of Physics B: Atomic, Molecular and Optical Physics*, 35(10):L199, 2002.

[76] P. Giannakeas, Matthew T. Eiles, F. Robicheaux, and Jan M. Rost. Dressed ion-pair states of an ultralong-range rydberg molecule. *Phys. Rev. Lett.*, 125: 123401, Sep 2020.

[77] Enrico Fermi. Sopra lo spostamento per pressione delle righe elevate delle serie spettrali. *Il Nuovo Cimento*, 11(3):157–166, mar 1934.

[78] A. Omont. On the theory of collisions of atoms in rydberg states with neutral particles. *Journal de Physique*, 38(11):1343–1359, 1977.

[79] D. A. Anderson, S. A. Miller, and G. Raithel. Angular-momentum couplings in long-range rb_2 rydberg molecules. *Phys. Rev. A*, 90:062518, Dec 2014.

[80] Roger Ding, JD Whalen, SK Kanungo, TC Killian, FB Dunning, S Yoshida, and J Burgdörfer. Spectroscopy of sr 87 triplet rydberg states. *Physical Review A*, 98(4):042505, 2018.

[81] L Barbier and M Cheret. Experimental study of penning and hornbeck-molnar ionisation of rubidium atoms excited in a high s or d level (5d nl 11s). *Journal of Physics B: Atomic and Molecular Physics*, 20(6):1229, 1987.

[82] Vera Bendkowsky. *Ultralong range Rydberg molecules: investigation of a novel binding*. PhD thesis, Universität Stuttgart, 2010.

[83] Thomas Niederprüm, Oliver Thomas, Torsten Manthey, Tobias M. Weber, and Herwig Ott. Giant cross section for molecular ion formation in ultracold rydberg gases. *Phys. Rev. Lett.*, 115:013003, Jul 2015.

[84] Xiaoxuan Han, Suying Bai, Yuechun Jiao, Liping Hao, Yongmei Xue, Jianming Zhao, Suotang Jia, and Georg Raithel. Cs $62D_J$ rydberg-atom macrodimers formed by long-range multipole interaction. *Phys. Rev. A*, 97:031403, Mar 2018.

[85] Christophe Boisseau, Ionel Simbotin, and Robin Côté. Macrodimers: Ultralong range rydberg molecules. *Phys. Rev. Lett.*, 88:133004, Mar 2002.

[86] Heiner Saßmannshausen and Johannes Deiglmayr. Observation of rydberg-atom macrodimers: Micrometer-sized diatomic molecules. *Phys. Rev. Lett.*, 117:083401, Aug 2016.

[87] Samuel Markson, Seth T Rittenhouse, Richard Schmidt, James P Shaffer, and Hossein R Sadeghpour. Theory of ultralong-range rydberg molecule formation incorporating spin-dependent relativistic effects: Cs (6s)–cs (np) as case study. *Chem. Phys. Chem.*, 17(22):3683–3691, 2016.

[88] F. Hund. Zur deutung der molekelspektren. ii. *Zeitschrift für Physik*, 42(2-3): 93120, 1927.

[89] John M. Brown and Alan Carrington. *Rotational spectroscopy of diatomic molecules*. Cambridge University Press, 2003.

[90] Felix Engel, Thomas Dieterle, Frederic Hummel, Christian Fey, Peter Schmelcher, Robert Löw, Tilman Pfau, and Florian Meinert. Precision spectroscopy of negative-ion resonances in ultralong-range rydberg molecules. *Physical review letters*, 123(7):073003, 2019.

[91] J. J. Sakurai. *Modern Quantum Mechanics (2nd Edition)*. Pearson, Essex, England, jul 2010. ISBN 0805382917.

[92] Determination of phase-shifts. `http://farside.ph.utexas.edu/teaching/qmech/Quantum/node135.html`. Accessed: 2020-08-07.

[93] Thomas F. O'Malley, Larry Spruch, and Leonard Rosenberg. Modification of effective-range theory in the presence of a long-range (r-4) potential. *Journal of Mathematical Physics*, 2(4):491–498, jul 1961.

[94] C. Bahrim, I. I. Fabrikant, and U. Thumm. Boundary conditions for the pauli equation: Application to photodetachment of cs^-. *Phys. Rev. Lett.*, 87:123003, Aug 2001.

[95] C. Bahrim, I. I. Fabrikant, and U. Thumm. Erratum: Boundary conditions for the pauli equation: Application to photodetachment of cs^- [phys. rev. lett. 87, 123003 (2001)]. *Phys. Rev. Lett.*, 88:109904, Feb 2002.

[96] Matthew T Eiles. Formation of long-range rydberg molecules in two-component ultracold gases. *Physical Review A*, 98(4):042706, 2018.

[97] Matthew T Eiles and Chris H Greene. Hamiltonian for the inclusion of spin effects in long-range rydberg molecules. *Physical Review A*, 95(4):042515, 2017.

[98] MI Chibisov, AA Khuskivadze, and II Fabrikant. Energies and dipole moments of long-range molecular rydberg states. *Journal of Physics B: Atomic, Molecular and Optical Physics*, 35(10):L193, 2002.

[99] Christian Fey, Markus Kurz, Peter Schmelcher, Seth T Rittenhouse, and Hossein R Sadeghpour. A comparative analysis of binding in ultralong-range rydberg molecules. *New Journal of Physics*, 17(5):055010, 2015.

[100] MJ Piotrowicz, C MacCormick, A Kowalczyk, S Bergamini, II Beterov, and EA Yakshina. Measurement of the electric dipole moments for transitions to rubidium rydberg states via autler–townes splitting. *New Journal of Physics*, 13(9):093012, 2011.

[101] Michal Tarana and Roman Čurík. Adiabatic potential-energy curves of long-range rydberg molecules: Two-electron r-matrix approach. *Physical Review A*, 93(1):012515, 2016.

[102] Michal Tarana and Roman Čurík. R-matrix calculations of electron collisions with a lithium atom at low energies. *Physical Review A*, 99(1):012708, 2019.

[103] Michal Tarana. Long-range rydberg molecule rb _2: Two-electron\textit {R}-matrix calculations at intermediate internuclear distances. *arXiv preprint arXiv:2003.13495*, 2020.

[104] P Giannakeas, Matthew T Eiles, F Robicheaux, and Jan-Michael Rost. Generalized local frame transformation theory for ultralong-range rydberg molecules. *arXiv preprint arXiv:2005.10246*, 2020.

[105] Markus Deiß, Shinsuke Haze, Joschka Wolf, Limei Wang, Florian Meinert, Christian Fey, Frederic Hummel, Peter Schmelcher, and Johannes Hecker Denschlag. Observation of spin-orbit-dependent electron scattering using long-range rydberg molecules. *Physical Review Research*, 2(1):013047, 2020.

[106] AR Johnston and PD Burrow. Shape resonances in electron scattering from metal atoms. *Journal of Physics B: Atomic and Molecular Physics*, 15(20): L745, 1982.

[107] Michael Peper and Johannes Deiglmayr. Formation of ultracold ion pairs through long-range rydberg molecules. *Journal of Physics B: Atomic, Molecular and Optical Physics*, 53(6):064001, 2020.

[108] Yun-Jhih Chen, Stefan Zigo, and Georg Raithel. Atom trapping and spectroscopy in cavity-generated optical potentials. *Physical Review A*, 89:063409, jun 2014.

[109] Andrei Derevianko and Hidetoshi Katori. Colloquium: Physics of optical lattice clocks. *Rev. Mod. Phys.*, 83:331–347, May 2011.

[110] Richang Dong, Rong Wei, Yuanbo Du, Fan Zou, Jinda Lin, and Yuzhu Wang. Magnetic field measurement by weak magnetic-sensitive zeeman splitting. *Applied Physics Letters*, 106(15):152402, 2015.

[111] G. W. Biedermann, X. Wu, L. Deslauriers, S. Roy, C. Mahadeswaraswamy, and M. A. Kasevich. Testing gravity with cold-atom interferometers. *Phys. Rev. A*, 91:033629, Mar 2015.

[112] Renée Charrière, Malo Cadoret, Nassim Zahzam, Yannick Bidel, and Alexandre Bresson. Local gravity measurement with the combination of atom interferometry and bloch oscillations. *Phys. Rev. A*, 85:013639, Jan 2012.

[113] Cheng Sheng, Xiaodong He, Peng Xu, Ruijun Guo, Kunpeng Wang, Zongyuan Xiong, Min Liu, Jin Wang, and Mingsheng Zhan. High-fidelity single-qubit gates on neutral atoms in a two-dimensional magic-intensity optical dipole trap array. *Physical review letters*, 121(24):240501, 2018.

[114] Hidetoshi Katori, Masao Takamoto, V. G. Pal'chikov, and V. D. Ovsiannikov. Ultrastable optical clock with neutral atoms in an engineered light shift trap. *Phys. Rev. Lett.*, 91:173005, Oct 2003.

[115] Andrei Derevianko. "doubly magic" conditions in magic-wavelength trapping of ultracold alkali-metal atoms. *Phys. Rev. Lett.*, 105:033002, Jul 2010.

[116] Paul S Barklem. Accurate abundance analysis of late-type stars: advances in atomic physics. *The Astronomy and Astrophysics Review*, 24(1):9, 2016.

[117] Lianshui Zhao, Werner Eissner, Sultana N Nahar, and Anil K Pradhan. Converged close-coupling r-matrix calculations of photoionization of fe xvii in astrophysical plasmas: from convergence to completeness. *arXiv preprint arXiv:1801.02188*, 2018.

[118] Sultana N Nahar and Anil K Pradhan. Large enhancement in high-energy photoionization of fe xvii and missing continuum plasma opacity. *Physical review letters*, 116(23):235003, 2016.

[119] T. C. Killian, S. Kulin, S. D. Bergeson, L. A. Orozco, C. Orzel, and S. L. Rolston. Creation of an ultracold neutral plasma. *Phys. Rev. Lett.*, 83:4776–4779, Dec 1999.

[120] Thomas K Langin, Grant M Gorman, and Thomas C Killian. Laser cooling of ions in a neutral plasma. *Science*, 363(6422):61–64, 2019.

[121] Fei-lu Wang, Shinsuke Fujioka, Hiroaki Nishimura, Daiji Kato, Yu-tong Li, Gang Zhao, Jie Zhang, and Hideaki Takabe. Experimental evidence and theoretical analysis of photoionized plasma under x-ray radiation produced by an intense laser. *Physics of Plasmas*, 15(7):073108, 2008.

[122] S Fujioka, Z Zhang, N Yamamoto, S Ohira, Y Fujii, K Ishihara, T Johzaki, A Sunahara, Y Arikawa, K Shigemori, et al. High-energy-density plasmas generation on gekko-lfex laser facility for fast-ignition laser fusion studies and laboratory astrophysics. *Plasma Physics and Controlled Fusion*, 54(12):124042, 2012.

[123] Andrzej Bartnik, Przemyslaw Wachulak, Henryk Fiedorowicz, Tomasz Fok, Roman Jarocki, and Miroslaw Szczurek. Extreme ultraviolet-induced photoionized plasmas. *Physica Scripta*, 2014(T161):014061, 2014.

[124] MS Safronova, WR Johnson, and A Derevianko. Relativistic many-body calculations of energy levels, hyperfine constants, electric-dipole matrix elements, and static polarizabilities for alkali-metal atoms. *Physical Review A*, 60(6):4476, 1999.

[125] MS Safronova, Carl J Williams, and Charles W Clark. Relativistic many-body calculations of electric-dipole matrix elements, lifetimes, and polarizabilities in rubidium. *Physical Review A*, 69(2):022509, 2004.

[126] MS Safronova and UI Safronova. Critically evaluated theoretical energies, lifetimes, hyperfine constants, and multipole polarizabilities in rb 87. *Physical Review A*, 83(5):052508, 2011.

[127] CD Herold, VD Vaidya, Xiao Li, SL Rolston, JV Porto, and MS Safronova. Precision measurement of transition matrix elements via light shift cancellation. *Physical review letters*, 109(24):243003, 2012.

[128] Bindiya Arora, MS Safronova, and Charles W Clark. Determination of electric-dipole matrix elements in k and rb from stark shift measurements. *Physical Review A*, 76(5):052516, 2007.

[129] A Sieradzan, MD Havey, and MS Safronova. Combined experimental and theoretical study of the 6 p 2 p j 8 s 2 s 1/2 relative transition matrix elements in atomic cs. *Physical Review A*, 69(2):022502, 2004.

[130] A. A. Vasilyev, I. M. Savukov, M. S. Safronova, and H. G. Berry. Measurement of the $6s - 7p$ transition probabilities in atomic cesium and a revised value for the weak charge Q_W. *Phys. Rev. A*, 66:020101, Aug 2002.

[131] RV Ambartzumian, NP Furzikov, VS Letokhov, and AA Puretsky. Measuring photoionization cross-sections of excited atomic states. *Applied physics*, 9(4): 335–337, 1976.

[132] Timothy P Dinneen, Christopher D Wallace, Kit-Yan N Tan, and Phillip L Gould. Use of trapped atoms to measure absolute photoionization cross sections. *Optics letters*, 17(23):1706–1708, 1992.

[133] JR Lowell, T Northup, BM Patterson, T Takekoshi, and RJ Knize. Measurement of the photoionization cross section of the 5 s 1/2 state of rubidium. *Physical Review A*, 66(6):062704, 2002.

[134] M Witkowski, R Munoz-Rodriguez, A Raczyński, J Zaremba, B Nagórny, PS Żuchowski, R Ciuryło, and M Zawada. Photoionization cross sections of the 5 s 1/2 and 5 p 3/2 states of rb in simultaneous magneto-optical trapping of rb and hg. *Physical Review A*, 98(5):053444, 2018.

[135] C Gabbanini, S Gozzini, and A Lucchesini. Photoionization cross section measurement in a rb vapor cell trap. *Optics Communications*, 141(1-2):25–28, 1997.

[136] Ali Nadeem and S. U. Haq. Photoionization from the $5p^2P_{3/2}$ state of rubidium. *Phys. Rev. A*, 83:063404, Jun 2011.

[137] BC Duncan, V Sanchez-Villicana, PL Gould, and HR Sadeghpour. Measurement of the rb (5 d 5/2) photoionization cross section using trapped atoms. *Physical Review A*, 63(4):043411, 2001.

[138] C Gabbanini. Assessments of lifetimes and photoionization cross-sections at 10.6 μm of nd rydberg states of rb measured in a magneto-optical trap. *Spectrochimica Acta Part B: Atomic Spectroscopy*, 61(2):196–199, 2006.

[139] F Markert, Peter Würtz, Andreas Koglbauer, Tatjana Gericke, A Vogler, and Herwig Ott. Ac-stark shift and photoionization of rydberg atoms in an optical dipole trap. *New Journal of Physics*, 12(11):113003, 2010.

[140] J. Tallant, D. Booth, and J. P. Shaffer. Photoionization rates of cs rydberg atoms in a 1064-nm far-off-resonance trap. *Phys. Rev. A*, 82:063406, Dec 2010.

[141] VA Davydkin and BA Zon. Radiation and polarization characteristics of rydberg atomic states. 2. *Optika I Spektroskopiya*, 52(4):600–604, 1982.

[142] AA Kamenski and VD Ovsiannikov. Electric-field-induced redistribution of radiation transition probabilities in atomic multiplet lines. *Journal of Physics B: Atomic, Molecular and Optical Physics*, 39(9):2247, 2006.

[143] S Snigirev, A Golovizin, D Tregubov, S Pyatchenkov, D Sukachev, A Akimov, V Sorokin, and N Kolachevsky. Measurement of the 5 d-level polarizability in laser-cooled rb atoms. *Physical Review A*, 89(1):012510, 2014.

[144] Kyle W Martin, Benjamin Stuhl, Jon Eugenio, Marianna S Safronova, Gretchen Phelps, John H Burke, and Nathan D Lemke. Frequency shifts due to stark effects on a rubidium two-photon transition. *Physical Review A*, 100(2):023417, 2019.

[145] D Touahri, O Acef, A Clairon, J-J Zondy, R Felder, L Hilico, B De Beauvoir, F Biraben, and F Nez. Frequency measurement of the 5s12 (f= 3)- 5d52 (f= 5) two-photon transition in rubidium. *Optics Communications*, 133(1-6):471–478, 1997.

[146] L Hilico, R Felder, D Touahri, O Acef, A Clairon, and F Biraben. Metrological features of the rubidium two-photon standards of the bnm-lptf and kastler brossel laboratories. *The European Physical Journal-Applied Physics*, 4(2):219–225, 1998.

[147] Osama Terra and Hatem Hussein. An ultra-stable optical frequency standard for telecommunication purposes based upon the 5s 1/2 5d 5/2 two-photon transition in rubidium. *Applied Physics B*, 122(2):27, 2016.

[148] Ketan D Rathod and Vasant Natarajan. Accessing the $5s_{1/2} \rightarrow 5d_{5/2}$ two-photon transition in rb using a diode laser system. *Sci. and Cult.*, 83:39–41, 2017.

[149] Kyle W. Martin, Gretchen Phelps, Nathan D. Lemke, Matthew S. Bigelow, Benjamin Stuhl, Michael Wojcik, Michael Holt, Ian Coddington, Michael W. Bishop, and John H. Burke. Compact optical atomic clock based on a two-photon transition in rubidium. *Phys. Rev. Applied*, 9:014019, Jan 2018.

[150] V Gerginov and K Beloy. Two-photon optical frequency reference with active ac stark shift cancellation. *Physical Review Applied*, 10(1):014031, 2018.

[151] Kyle W Martin, Benjamin Stuhl, Jon Eugenio, Marianna S Safronova, Gretchen Phelps, John H Burke, and Nathan D Lemke. Frequency shifts due to stark effects on a rubidium two-photon transition. *Physical Review A*, 100(2):023417, 2019.

[152] TJ Quinn. Practical realization of the definition of the metre, including recommended radiations of other optical frequency standards (2001). *Metrologia*, 40 (2):103, 2003.

[153] Andreas Neuzner, Matthias Körber, Stephan Dürr, Gerhard Rempe, and Stephan Ritter. Breakdown of atomic hyperfine coupling in a deep optical-dipole trap. *Physical Review A*, 92(5):053842, 2015.

[154] Keith D Bonin and Michael A Kadar-Kallen. Theory of the light-force technique for measuring polarizabilities. *Physical Review A*, 47(2):944, 1993.

[155] M Marinescu, HR Sadeghpour, and A Dalgarno. Dynamic dipole polarizabilities of rubidium. *Physical Review A*, 49(6):5103, 1994.

[156] Nikola Šibalić, Jonathan D Pritchard, Charles S Adams, and Kevin J Weatherill. Arc: An open-source library for calculating properties of alkali rydberg atoms. *Computer Physics Communications*, 220:319–331, 2017.

[157] D. M. Brink and G. R. Satchler. *Angular Momentum, 2nd ed.* Clarendon Press, 1968.

[158] John C Tully and Richard K Preston. Trajectory surface hopping approach to nonadiabatic molecular collisions: the reaction of h+ with d2. *The Journal of Chemical Physics*, 55(2):562–572, 1971.

[159] John C Tully. Molecular dynamics with electronic transitions. *The Journal of Chemical Physics*, 93(2):1061–1071, 1990.

[160] Serge Haroche. Nobel lecture: Controlling photons in a box and exploring the quantum to classical boundary. *Reviews of Modern Physics*, 85(3):1083, 2013.

[161] Thanh Long Nguyen, Jean-Michel Raimond, Clément Sayrin, Rodrigo Cortinas, Tigrane Cantat-Moltrecht, Fédéric Assemat, Igor Dotsenko, Sébastien Gleyzes, Serge Haroche, Guillaume Roux, et al. Towards quantum simulation with circular rydberg atoms. *Physical Review X*, 8(1):011032, 2018.

[162] Richard R Freeman and Daniel Kleppner. Core polarization and quantum defects in high-angular-momentum states of alkali atoms. *Physical Review A*, 14 (5):1614, 1976.

[163] Stephen R Lundeen. Fine structure in high-l rydberg states: A path to properties of positive ions. *Advances in atomic, molecular, and optical physics*, 52: 161–208, 2005.

[164] SJ Berl, CA Sackett, TF Gallagher, and J Nunkaew. Core polarizability of rubidium using spectroscopy of the ng to nh, ni rydberg transitions. *arXiv preprint arXiv:2004.08226*, 2020.

[165] Randall G Hulet and Daniel Kleppner. Rydberg atoms in "circular" states. *Physical review letters*, 51(16):1430, 1983.

[166] Robert Lutwak, Jeffrey Holley, Pin Peter Chang, Scott Paine, Daniel Kleppner, and Theodore Ducas. Circular states of atomic hydrogen. *Physical Review A*, 56(2):1443, 1997.

[167] Ryan Cardman and Georg Raithel. Circularizing rydberg atoms with time-dependent optical traps. *Physical Review A*, 101(1):013434, 2020.

[168] William A Chupka. Lifetimes of very high rydberg states of aromatic molecules. *The Journal of chemical physics*, 99(8):5800–5806, 1993.

[169] Paolo Bellomo, David Farrelly, and T Uzer. Collisional population of ultra-high, ultra-long-living rydberg states under zero-electron-kinetic-energy conditions. *The Journal of chemical physics*, 107(7):2499–2515, 1997.

[170] SK Dutta, D Feldbaum, A Walz-Flannigan, JR Guest, and G Raithel. High-angular-momentum states in cold rydberg gases. *Physical Review Letters*, 86 (18):3993, 2001.

[171] Alisa Walz-Flannigan, JR Guest, J-H Choi, and G Raithel. Cold-rydberg-gas dynamics. *Physical Review A*, 69(6):063405, 2004.

[172] Andrew Held, Leonid Ya Baranov, Heinrich L Selzle, and Edward W Schlag. Lifetime control in rydberg states using fast switching dc electric fields: Ii. enhancement for nitric oxide. *Chemical physics letters*, 291(3-4):318–324, 1998.

[173] D Delande and JC Gay. A new method for producing circular rydberg states. *EPL (Europhysics Letters)*, 5(4):303, 1988.

[174] J Hare, M Gross, and P Goy. Circular atoms prepared by a new method of crossed electric and magnetic fields. *Physical review letters*, 61(17):1938, 1988.

[175] WE Cooke, TF Gallagher, SA Edelstein, and RM Hill. Doubly excited autoionizing rydberg states of sr. *Physical Review Letters*, 40(3):178, 1978.

[176] L Pruvost, P Camus, J-M Lecomte, CR Mahon, and P Pillet. High angular momentum 6pnl and 6dnl doubly excited rydberg states of barium. *Journal of Physics B: Atomic, Molecular and Optical Physics*, 24(22):4723, 1991.

[177] U Eichmann, V Lange, and W Sandner. Dipole structure of planetary atoms. *Physical review letters*, 68(1):21, 1992.

[178] BE Tannian, CL Stokely, FB Dunning, CO Reinhold, and J Burgdörfer. Manipulation of atomic-state distributions using pulsed electric fields. *Journal of Physics B: Atomic, Molecular and Optical Physics*, 32(18):L517, 1999.

[179] Hao Zhang, Limei Wang, Linjie Zhang, Changyong Li, Liantuan Xiao, Jianming Zhao, Suotang Jia, Patrick Cheinet, Daniel Comparat, and Pierre Pillet. Stark-induced l-mixing interferences in ultracold cesium rydberg atoms. *Physical Review A*, 87(3):033405, 2013.

[180] Limei Wang, Hao Zhang, Linjie Zhang, Changyong Li, Yonggang Yang, Jianming Zhao, Georg Raithel, and Suotang Jia. Dipolar rydberg-atom gas prepared by adiabatic passage through an avoided crossing. *New Journal of Physics*, 17 (6):063011, 2015.

[181] John D Corless and CR Stroud Jr. Optical mixing of rydberg angular momenta. *Physical review letters*, 79(4):637, 1997.

[182] HM Nilsen, JP Hansen, S Selstø, and LB Madsen. Laser excitation of angular rydberg wavepackets. *Journal of Physics B: Atomic, Molecular and Optical Physics*, 32(20):4995, 1999.

[183] Birgit S Mecking and P Lambropoulos. Laser excitation of radial-angular rydberg wave packets. *Physical review letters*, 83(9):1743, 1999.

[184] HG Muller and LD Noordam. Suppression of angular-momentum mixing in photoexcitation of rydberg states by multistate off-resonant quantum coherence. *Physical review letters*, 82(25):5024, 1999.

[185] Lars Bojer Madsen. Comment on suppression of angular-momentum mixing in photoexcitation of rydberg states by multistate off-resonant quantum coherence. *Physical review letters*, 85(4):898, 2000.

[186] HG Muller and LD Noordam. Muller and noordam reply. *Physical review letters*, 85(4):899, 2000.

[187] Halvor Møll Nilsen and JP Hansen. Generation of an angular and radial rydberg wave packet in a single laser pulse. *Physical Review A*, 63(1):011405, 2000.

[188] R Parzyński, M Sobczak, and A Wójcik. Photoionization indicators of optical mixing of different-parity degenerate rydberg states. *Physical Review A*, 61(2): 023413, 2000.

[189] R Parzynski, M Sobczak, and A Wójcik. Photoionization artifacts from model rydberg atoms. *Journal of Physics B: Atomic, Molecular and Optical Physics*, 34(18):3629, 2001.

[190] R Parzyński, M Sobczak, and A Wójcik. Rydberg-atom photoionization with and without the single-n manifold approximation. *Physical Review A*, 63(6): 063413, 2001.

[191] HG Muller. Suppression of angular-momentum mixing in precision solutions of the schrödinger equation for photoexcitation of rydberg states. *Physical Review A*, 65(5):055402, 2002.

[192] Halvor Møll Nilsen, LB Madsen, and JP Hansen. On selection rules for atoms in laser fields and high harmonic generation. *Journal of Physics B: Atomic, Molecular and Optical Physics*, 35(17):L403, 2002.

[193] Yannis Komninos, Theodoros Mercouris, and Cleanthes A Nicolaides. Theory and computation of the matrix elements of the full interaction of the electromagnetic field with an atomic state: Application to the rydberg and the continuous spectrum. *Physical Review A*, 65(4):043412, 2002.

[194] Theodoros Mercouris, Yannis Komninos, and Cleanthes A Nicolaides. Electric dipole versus full interaction in the dynamics of laser excitation of rydberg wavepackets. *Journal of Physics B: Atomic, Molecular and Optical Physics*, 35 (6):1439, 2002.

[195] R Parzyński and M Sobczak. Beyond the long-wavelength approximation in electromagnetic rydberg–rydberg couplings. *Optics communications*, 225(1-3): 123–130, 2003.

[196] Yannis Komninos, Theodoros Mercouris, and Cleanthes A Nicolaides. Long-wavelength approximation in on-and off-resonance transitions. *Physical Review A*, 71(2):023410, 2005.

[197] Theodoros Mercouris, Yannis Komninos, and Cleanthes A Nicolaides. The state-specific expansion approach to the solution of the polyelectronic time-dependent schrödinger equation for atoms and molecules in unstable states. In *Advances in Quantum Chemistry*, volume 60, pages 333–405. Elsevier, 2010.

[198] Dashavir Chetty, Rohan D Glover, Bruno A deHarak, Xiao-Min Tong, Han Xu, Tom Pauly, Noah Smith, Kathryn R Hamilton, Klaus Bartschat, Joseph P Ziegel, et al. Observation of dynamic stark resonances in strong-field excitation. *Physical Review A*, 101(5):053402, 2020.

[199] Katarzyna Krajewska, Ilya I Fabrikant, and Anthony F Starace. Threshold effects in strong-field ionization: Energy shifts and rydberg structures. *Physical Review A*, 86(5):053410, 2012.

[200] Qianguang Li, Xiao-Min Tong, Toru Morishita, Hui Wei, and Chii Dong Lin. Fine structures in the intensity dependence of excitation and ionization probabilities of hydrogen atoms in intense 800-nm laser pulses. *Physical Review A*, 89(2):023421, 2014.

[201] Bin Zhang, Wenbo Chen, and Zengxiu Zhao. Generation of rydberg states of hydrogen atoms with intense laser pulses: The roles of coulomb force and initial lateral momentum. *Physical Review A*, 90(2):023409, 2014.

[202] H Zimmermann, S Patchkovskii, M Ivanov, and U Eichmann. Unified time and frequency picture of ultrafast atomic excitation in strong laser fields. *Physical review letters*, 118(1):013003, 2017.

[203] B Piraux, F Mota-Furtado, PF O'Mahony, A Galstyan, and Yu V Popov. Excitation of rydberg wave packets in the tunneling regime. *Physical Review A*, 96(4):043403, 2017.

[204] J Venzke, R Reiff, Z Xue, A Jaroń-Becker, and A Becker. Angular momentum distribution in rydberg states excited by a strong laser pulse. *Physical Review A*, 98(4):043434, 2018.

[205] Shilin Hu, Xiaolei Hao, Hang Lv, Mingqing Liu, Tianxiang Yang, Haifeng Xu, Mingxing Jin, Dajun Ding, Qianguang Li, Weidong Li, et al. Quantum dynamics of atomic rydberg excitation in strong laser fields. *Optics express*, 27(22): 31629–31643, 2019.

[206] PeiPei Xin, Hong Cheng, ShanShan Zhang, HanMu Wang, ZiShan Xu, and HongPing Liu. Creating high-purity angular-momentum-state rydberg atoms by a pair of unipolar laser pulses. *Physical Review A*, 97(4):043425, 2018.

[207] MA Henry and F Robicheaux. Simulation of motion and radiative decay of rydberg hydrogen atoms in electric and magnetic fields. *Journal of Physics B: Atomic, Molecular and Optical Physics*, 44(14):145003, 2011.

[208] Daniel Comparat and Chloé Malbrunot. Laser-stimulated deexcitation of rydberg antihydrogen atoms. *Physical Review A*, 99(1):013418, 2019.

[209] SK Dutta, JR Guest, D Feldbaum, A Walz-Flannigan, and Georg Raithel. Ponderomotive optical lattice for rydberg atoms. *Physical review letters*, 85 (26):5551, 2000.

[210] Kelly Cooper Younge, Sarah Elizabeth Anderson, and Georg Raithel. Adiabatic potentials for rydberg atoms in a ponderomotive optical lattice. *New Journal of Physics*, 12(2):023031, 2010.

[211] B Knuffman and G Raithel. Multipole transitions of rydberg atoms in modulated ponderomotive potentials. *Physical Review A*, 75(5):053401, 2007.

[212] T Van der Veldt, W Vassen, and W Hogervorst. Helium rydberg states in parallel electric and magnetic fields. *Journal of Physics B: Atomic, Molecular and Optical Physics*, 26(13):1945, 1993.

[213] Sarah E Anderson and Georg Raithel. Ionization of rydberg atoms by standing-wave light fields. *Nature communications*, 4(1):1–7, 2013.

[214] A Duspayev, X Han, MA Viray, L Ma, J Zhao, and G Raithel. Long-range rydberg-atom-ion molecules of rb and cs. *arXiv preprint arXiv:2101.05132*, 2021.

[215] E Hansis, T Cubel, J-H Choi, JR Guest, and G Raithel. Simple pressure-tuned fabry–pérot interferometer. *Review of scientific instruments*, 76(3):033105, 2005.